UNIVERSITY OF CALIFORNIA, MERCED

PhD Dissertation

Understanding Structure-property Relationships between Tribological Properties and Chemistry of Phosphonium Ionic Liquids

by

Ting Liu

A dissertation submitted in partial satisfaction of the
requirements for the degree of Doctor of Philosophy
in
Mechanical Engineering
at
University of California, Merced

Committee in charge:
Associate Professor Mehmet Baykara, Chair
Associate Professor Abel Chuang
Associate Professor Pradeep Menezes
Professor Ashlie Martini, Advisor

June, 2023

The dissertation of Ting Liu, titled Understanding Structure-property Relationships between Tribological Properties and Chemistry of Phosphonium Ionic Liquids, is approved, and it is acceptable in quality and form for publication on microfilm and electronically:

.....	.....
Dr. Mehmet Baykara	Date
Committee Chair	
.....	.....
Dr. Ashlie Martini	Date
Advisor	
.....	.....
Dr. Pradeep Menezes	Date
Committee Member	
.....	.....
Dr. Abel Chuang	Date
Committee Member	

I, Ting Liu, declare that this disertation titled - Understanding Structure-property Relationships between Tribological Properties and Chemistry of Phosphonium Ionic Liquids - and the work presented in it are my own. I confirm that:

- This work was done wholly or mainly while in candidature for a research degree at this University.
- Where any part of this thesis has previously been submitted for a degree or any other qualification at this University or any other institution, this has been clearly stated.
- Where I have consulted the published work of others, this is always clearly attributed.
- Where I have quoted from the work of others, the source is always given. With the exception of such quotations, this thesis is entirely my own work.
- I have acknowledged all main sources of help.
- Where the thesis is based on work done by myself jointly with others, I have made clear exactly what was done by others and what I have contributed myself.

....

Ting Liu Date

....

Dr. Ashlie Martini Date

Advisor

Contents

List of Figures

List of Tables

List of Abbreviations

The following are abbreviations used for cations and anions within the body of the document.

BMIM	1-butyl-3-methylimidazolium
Lau	laurate
Pmt	palmitate
Ste	stearate
Ole	oleate
DMIM	1,3-dimethylimidazolium
EMIM	1-ethyl-3-methylimidazolium
HMIM	1-hexyl-3-methylimidazolium
N8,8,8,1	methyltrioctylammonium
PrMIM	1-propyl-3-methylimidazolium
P1,1,1,1	tetramethylphosphonium
P1,1,1,5	pentyltrimethylphosphonium
P1,1,1,6	hexyltrimethylphosphonium
P2,2,2,2	tetraethylphosphonium
P2,2,2,5	triethylpentylphosphonium
P2,2,2,8	triethyloctylphosphonium
P2,2,2,10	triethyldecylphosphonium
P2,2,2,12	triethyldodecylphosphonium
P2,2,2,1O1	triethyl(methoxymethyl)phosphonium
P2,2,2,2O1	triethyl(2-methoxyethyl)phosphonium
P3,3,3,3	tetrapropylphosphonium
P4,4,4,2	tributylethylphosphonium

P4,4,4,4	tetrabutylphosphonium
P4,4,4,6	tributylhexylphosphonium
P4,4,4,8	tributyloctylphosphonium
P4,4,4,10	tributyldecylphosphonium
P4,4,4,12	tributyldodecylphosphonium
P4,4,4,14	tributyltetradecylphosphonium
P6,6,6,6	tetrahexylphosphonium
P6,6,6,14	trihexyltetradecylphosphonium
P8,8,8,8	tetraoctylphosphonium
$HP(Ph)_3$	triphenylphosphonium
$HP(Oct)_3$	trioctylphosphonium
$P2(Ph)_3$	ethyltriphenylphosphonium
$P3(Ph)_3$	propyltriphenylphosphonium
$P4(Ph)_3$	butyltriphenylphosphonium
$P6(Ph)_3$	hexyltriphenylphosphonium
$P8(Ph)_3$	octyltriphenylphosphonium
β-Ala	β-alaninate
2-CNpyr	2-cyanopyrrolide
3-Triaz	1,2,3-triazolide
$(iC8)_2PO_2$	bis(2,4,4-trimethylpentyl) phosphinate
AcO	acetate
Ala	alaninate
Asp	aspartic acid (aspartate)
BEHP	bis(2-ethylhexyl)phosphate
Benz	benzoate
Benzim	benzimidazolide
BF_4	tetrafluoroborate
BMB	bis(mandelato)borate
BMLB	bis(malonato)borate
BnIm	Benzodimidazolide
BOB	bis(oxalato)borate
Br	bromide
BrBnIm	6-Bromo-benzimidazolide

BScB	bis(salicylato)borate
ButO	butanoate
CF_3pyra	2-(Trifluoromethyl)pyrazolide
Cl	chloride
Cpy	2-cyanopyrrolide
DCA	dicyanamide
DecO	decanoate
DEP	diethyl phosphate
FAP	tris(pentafluoroethyl)trifluorophosphate
Gln	glutaminate
Glu	glutamate
Gly	glycinate
HexO	hexanoate
Ido	1,3-indanedionate
Ile	isoleucinate
Im	Imidazolide
Leu	leucinate
Lys	lysinate
$MeSO_4$	methyl sulfate
Met	methioninate
MMIM	1,3-dimethylimidazolium
OctO	octanoate
OTf	triflate
PAO	polyalphaolefin
PF_6	hexafluorophosphate
Phe	phenylalaninate
PhO	phenolate
Pro	prolinate
PTFE	poly(tetrafluoroethylene)
p-TsO	p-toluene-sulfonate
Sacc	saccharinate
Sali	salicylate
Ser	serinate

Tau	taurinate
Tf_2N	bis(trifluoromethanesulfonyl)imide
TFA	trifluoroacetate
TFO	triflate
TFSI	bis(trifluoromethyl)sulfonylimide
Thr	threonate
TMPP	bis(2,4,4-trimethylpentyl)phosphinate
Val	valinate
ZDDP	dialkyldithiophosphate

Acknowledgement

First and foremost I am extremely grateful to my advisor Professor Ashlie Martini for her invaluable advice, continuous support, and patience during my PhD study. Professor Ashlie Martini is the best advisor I have ever know. She is also great researcher and educator, who has the wisdom, motivation, and energy to mentor and support her students and keep them on the right track towards success in a extremely professional manner. Her immense knowledge and plentiful experience have encouraged me in all the time of my academic research and daily life. Becoming a student in the Martini Research Group is the best decision I have made in 2020 after I joined UC Merced in 2017.

I am grateful to my very supportive family especially my mother, father, and younger sister. It is hard for me to imagine the amount of effort they have made for me to have a good education and future. As the first generation in college of my family history, I would not have gone so far regardless how hard I worked without the support and understanding from my family. Now I have my own family, I would like to express my gratitude to Nuo Li, my fiancee and the mother of my baby son. Without her tremendous understanding and encouragement in the past few years, it would be impossible for me to complete my study. Having a baby during my Ph.D. journey is the best part of my life, here is my deepest gratefulness to my fiancee and my baby son who made me understanding the meaning of inheritance of life.

I would also like to thank Professor Pradeep Menezes, who is also one of my committee member, for his suggestions and positive feedbacks on my biweekly updates of the ionic liquids project. I also acknowledge Md Hafizur Rahman as this dissertation would not have been possible without his support for all corresponding experiments. I also appreciate valuable input from Dr. Manish Patel.

I would also like to thank the other two members of my dissertation committee - Professor Mehmet Baykara and Professor Abel Chuang, not only for their time but also for

their valuable comments and suggestions for my dissertation.

To my wonderful former and current lab-mates in the Martini Research Group, including Dr. Pawan Panwar, Dr. Arash Khajeh, Dr. Quanpeng Yang, Dr. Ingrid Padilla Espinosa, Dr. José Cobeña Reyes, Dr. Karen Mohammadtabar, Dr. Mohammad R. Vazirisereshk, Dr. Azhar Vellore, Dr. Rimei Chen, Dr. Michelle Len, Fakhrul Hasan Bhuiyan, Sergio Romero Garcia, Samuel Leventini, Muztoba Rabbani, Daniel Miliate, etc., thanks for the fun and support. In particular, Dr. Pawan Panwar and Dr. Arash Khajeh provided all necessary technique support for my projects. I appreciate all support and suggestions provided during weekly presentation and small group meetings. I will miss the time we made tiktok videos, calendar pictures, and also parties.

I want to thank all the friends I made during my Ph.D journey in UC Merced, including Anupam Mishra, Ahmad Elhares, Hector Gomez, Yuquan Chen, Yijia Guo, Wenqian Dong, Haolin Liang, Shangjie Ma, Songtao Ye, etc., all of you made my Ph.D journey colorful besides research. Lastly, I wish to sincerely thank Lu Yi, who convinced and encouraged me to pursue a further education in the United State after obtain my Master degree in China.

Again, thank you all for everything that helped me get to this day.

Curriculum Vita

Education

- Ph.D., Mechanical Engineering, University of California, Merced, 2017 - 2023
- M.S., Petroleum Engineering, China University of Petroleum, Beijing, 2014 - 2017
- B.S., Petroleum Engineering, China University of Petroleum, Beijing, 2010 - 2014

Projects

High-Performance Phosphonium Ionic Liquids Lubricants

NSF project in collaboration with University of Nevada, Reno, 02/2021 - 06/2023

- Established structure-property-function relationships to guide design and manufacture of new high performance ionic liquids
- Developed in-house Matlab and Python script for generating MD simulation data files and post processing
- Predicted physico-chemical properties (density, viscosity, specific heat and thermal conductivity) of neat phosphonium ionic liquids and their mixture with water and base oil
- Explored the mechanisms of thermal decomposition and corrosion on iron oxide for phosphonium ionic liquids
- Explored how ion pairs affect contact angle and coefficient of friction trend in contact with steel surface

Cold Spray Defect Prediction By Multi-particle Impact

In collaboration with U.S. Army CCDC Army Research Laboratory, 08/2019 - 07/2020

- Simulated 2D & 3D cold spray process by the impact of multiple particles on a substrate based on LAMMPS simulation using smoothed-particle hydrodynamics to predict voids/pores generation
- Conducted Abaqus simulation of solid particle impacting on substrate with Johnson-Cook plasticity to validate LAMMPS simulation
- Simulated porous medium impact on solid substrate to study porosity vanishing in cold spray

Fluid Structure Interaction in Mesoscale Applications

Water & Energy Laboratory of Mechanical Engineering, UC Merced, 08/2017 - 07/2020

- Developed a computational efficient version of Many-body dissipative particle dynamics simulation package with Fortran for fluid structure interaction
- Simulated mesoscale fluid structure interaction including coalescence induced jumping, electrowetting induced jumping, coalescence of barrel shaped microscale droplets on fiber and droplets moving on fiber with wettability gradient based on the developed scripts
- Established a velocity prediction model for each fluid structure interaction case

Evaluation and prediction on productivity for shale gas, tight gas and coal-bed methane co-production

Funded by China National Offshore Oil Corporation, 06/2014 - 06/2017

- Evaluated and predicted different production modes for for different formation composition scenarios
- Designed special drilling & completion method and conducted corresponding working fluids optimization

Formation Mechanism of Fuzzy Ball Working Fluids

Master Degree Thesis, 06/2014 - 06/2017

- Investigated the forming mechanism of the "One core-two layer-three membrane" structure of fuzzy ball
- Studied physicochemical properties of four major additives of fuzzy ball and interactive reactions among them with water
- Investigated the impact of the dosage and addition order additives on the forming process of fuzzy ball

Publications

- Liu, T., Rahman, M.H., Menezes, P.L. and Martini, A., 2023. Corrosion of ferrous surfaces by phosphonium ionic liquids. Corrosion Science, resubmitted after peer review.
- Liu, T., Rahman, M.H., Menezes, P.L. and Martini, A., 2022. Effect of Ion Pair on Contact Angle for Phosphonium Ionic Liquids. The Journal of Physical Chemistry B, 126(23), pp.4354–4363.
- Liu, T., Panwar, P., Khajeh, A., Rahman, M.H., Menezes, P.L. and Martini, A., 2022. Review of Molecular Dynamics Simulations of Phosphonium Ionic Liquid Lubricants. Tribology Letters, 70(2), pp.1-24.
- Rahman, M. H., Liu, T., Macias, T., Misra, M., Patel, M., Martini, A., & Menezes, P. L., 2022. Physicochemical and tribological comparison of bio- and halogen-based ionic liquid lubricants. Journal of Molecular Liquids, In Press
- Khajeh, A., Rahman, M.H., Liu, T., Panwar, P., Menezes, P.L. and Martini, A., 2022. Thermal decomposition of phosphonium salicylate and phosphonium benzoate ionic liquids. Journal of Molecular Liquids, 352, p.118700.
- Liu, T., Mishra, A., Hemeda, A.A., Palko, J. and Ma, Y., 2020. A Many-body Dissipative Particle Dynamics Study of Coalescence Induced Jumping. In ASTFE Digital Library. Begel House Inc..

- Liu, T., Mishra, A., Torabi, M., Hemeda, A.A., Palko, J. and Ma, Y., 2019. Electrowetting-induced Droplet Jumping Simulation Using Many-body Dissipative Particle Dynamics. In ASTFE Digital Library. Begel House Inc..
- Mishra, A., Hemeda, A. A., Torabi, M., Liu, T., Palko, J., Goyal, S. and Ma, Y., 2019. Flow Visualization around Mesoscale Solid Particle within a Moving Droplet Using Multi-body Dissipative Particle Dynamics. In ASTFE Digital Library. Begel House Inc..
- Torabi, M., Hemeda, A.A., Mishra, A., Liu, T. and Ma, Y., 2019. Liquid Bridge Eruption for Mesoscale Gravure Printing Using Multi-body Dissipative Particle Dynamics. In ASTFE Digital Library. Begel House Inc..
- Yiwei, R., Shuaishuai, N., Baojiang, D., Ting, L., Wensheng, W. and Xuanqing, L. A Novel Method for Quantitative Analysis of Engineering Factors Influencing CBM Production (J). International Journal of Engineering and Technical Research (IJETR) ISSN, 2321-0869.

Awards

- STLE Scholarship Award, Northern California STLE Section, 2023
- Second Prize for poster presentation, STLE 2022 Annual Meeting, 2022
- Bobcat Fellowship, University of California, Merced, 2018 - 2022
- Travel Fellowship, University of California, Merced, 2018 - 2020
- First-tier Scholarship, China University of Petroleum, Beijing, 2014 - 2016
- Championship of the Petrobowl Asia-Pacific Region, Society of Petroleum Engineers, 2015
- Outstanding Graduates, China University of Petroleum, Beijing, 2014
- CNPC Scholarship, China National Petroleum Corporation, 2013

- Incentive Prize of Hope Project Inspired Action, Embassy of the United Kingdom, Beijing, 2012 - 2013
- National Encouragement Scholarship, China University of Petroleum, Beijing, 2011 - 2012

Conferences

- Presenter & Student Poster, 76th Annual Meeting of Society of Tribologists and Lubrication Engineers, Orlando, FL, USA, 2022
- Presenter, Thermal and Fluids Engineering Conference by American Society of Thermal and Fluids Engineers, 2018 - 2020
- Event organizer, China-U.S. Workshop on Management and Remediation of Contaminated Soils and Groundwater, Palm Springs, CA, USA, 2018
- Petrobowl competition, Annual Technical Conference and Exhibition of Society of Petroleum Engineers, 2013 & 2015

Peer Reviewer

- Tribology Letters (2)

Abstract

Ionic liquids (ILs) have many advantages compared to conventional organic compounds in terms of biological, chemical, physical, and thermal properties. Therefore, ILs are considered as promising green engineering liquids for replacement of commonly used volatile organic compounds that offer a convenient solution to challenges associated with both solvent emission and catalytic recycling for a diverse range of applications. Here, we primarily focus on ILs as lubricants and lubricant additives.

For the application in tribology as lubricants/lubricant additives, phosphonium ILs have been the rising star of the ILs family as they have been reported to exhibit lower wear and friction, as well as superior resistance to corrosion and tribo-corrosion. They are more stable in strongly basic media and more thermally stable than other ILs. Also, importantly, some phosphonium ILs can be less toxic and biodegradable than conventional organic compounds.

The physico-chemical properties of phosphonium ILs are tunable depending upon the combination of cation and anion employed. Changes in properties in turn affect the performance of phosphonium ILs as lubricants and lubricant additives. Although there have been many investigations into the relationship between IL properties and ion chemistry/structure, the selection of cations and anions for phosphonium ILs is still very much trial-and-error. To optimize phosphonium ILs for lubrication, a full understanding of the relationship between chemistry/structure and material properties of is phosphonium ILs required. Toward this goal, classical and reactive molecular dynamics simulations are employed to study the molecular scale mechanisms underlying the mechanical response of phosphonium ILs with different cation and anion combinations.

First, a non-reactive force field was used to predict bulk properties, including density, viscosity, and ionic conductivity. The accuracy of the modeling approach was evaluated by comparing to experiment/literature data. In particular, the effect of anions on these bulk

properties was analyzed. The high accuracy in predicting bulk properties provided confidence for using this force field to investigate the wetting behavior and frictional behavior. Then the wetting behavior of phosphonium ILs on iron was studied for different cation-anion pairs to investigate the interaction of phosphonium ILs with solid surfaces. Results showed that contact angle was affected by the anion and increased as benzoate $<$ salicylate $<$ saccharinate longer alkyl chains in the cations led to lower contact angle. The trends were explained in terms of adhesive and cohesive energies in the simulations, and then correlated to the atomic scale differences between the anions and cations. Since the effectiveness of lubricants depends on their frictional behavior, viscous friction that is entirely determined by the fluid properties was investigated for different phosphonium cations. It was found that viscous friction is highly related to cation alkyl chains and chain asymmetry under the same operating condition. A predictive model of viscous friction for tetraalkylphosphonium ILs was then established to capture the effect of cation moiety and operating conditions. Lastly, in many applications, ILs are in direct contact with a metal surface and form a solid-liquid interface and possible corrosion could occur. The origins of corrosion behavior for trihexyltetradecylphosphonium benzoate and trihexyltetradecylphosphonium salicylate on ferrous surfaces was analyzed using reactive molecular dynamics simulations based on the types of bonding and orientation of the anions relative to the surface. It was found that salicylate had more possible bonding scenarios and was more likely to be tilted on the surface than benzoate, affecting the localization of surface-anion bonds and anion coverage density which could affect corrosion mechanisms.

Overall, the results of these studies revealed direct correlations between tribological properties of phosphonium ILs and cation and anion chemistry. The structure-property relationship obtained from this study can ultimately be used to guide the design of high performance phosphonium ILs lubricants.

Chapter 1

Introduction

1.1 Ionic Liquids in General

Ionic liquids (ILs) are salts in the liquid form with melting point below 100°C or even at room temperature that comprise cations and anions [8, 9].

ILs have a number of advantages compared to conventional organic compounds in terms of biological, chemical, physical, and thermal properties [10]. For example, ILs have negligible vapor pressure and wide liquid range of up to more than 400 K. Therefore, ILs have less risk of explosion relative to volatile organic compounds and they have also no side effects on atmospheric photo-chemistry [11]. With this advantage, ILs can be recycled and reused without volume loss [12–14] and are regarded as "environmentally friendly" compared to volatile organic compounds [15]. ILs are also miscible in substances having very wide range of polarities and can dissolve organic and inorganic substances and even polymeric materials. This not only enables the use of ILs as additives, solvents, and catalysts, but also offers numerous opportunities to improve and develop extraction processes for ILs [16]. Additionally, since they consist exclusively of ions, ILs also have higher thermal and electrical conductivity as well as a larger electrochemical window compared to volatile organic compounds [10, 17].

Therefore, ILs are considered as promising green engineering liquids for replacement of commonly used volatile organic compounds that offer a convenient solution to challenges associated with both solvent emission and catalytic recycling [18, 19]. These advantages also make ILs useful for a diverse range of applications such as electro-chemistry, solvent,

engineering, catalysis, biological aid, physical chemistry, analytical chemistry, and many more [9, 17, 20].

This research focuses on ILs as lubricants and lubricant additives [12, 20–22]. Due to the inherent polarity of ions that enable strong surface adsorption [12], ILs can form thick tribo-films that enhance lubrication for rubbing and contacting surfaces [23]. Since ILs were first explored as lubricants and showed excellent tribological characteristics, such as friction reduction, antiwear performance, and high load-carrying capacity [24], interest in IL lubricants has steadily increased [12, 25]. Initially, ILs were studied as neat or base lubricants due to the their low solubility in common nonpolar hydrocarbon lubricating oils [26, 27]. More recently, oil-miscible ILs were developed with promising antiscuffing and antiwear functionalities, and studies have focused on ILs as additives for lubricants [9, 12, 28].

1.2 Phosphonium Ionic Liquids

ILs that have been considered for lubrication use many different anions, either organic or inorganic, and cations. However, the most common cations are ammonium-, phosphonium-, pyrrolidinium-, morpholinium-, imidazolium-, or pyridinium-based [10, 15]. Among these, phosphonium ILs have been the focus of recent studies for several reasons. First, phosphonium ILs have been reported to exhibit lower wear and friction than synthetic and petroleum-based oils as well as ammonium and imidazolium ILs [29–34]. Phosphonium ILs have also better miscibility in mineral and synthetic base oil than their imidazolium and pyrrolidinium counterparts, which is important for the use of ILs as additives [35]. The lack of acidic protons makes phosphonium ILs more stable in strongly basic media and more thermally stable than ammonium ILs [36–38]. Superior resistance to corrosion and tribo-corrosion has also been reported for phosphonium ILs [39–41]. Finally, many halogen-free phosphonium ILs have been developed that are considered environmentally friendly [42–44], since they can be extracted from bio-based feedstock [20] and biodegradable [45–47]. With these advantages, phosphonium ILs are leading candidates for lubricant applications [12, 20–22].

There are several types of phosphonium cations having the general chemical formula [PR_4], with R = H, alkyl, aryl, ester, and halide, etc. Frequently studied phosphonium cations are tetraalkylphosphonium,triarylphosphonium, methoxyalkyl-trialkylphosphonium,

and more complicated forms like [4-(methoxycarbonyl)benzyl](triphenyl)phosphonium [48]. Snapshots of atomistic models of some common phosphonium cations are shown in Figure 1.1.

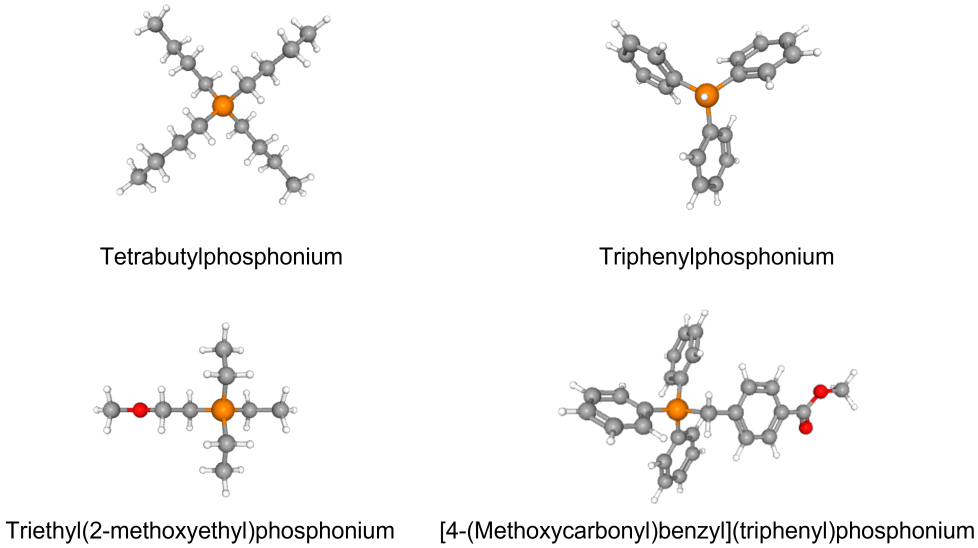

Figure 1.1: Snapshots of atomistic models of representative phosphonium cations. Sphere colors correspond to atoms type: grey C, white H, red O, and orange P.

The physico-chemical properties of phosphonium ILs are tunable depending upon the combination of cation and anion employed. Generally, studies have shown that properties vary with the length and branching of the alkyl chains in the cation and the anion chemistry. Changes in properties in turn affect the performance of phosphonium ILs in different applications. Although there have been many investigations into relationship between IL properties and ion chemistry/structure, the selection of cations and anions for phosphonium ILs is still very much trial-and-error. To optimize phosphonium ILs for lubrication, a full understanding of the relationship between IL chemistry/structure and material properties is required.

Atomistic simulations are important numerical methods for the investigation of magnetic, electronic, chemical, and mechanical properties of materials since these modeling approaches can track atom positions and forces. Such simulations provide a convenient way to investigate correlations between atomic-scale structure and the properties of molecular systems. Atomistic simulations can also complement experimental techniques to reduce

the number of formulations that need to be tested and provide design guidelines. There are many different atomistic simulation methods available [49], but this research focuses on molecular dynamics (MD) simulations with empirical interatomic potentials, or force fields. MD simulations are useful tools for studying ILs because they enable calculation of physico-chemical properties of the fluids at different temperature and stress conditions. More importantly, they provide information about atomic-scale mechanisms underlying observed properties and behaviors [50]. Such information can potentially be used to guide the selection or design of IL lubricants.

In the following sections, previous MD simulation-based studies of phosphonium ILs will be summarized. Although the scope of the summary is limited to phosphonium ILs, simulations of other ILs will be mentioned to provide context for observations and reported results. The summary will begin with a brief introduction to MD simulation methods. This section will focus on the force fields/potentials used in the simulations since those are critical to the accuracy of results. The most widely used reactive and non-reactive force fields developed for studying phosphonium ILs properties will be introduced. Simulation analysis techniques focusing on cation-anion interactions, which play a determining role in physico-chemical properties of phosphonium ILs, will also be introduced. Next, simulation predictions of physico-chemical properties of phosphonium ILs will be summarized including density, viscosity, self-diffusivity, ionic conductivity, heat capacity, and thermal stability. The summary will include studies specifically focused on ILs as lubricants as well as studies designed for other applications that modeled material properties or interactions relevant to lubrication. Then, the effect of interactions between phosphonium ILs and other chemical species, particularly water and CO_2, on IL properties and behavior will be discussed, as well as wetting and confinement by solid surfaces. Lastly, based on the summary of previous work, opportunities for future MD simulation-based studies to understand and guide design of high-performance phosphonium ILs will be identified.

1.3 Molecular Dynamics Simulations of Phosphonium ILs

1.3.1 Empirical Force Fields

In MD simulations, the state of a given molecular structure and its temporal evolution are calculated by Newton's equations of motion [51]. In classical MD simulations, force is

calculated from empirical equations that approximate the quantum-mechanical interactions between atoms, called force fields or potentials. The accuracy of MD simulations is highly dependent on the accuracy of the force field.

There are two broad categories of empirical potentials, reactive and non-reactive. Non-reactive potentials assume permanent covalent bonds between the atoms and cannot be used to study chemical reactions. However, non-reactive potentials are very efficient for predicting thermo-physical properties like density, viscosity, and heat capacity due to their simplicity and low computational cost. Hundreds or thousands of molecules, depending on their size, can be modeled for hundreds of nanoseconds using this approach. Reactive force fields, although less computationally efficient than non-reactive models, capture the formation and breaking of chemical bonds and so are suitable for modeling properties such as thermal stability as well as reactions between species. Here, the most widely used reactive and non-reactive force fields for studying phosphonium ILs are introduced.

The non-reactive force fields for ILs can be classified into two categories: polarizable [2, 52–57] and non-polarizable [58–63]. Non-polarizable force fields handle individual atoms as point masses with fixed atomic charge, and do not explicitly consider the polarization of the atoms as a response to external electric fields, while polarizable force fields include explicit treatment of the polarization effect to improve the calculation of electrostatics [64].

Studies have shown that the polarizable force fields are better able to model the physicochemical properties of ILs [2, 52–57]. The polarizable force fields are more computationally expensive than their non-polarizable counterparts. However, the greater computational power now available to researchers has enabled polarizable force field-based simulations on time and length scales long enough to ensure proper sampling of the phase space. Unfortunately, there are still relatively few polarizable models for phosphonium ILs [2, 52–57]. The Atomistic Polarizable Potential for Liquids, Electrolytes, & Polymers (APPLE&P) is currently the only polarizable force-field applied to study phosphonium ILs [53]. Therefore, parameters for non-polarizable force fields, such as AMBER [65] and OPLS [66], have been refined or revisited to better predict the interactions in ILs. IL-specific parameters have been developed for AMBER [67–69], the generalized Amber force field (GAFF)[70, 71], CLASS I (based on the AMBER framework) [72], DREIDING[2], OPLS [73, 74], and CL&P (based on the OPLS framework) [63, 75–79]. These optimized force fields have been shown to simulate the mechanics that dominate phosphonium IL properties on

the molecular level with reasonable accuracy. Among these force fields, the AMBER force field parameter sets have been developed for the widest range of phosphonium ILs cation-anion pairs [1, 2, 6, 33, 67, 69, 80–82].

Since non-reactive force fields cannot capture bond dissociation and formation, they are not able to model some properties. This limitation is overcome by reactive force fields that have been developed to study various materials, systems, and chemical reactions [72]. Unfortunately, reactive force fields developed for ILs are even rarer than non-reactive force fields, due to the difficulty of the parameterization procedure and the extensive ab initio data sets for proper fitting of the numerous force field parameters [72]. The only reactive force field for which a parameter set has been developed specifically for ILs is ReaxFF [83]. An IL-specific ReaxFF parameter set was developed to study the chemical and physical interactions in a mixture of [P4,4,4,4][Gly]and CO_2 [3]. In this force field, polarization effects are considered through a geometry-dependent charge equilibration scheme. Further, a shielding term was included to avoid excessively close-range nonbonded interactions between the anions and cations. Based on the potential parameters of this force field, a new parameter set for Fe/P/O interactions was developed to analyze the conversion of tricresyl phosphate on an iron oxide surface[84]. This new developed potential set was then used previously model thermal decomposition of tricresyl phosphate on ferrous surfaces [85] and thermal decomposition phosphonium benzoate and phosphonium salicylate [5]. Since this is the only reactive potential available for ILs, there are just a few simulation studies of properties that involve chemical reactions of phosphonium ILs.

1.3.2 Simulation Analysis Methods

The interactions between ions have been widely used to understand and predict the physical properties of ILs [86, 87]. The three main types of interactions in neat ILs are cation-cation, cation-anion, and anion-anion. All three types of interactions may affect lubricant properties and can be analyzed using the methods described in this section. However, most previous studies have focused on cation-anion interactions to explain properties and trends [82, 88–90]. For ILs as additives or ILs with impurities, interactions with other chemical species also need to be considered. Interactions between ions, and between ions and other species, have been characterized by interionic/intermolecular interaction energies, radial distribution functions, spatial distribution functions, charge distributions, and

hydrogen bonding [33, 82, 88, 89, 91].

First, the interaction energy of ion pairs plays a crucial role in determining the ionic dissociation/association dynamics of ILs [86]. Therefore, interionic interaction energies can be used to understand the physical properties of ILs [87, 92]. Interionic/intermolecular interaction energies are calculated from simulations as the sum of electrostatic and van der Waals interactions between atoms [1, 91].

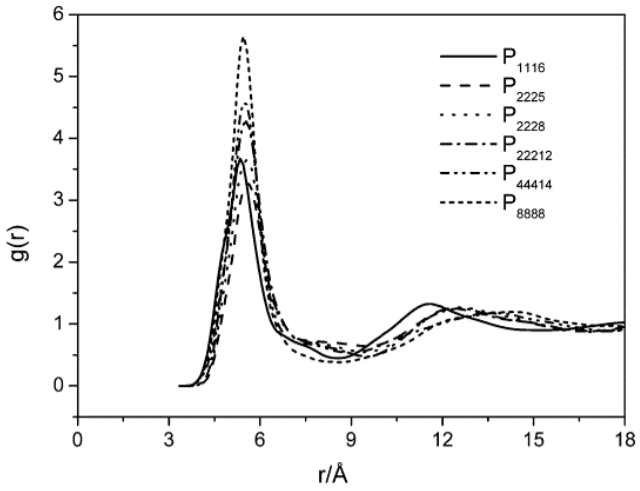

Figure 1.2: Representative RDF between P_{cation}-N_{anion} in ILs with [Tf_2N] and six different phosphonium cations. The height and position of the first peak are used to quantify cation-anion interactions [1]. Figure reprinted with permission from J. Phys. Chem. B 2012, 116, 16, 4934–4942. Copyright 2012 American Chemical Society.

A radial distribution function (RDF) quantifies the probability of finding an atom at some distance from a reference atom. It is obtained from simulations by calculating the distance between all atom pairs and binning them into a histogram [51]. A representative RDF for [Tf_2N] and six different phosphonium cations is shown in Figure 1.2. RDFs are important because they can be used to link microscopic details to macroscopic properties. Generally, a higher first peak in the cation-anion RDF indicates stronger interactions [1] while the position of the peak corresponds to the interaction distance [69].

One of the limitations of an RDF analysis is that detailed information of the local liquid structure can be lost due to cancellation of contributions from regions of low and high probability at the same distance but different parts of the local structure [93, 94]. Therefore, one-dimensional RDFs are unable to characterize uniquely the local spatial assembly

of molecules (ions) in a liquid [94]. Spacial distribution function (SDF) analyses overcome the limitations of RDFs. Specifically, SDFs capture both the radial and angular coordinates of the interatomic separation vector. SDFs between all independent atomic pairs can provide the 3-dimensional neighborhood surrounding a molecule (ion) or atom in the local coordinate system [94, 95]. Representative SDFs for [P4,4,4,8] with four different anions are shown in Figure 1.3. Such analysis can provide information about the local structure in molecular liquids that is not available in a RDF.

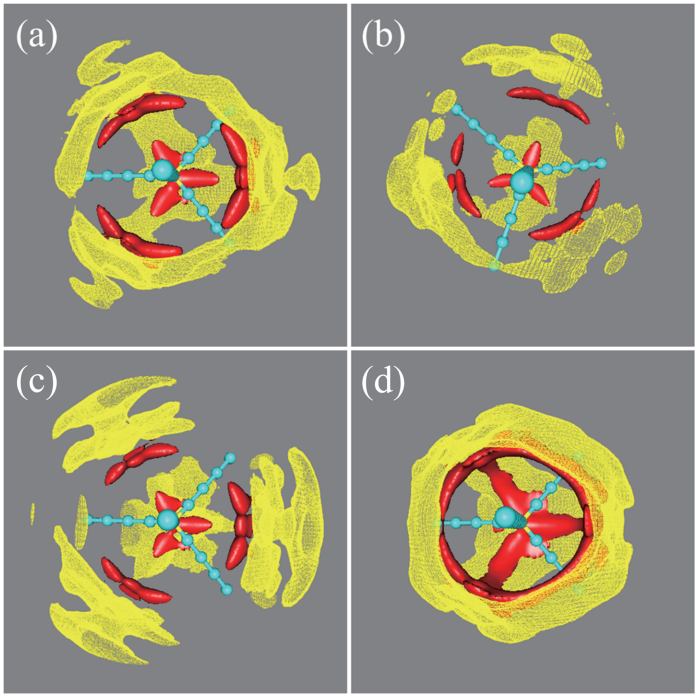

Figure 1.3: Representative SDFs of the B atom (yellow meshed surface) and all O atoms (red solid surface) in (a) [BMB], (b) [BMLB], (c) [BOB], and (d) [BScB] anions around the [P4,4,4,8] cation (P and C atoms are represented by yellow and cyan beads, respectively) obtained from atomistic simulations. In each case, the red and yellow bounded contour surfaces are drawn at 5.5 and 4.0 times the average density, respectively [2]. Figure reprinted with permission from J. Phys. Chem. B 2014, 118, 29, 8711–8723. Copyright 2014 American Chemical Society.

Next, the charge distribution across an IL affects chemical and separation processes. The charge distribution is recognized as an essential feature of ILs, influencing properties on the molecular as well as on the macroscopic scale. For non-polarizable force fields, charge distributions are calculated from the electrostatic potential surrounding the molecule

or fitted to reproduce experimentally measured condensed phase properties, while polarizable force fields specify charge distributions through an induced dipole or Drude oscillator. In reactive force fields, charge distributions are obtained using the charge equilibration method, which assumes that the system is a contiguous conductor and charge transfer can occur across any distance.

Lastly, hydrogen bonds (or H-bonds) are responsible for many of the physical and chemical properties of ILs, such as solubility, ionic conductivity, melting point, viscosity, thermal stability, wettability, and vaporization enthalpy [96, 97]. Hydrogen bonds are identified in a simulation based on hydrogen-to-acceptor distance and acceptor-hydrogen donor angle [98], although the criterion for these two parameters may vary for different systems [1, 69].

These analysis methods have been used separately and in combination to explain observations and trends in physico-chemical properties, as discussed next.

1.4 Physico-Chemical IL Properties

In this section, the properties of phosphonium ILs and their relevance to lubricants will be introduced, along with a brief description of the methods used to calculate each property. Simulation-calculated values for each property will be summarized, in table form, with comparison to experimental data when available. When possible, the accuracy of values obtained with different force fields will be compared. Finally, trends with respect to temperature, interactions with other chemical species, and the anion and cation chemistries will be identified and analyzed.

1.4.1 Density

Density plays a role in how a lubricant functions because it affects fluid flow properties. Also, higher density increases the amount of time it takes for particles to settle out of suspension. As such, high-density fluids exhibit better contamination control by aiding in the suspension, transport, and removal of particulate contaminants [99]. Also, in some applications, density increases the erosive potential of the fluid [100].

Density is the most commonly reported property from MD simulations because it is relatively easy to calculate. Density is obtained from MD simulations at constant temper-

ature and pressure [1]. During such simulations, the volume of the model system varies depending on the temperature and pressure conditions specified. Convergence of the simulations is determined based on the energy and volume reaching steady-state, i.e., fluctuating about a constant value [101]. Then, density is calculated from the volume averaged during steady-state divided by the total mass of atoms in the system [51].

A summary of densities calculated from MD simulations and comparison to experimental data are presented in Table 1.1. The phosphonium ILs in this and all subsequent tables are listed in order of anion type.

For density prediction of phosphonium ILs, the AMBER force field (including GAFF) is the most frequently used potential. The difference between simulation and experimental results for density is typically small (less than 3%) when using this potential. However, some simulations have a relative error of more than 4%, like those for [P1,1,1,6][Tf_2N] and [P4,4,4,4][Gln]. The larger error for [P1,1,1,6][Tf_2N] was attributed to the force field parameters for the carbon atoms bonded to the phosphorus atom [1]. It has also been reported that the accuracy of simulated densities using the AMBER force field could be improved by fine-tuning the interaction parameters [1]. Other potentials, including OPLS, CL&P, APPLE&P, DREIDING, and ReaxFF, have also been used to predict the density of phosphonium ILs. These other potentials predicted density with good accuracy (error less than 2%), although fewer phosphonium ILs have been studied using them compared to AMBER.

From Table 1.1, it can be seen that [P6,6,6,14][Cl] was modeled using OPLS, GAFF and CL&P, with OPLS and CL&P giving more accurate density than GAFF. This suggests that, if parameter sets are available, OPLS and CL&P force fields have higher accuracy for predicting density. Otherwise, the AMBER force field can be used since parameter sets have been developed for a wide range of cations and anions pairs for phosphonium ILs. Although ReaxFF was shown to predict density with reasonable accuracy for [P4,4,4,4][Gly], parameters have not been developed for many different ILs and this force field is less computationally efficient than non-reactive force fields, which limits the size of systems that can be modeled.

The densities reported in Table 1.1 were mostly calculated at a fixed temperature (usually room temperature) to validate the potential [1, 2, 69]. However, there are some studies that simulated the density of phosphonium ILs at different temperatures and showed density decreased with increasing temperature [70, 80, 106], as also observed in experimental stud-

Table 1.1: Density (g/cc) calculated using simulations (Sim) with different potentials at different temperature (Temp, K) compared to data from experiments (Exp) with the difference between them reported as error (%).

IL	Temp	Exp	Sim	Error	Potential	Reference
[P1,1,1,6][Tf_2N]	298	1.34	1.43	6.7	AMBER	[1]
[P2,2,2,1O1][Tf_2N]	298	1.42	1.46	2.8	AMBER	[1]
[P2,2,2,2O1][Tf_2N]	298	1.39	1.44	3.6	AMBER	[1]
[P2,2,2,5][Tf_2N]	298	1.32	1.3	1.5	APPLE&P	[53]
[P2,2,2,5][Tf_2N]	298	1.32	1.35	2.3	AMBER	[1]
[P2,2,2,8][Tf_2N]	298	1.26	1.28	1.6	AMBER	[1]
[P2,2,2,12][Tf_2N]	298	1.21	1.21	0	AMBER	[1]
[P4,4,4,14][Tf_2N]	298	1.125	1.12	1.2	AMBER	[1]
[P6,6,6,14][Tf_2N]	293	1.137	1.083	4.8	AMBER	[80]
[P8,8,8,8][Tf_2N]	298	1.076	1.07	0.5	AMBER	[1]
[P4,4,4,4][2-CNpyr]	333 - 413		0.896 - 0.845		GAFF	[102]
[P4,4,4,4][2-CNpyr-CO_2]	333 - 413		0.958 - 0.908		GAFF	[102]
[P4,4,4,4][BnIm]	333 - 413		0.921 - 0.873		GAFF	[102]
[P4,4,4,4][BnIm-CO_2]	333 - 413		0.981 - 0.931		GAFF	[102]
[P4,4,4,4][BrBnIm]	333 - 413		1.074 - 1.018		GAFF	[102]
[P4,4,4,4][BrBnIm-CO_2]	333 - 413		1.121 - 1.067		GAFF	[102]
[P4,4,4,4][CF_3Pyra]	333 - 413		0.969 - 0.913		GAFF	[102]
[P4,4,4,4][CF_3Pyra-CO_2]	333 - 413		1.02 - 0.964		GAFF	[102]
[P4,4,4,4][Im]	333 - 413		0.889 - 0.839		GAFF	[102]
[P4,4,4,4][Im-CO_2]	333 - 413		0.95 - 0.899		GAFF	[102]
[P4,4,4,4][Leu]	298	0.9269	0.924	0.3	AMBER	[69]
[P4,4,4,4][Ile]	298	0.9296	0.927	0.3	AMBER	[69]
[P4,4,4,4][Ala]	298	0.95	0.942	0.8	AMBER	[69]
[P4,4,4,4][Phe]	298	0.9524	0.98	2.9	AMBER	[69]
[P4,4,4,4][β-Ala]	298	0.959	0.954	0.5	AMBER	[69]
[P1,1,1,1][Gly]	300		1.392		GAFF	[90]
[P1,1,1,1][Gly]+10%H_2O	300		1.388		GAFF	[90]
[P4,4,4,4][Gly]	300	0.963	0.976	1.3	ReaxFF	[3]
[P4,4,4,4][Gly-CO_2]	300		1.000-1.049		ReaxFF	[3]
[P4,4,4,4][Gly]	300	0.963	0.993	3.0	GAFF	[90]
[P4,4,4,4][Gly]+10%H_2O	300		0.99		GAFF	[90]
[P4,4,4,4][Gly]	298	0.963	0.954	0.9	AMBER	[69]
[P4,4,4,4][Lys]	298	0.973	0.962	1.1	AMBER	[69]
[P4,4,4,4][Pro]	298	0.9828	0.963	2.0	AMBER	[69]
[P4,4,4,4][Met]	298	0.9868	0.984	0.3	AMBER	[69]
[P4,4,4,4][Ser]	298	0.991	0.993	0.2	AMBER	[69]
[P4,4,4,4][Glu]	298	1.0121	1.018	0.6	AMBER	[69]
[P4,4,4,4][Asp]	298	1.0173	1.028	1.1	AMBER	[69]
[P4,4,4,4][Tau]	298	1.0199	1.037	1.7	AMBER	[69]
[P4,4,4,4][Gln]	298	1.0519	1.003	4.6	AMBER	[69]
[P4,4,4,8][BMB]	293 - 373	1.0642 - 1.0084	1.0589 - 1.0118	0.5 - 0.3	A&D [1]	[2]
[P4,4,4,14][BMB]	293 - 373	1.0413 - 0.9841	1.0228 - 0.9789	1.8 - 0.5	A&D	[2]
[P6,6,6,14][BMB]	293 - 373	1.0086 - 0.9608	0.9979 - 0.9511	1.1 - 1.0	A&D	[2]
[P4,4,4,8][BScB]	293 - 373	1.0791 - 1.0219	1.0798 - 1.0312	0.1 - 0.9	A&D	[2]
[P4,4,4,14][BScB]	293 - 373	1.0405 - 0.9932	1.0472 - 1.0074	0.6 - 1.4	A&D	[2]
[P6,6,6,14][BScB]	293 - 373	1.0205 - 0.9633	1.0151 - 0.9854	0.5 - 2.3	A&D	[2]
[P4,4,4,8][BMLB]	293 - 373		1.1006 - 1.0578		A&D	[2]
[P4,4,4,14][BMLB]	293 - 373		1.0498 - 1.0011		A&D	[2]
[P6,6,6,14][BMLB]	293 - 373	0.9734 - 0.9265	1.0107 - 0.9683	3.8 - 4.5	A&D	[2]
[P4,4,4,8][BOB]	293 - 373		1.1034 - 1.0601		A&D	[2]
[P4,4,4,14][BOB]	293 - 373		1.0581 - 1.0105		A&D	[2]
[P6,6,6,14][BOB]	293 - 373	0.9973-0.9579 [2]	1.0215 - 0.9874		A&D	[2]
[P6,6,6,14][BOB]	298	0.97	1.01	4.1	A&D	[103]
[P4,4,4,8][Cl]	293 - 343	0.927 - 0.899	0.936 - 0.904	0.9 - 0.5	CL&P	[104]
[P6,6,6,14][Cl]	293	0.882	0.862	1.8	CL&P	[71]
[P6,6,6,14][Cl]	293	0.882	0.846	4.1	GAFF	[71]
[P6,6,6,14][Cl]	293 - 343	0.901 - 0.867	0.892 - 0.864	0.9 - 0.4	CL&P	[104]
[P6,6,6,14][Cl]	298	0.878	0.871	0.8	OPLS/CL&P	[60]
[P6,6,6,14][AcO]	293 - 333	0.902 - 0.875	0.895 - 0.870	0.8 - 0.5	CL&P&OPLS	[104]
[P6,6,6,14][Br]	298	0.958	0.938	2.2	OPLS/CL&P	[60]
[P6,6,6,14][Br]	298	0.958	0.942	1.7	OPLS/CL&P	[105]
[P6,6,6,14][DCA]	298	0.902	0.893	1.0	OPLS/CL&P	[105]
[$HP(Oct)_3$][TFO]	393 -465		0.884 - 0.836		OPLS	[106]
[$HP(Ph)_3$][TFO]	393 -465		1.19 - 1.123		OPLS	[106]

[a] A&D represents for AMBER&DREIDING.

[b] Exp density 293 - 353 K [107].

ies [7, 108–110]. This trend was explained by the fact that interactions between cations and anions become weaker with increasing temperature, as demonstrated by SDF analysis [80].

The presence of water was shown to decrease the density of [P1,1,1,1][Gly] and [P4,4,4,4][Gly] and the effect was attributed to strong interactions between hydrophilic glycinate and water that, in turn, weakened the interactions between the cation and glycinate [90]. It has also been found that chemical adsorption of CO_2 increased the density of five different [P4,4,4,4]-based ILs [102]. ReaxFF parameters were developed specifically to capture the physical and chemical interactions between [P4,4,4,4][Gly] and CO_2 [3]. The simulated reaction pathway for CO_2 and [Gly] anion is shown in Figure 1.4. The trained ReaxFF force field was then used to calculate the density with error less than 1%. The simulations also predicted a significant increase in density with increasing CO_2/IL ratio, larger than predicted by the non-reactive AMBER force field [69]. This larger increase from reactive MD simulations was attributed to bonding between CO_2 and the [Gly] anion, which reduced the volume and thus increased the density of the system [3].

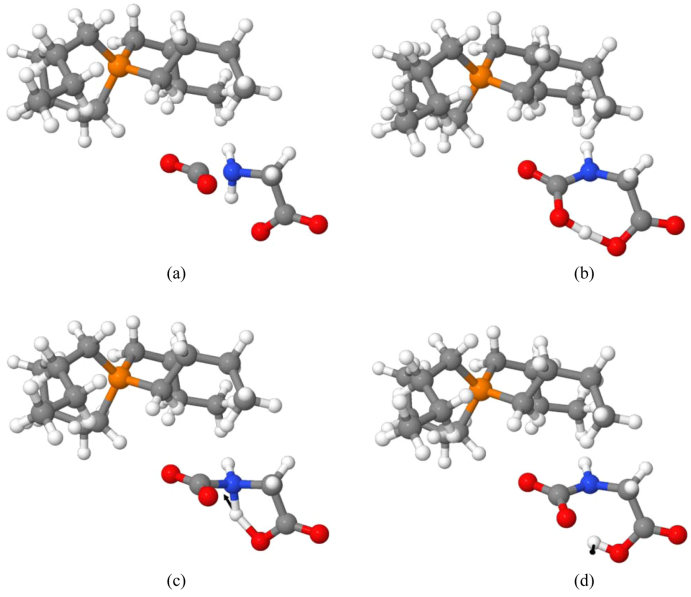

Figure 1.4: Snapshots of [P4,4,4,4][Gly] and CO_2 at different steps in the reaction pathway obtained from a reactive MD simulation [3]. Sphere colors correspond to atoms type: grey C, white H, blue N, red O, and orange P. Figure reprinted with permission from J. Phys. Chem. B 2014, 118, 41, 12008–12016. Copyright 2014 American Chemical Society.

Table 1.1 shows that density depends on both cation and anion. First, it has been reported that density decreases with increasing cation size for the same anion [2, 111].

This trend is observed in Table 1.1 where density increases as [P8,8,8,8] < [P4,4,4,14] < [P2,2,2,12] < [P2,2,2,8] < [P2,2,2,5] < [P1,1,1,6] for [Tf_2N] anions. The same trend is observed for chelated orthoborate anions with density increasing as [P6,6,6,14] < [P4,4,4,14] < [P4,4,4,8]. It was proposed that longer cation alkyl chains increase the interionic separation and lower the packing efficiency, resulting in more volume occupied by the cations and a lower overall density [2, 111, 112].This explanation was supported by an analysis that showed longer cation alkyl chains had lower interaction energies which led to less efficient packing of ions [2].

The anion can also affect density. For non-phosphonium ILs, some studies reported that density increased with the molecular weight of anions [113, 114]. This trend is observed for [P6,6,6,14]-based ILs in Table 1.1, where both density and molecular weight increase as [Cl] < [AcO] < [DCA] < [Br]. Further, for the difference between [DCA] and [Br], RDF peaks for [DCA] were found to be broader and less pronounced than those of [Br]. This trend was attributed to the anion structure. The spherical shape of [Br] had high charge-density, which allowed the ions to come closer to the [P6,6,6,14] cation, whereas the angular shape of [DCA] had a diffused charge distribution, hindered this process which led to a lower density [105].

However, other studies showed results that do not follow this trend [115] or even exhibited the opposite trend [116]. As observed in Table 1.1, for [P4,4,4,8] and [P4,4,4,14] cations, density increases as [BMB] < [BScB] < [BMLB] < [BOB], which is opposite to the trend in their anion mass. Similarly, for [P4,4,4,4] cations with amino acid anions in Table 1.1, density increases as [Leu] < [Ala] < [Gly] and [Phe] < [Met] < [Ser], exhibiting a trend inversely correlated to anion molar mass. The observation may be due to the greater number of carbon atoms in the heavier anions which increased occupied volume, following the same argument as proposed for cations with longer alkyl chains. Therefore, factors other than molar mass, such as atom type and polarity, also need to be considered to understand the effect of the anion on density.

1.4.2 Viscosity

Viscosity is a property of lubricants that quantifies a fluid's resistance to flow. Viscosity directly determines fluid film thickness and viscous friction and so is the dominant factor in tribological behavior, as well as mechanical efficiency in hydraulic applications. The

rate of decrease of viscosity with temperature is particularly important because there is always frictional heating in a sliding contact. At a molecular level, viscosity is due to the interactions between and within molecules (ions) in a fluid. However, there have been fewer simulation studies of phosphonium IL viscosity than density because the simulations of viscosity are more complicated and time-consuming.

There are four main approaches to calculating viscosity in MD simulations. These methods are commonly known as Green-Kubo (GK), Einstein, direct non-equilibrium molecular dynamics (NEMD), and reverse non-equilibrium molecular dynamics (rNEMD) simulations [117]. The first two approaches are equilibrium molecular dynamics (EMD) simulation approaches whereas the last two are non-equilibrium molecular dynamics (NEMD) approaches. EMD approaches are used to calculate viscosity at low shear rates, i.e., Newtonian viscosity, while NEMD approaches are used to calculate viscosity at high shear rates. However, low shear viscosity can be estimated from the NEMD approaches by fitting the high shear rate viscosity data to an empirical equation, such as the Carreau or Eyring equation, and extrapolating back to low shear rates [82, 118, 119].

Both the GK and Einstein approaches calculate low shear viscosity as a function of simulation box volume, Boltzmann constant, temperature, time, and stress. The difference between them is that the GK approach relates the ensemble average of the autocorrelation of stress to viscosity [82, 106], whereas the Einstein approach relates the ensemble average of the mean-square displacement (MSD) of the stress tensor to viscosity [53]. Of the two EMD approaches, GK is more widely used since it is easy to implement and has been reported to accurately predict viscosity when viscosity is relatively low [82, 120]. However, the autocorrelation functions of stress take a long time to converge, especially when the viscosity of the liquids is over 20 mPa·s [121]. In such cases, the Einstein approach is a more computationally efficient and reasonably accurate approach [122, 123].

In NEMD, shear flow simulations are performed by applying the SLLOD equations of motion [124]. The viscosity under high shear rate is obtained as the ratio of the shear stress and the velocity gradient [82]. NEMD was used to model [P6,6,6,14][Im] and [P6,6,6,14][ImC] to compare viscosity before and after CO_2 absorption and showed accuracy less than 20% even for high viscosity [125]. NEMD was also used for [P6,6,6,14][Cl] and [P6,6,6,14][BMB] to cross-check the viscosity results obtained from the GK relation [82]. However, most previous viscosity simulations for phosphonium ILs have used EMD methods.

Table 1.2: Viscosity (mPa·s) calculated using simulations (Sim) with different potentials and calculation methods at different temperatures (Temp, K) compared to data from experiment (Exp) with the difference between them reported as error (%).

IL	Temp	Exp	Sim	Error	Potential	Method	Reference
[P2,2,2,2O1][Tf_2N]	400	3.8	4.1	7.9	AMBER	Green-Kubo	[6]
[P2,2,2,5][Tf_2N]	298	88	80	9.0	APPLE&P	Einstein	[53]
[P2,2,2,5][Tf_2N]	373	5.38	4.98	7.4	OPLS	Einstein	[123]
[P2,2,2,8][Tf_2N]	373	7.49	6.06	19.1	OPLS	Einstein	[123]
[P2,2,2,12][Tf_2N]	373		8.36		OPLS	Einstein	[123]
[P2,2,2,2][PhO]	298 - 420		1.76 - 0.77		OPLS/CL&P	Green-Kubo	[126]
[P3,3,3,3][PhO]	298 - 420		2.09 - 0.83		OPLS/CL&P	Green-Kubo	[126]
[P4,4,4,4][PhO]	298 - 420		2.01 - 0.94		OPLS/CL&P	Green-Kubo	[126]
[P6,6,6,6][PhO]	298 - 420		1.71 - 0.96		OPLS/CL&P	Green-Kubo	[126]
[P8,8,8,8][PhO]	298 - 420		1.15 - 0.98		OPLS/CL&P	Green-Kubo	[126]
[P6,6,6,14][Cl]	323	402	300	25.4	AMBER	Green-Kubo	[82]
[P6,6,6,14][Cl]	343	167	130	22.1	AMBER	Green-Kubo	[82]
[P6,6,6,14][Cl]	363	86	62	27.9	AMBER	Green-Kubo	[82]
[P6,6,6,14][Cl]	383	48	31	35.4	AMBER	Green-Kubo/NEMD	[82]
[P6,6,6,14][Cl]	403	29	13.5	53.4	AMBER	Green-Kubo	[82]
[P6,6,6,14][Cl]	423	18	9.5	47.2	AMBER	Green-Kubo/NEMD	[82]
[P6,6,6,14][Cl]	463	9	4.6	48.9	AMBER	Green-Kubo/NEMD	[82]
[P6,6,6,14][BMB]	373	67	75	11.9	AMBER	Green-Kubo	[82]
[P6,6,6,14][BMB]	383	47	68	44.7	AMBER	Green-Kubo	[82]
[P6,6,6,14][BMB]	403	27	29	7.4	AMBER	Green-Kubo	[82]
[P6,6,6,14][BMB]	423	18	16	11.1	AMBER	Green-Kubo/NEMD	[82]
[P6,6,6,14][BMB]	443	14	12	14.2	AMBER	Green-Kubo	[82]
[P6,6,6,14][BMB]	463	11	6	45.4	AMBER	Green-Kubo	[82]
[P6,6,6,14][Im]	298	810.4	897	11	OPLS	NEMD	[125]
[P6,6,6,14][ImC]	298	648.7	516.9	20	OPLS	NEMD	[125]
[P6,6,6,14][Tf_2N]	273		994.24		AMBER	Einstein	[80]
[P6,6,6,14][Tf_2N]	293	450	735.74	63.5	AMBER	Einstein	[80]
[P6,6,6,14][Tf_2N]	373		201.54		AMBER	Einstein	[80]
[P6,6,6,14][Tf_2N]	473		24.15		AMBER	Einstein	[80]
[P6,6,6,14][Tf_2N]	573		4.91		AMBER	Einstein	[80]
[HP($Oct)_3$][TFO]	393		33.1		OPLS	Green-Kubo	[106]
[HP($Oct)_3$][TFO]	417		25.2		OPLS	Green-Kubo	[106]
[HP($Oct)_3$][TFO]	441		8.8		OPLS	Green-Kubo	[106]
[HP($Oct)_3$][TFO]	465		6.6		OPLS	Green-Kubo	[106]
[HP($Ph)_3$][TFO]	393		14.8		OPLS	Green-Kubo	[106]
[HP($Ph)_3$][TFO]	417		9.3		OPLS	Green-Kubo	[106]
[HP($Ph)_3$][TFO]	441		4.8		OPLS	Green-Kubo	[106]
[HP($Ph)_3$][TFO]	465		3.6		OPLS	Green-Kubo	[106]
[P2($Ph)_3$][PhO]	298 - 420		2.46 - 1.14		OPLS/CL&P	Green-Kubo	[126]
[P3($Ph)_3$][PhO]	298 - 420		2.33 - 1.2		OPLS/CL&P	Green-Kubo	[126]
[P4($Ph)_3$][PhO]	298 - 420		2.5 - 1.15		OPLS/CL&P	Green-Kubo	[126]
[P6($Ph)_3$][PhO]	298 - 420		2.56 - 1.17		OPLS/CL&P	Green-Kubo	[126]
[P8($Ph)_3$][PhO]	298 - 420		1.22 - 1.12		OPLS/CL&P	Green-Kubo	[126]

A summary of Newtonian viscosities calculated from MD simulations and comparison to experimental data is presented in Table 1.2. In terms of simulation methods, the relative error of viscosity calculated from GK theory varies from around 7% to more than 50% for both [P6,6,6,14][Cl] and [P6,6,6,14][BMB] at different temperatures and has 8% error for [P2,2,2,2O1][Tf_2N] at 400 K. With the Einstein relation, viscosity calculations for [P2,2,2,5][Tf_2N] at temperatures of 298 K and 373 K showed good agreement with experimental data, with error less than 10%. However, the error increased to around 20% for [P2,2,2,8][Tf_2N] at 373 K and more than 60% for [P6,6,6,14][Tf_2N] at 293 K. Overall, the GK and Einstein relations give similar accuracy for phosphonium IL viscosity.

As expected, the accuracy of all EMD calculation methods is lower for higher viscosity ILs in Table 1.2. Therefore, equilibrium methods for calculating viscosity are best for modeling phosphonium ILs with low viscosity as well as blends of phosphonium ILs with base oil, whose viscosity is usually much lower than neat ILs.

From Table 1.2, it can be seen that the APPLE&P (polarizable), AMBER, OPLS, and OPLS-based CL&P force fields have been used to simulate viscosity of phosphonium ILs. APPLE&P exhibited good agreement with experimental study, even though the viscosity is over 20 mPa·s. However, only [P2,2,2,5][Tf_2N] has been studied using this potential. The AMBER, OPLS, and CL&P force fields have been used more frequently. However, their overall accuracy, which decreases as viscosity increases, is lower than that for APPLE&P for [P2,2,2,5][Tf_2N]. This is consistent with previous studies that reported polarizable force fields are better able to model the physico-chemical properties of ILs [2, 53–57].

Like density, some studies only calculated the viscosity of phosphonium ILs at a specific temperature. However, there are a few studies that simulated the change of viscosity with temperature. For example, Table 1.2 reports the viscosity of [P6,6,6,14][Tf_2N] from 273 to 573 K, [P6,6,6,14][Cl] from 323 to 463 K and [$HP(Oct)_3$][TFO] from 393 to 465 K. Consistent with physical observations, MD simulations predict the viscosities of these phosphonium ILs decrease rapidly with increasing temperature. This trend was also reflected in an RDF analysis for [P6,6,6,14][Tf_2N] where the height of the first peak of H_{cation}-O_{anion}s RDFs decreased with temperature, indicating that interactions between cation and anion became weaker with increasing temperature, therefore contributing to lower viscosity [80].

It has been reported that chemical adsorption of CO_2 decreased the viscosity of [P6,6,6,14][Im]. This was explained by RDFs and SDFs that showed the anions became asymmetric after

reaction with CO_2, which weakened the interaction between the phosphorus atom and the nitrogen atom of the anion. This weakened interaction led to faster dissociation of cation-anion pairs, thereby accelerating dynamics and lowering viscosity [125].

For the effect of cation on viscosity, it has been reported that higher symmetry or longer alkyl moieties in the cation generally lead to higher viscosity for a given anion [127–129]. This is seen in Table 1.2 where viscosity increases as [P2,2,2,5][Tf_2N] < [P2,2,2,8][Tf_2N] < [P2,2,2,12][Tf_2N] at 373 K and [P2,2,2,2][PhO] < [P3,3,3,3][PhO] < [P4,4,4,4][PhO] < [P6,6,6,6][PhO] < [P8,8,8,8][PhO] at 420 K. However, there are some exceptions; for example, [P6,6,6,6][PhO] and [P8,8,8,8][PhO] at 298 K. Table 1.2 also shows that, for the [Tf_2N] anion, viscosity is lower for [P2,2,2,2O1] than [P2,2,2,5], consistent with a previous report that the presence of alkyl ether chains decreases viscosity compared to alkyl chains [89].

For [P2,2,2,5], [P2,2,2,8], and [P2,2,2,12] paired with [Tf_2N], the effect of cation chain length on viscosity was analyzed using interionic interaction energy, RDFs for P_{cation}-N_{anion} and H_{cation}-O_{anion}, and hydrogen bonding [1]. It was found that the viscosity and interaction energy exhibited the same trend which suggested that the relatively high viscosities of ILs may due to the strong interactions between ions, consistent with a previous study that showed higher interionic interaction energy is correlated to higher viscosity for [EMIM]-based ILs [92]. Coordination numbers calculated by integrating RDFs showed that cations with shorter alkyl chain lengths were likely to be surrounded by more anions and molecule flowability increased as a result, leading to a lower viscosity. Lastly, stronger hydrogen bonding usually correlates to higher viscosity for different anions paired with the same cation [69, 130].

In a study of halogen-free chelated orthoborate-phosphonium ILs, the P_{cation}-B_{anion} RDFs for cations with longer alkyl chains exhibited a higher first peak and lower first minimum for the same anion [2]. This is in agreement with the trend that cations with larger alkyl groups have higher viscosity. In another study, the viscosity of [P2,2,2,5][Tf_2N] was found to be nearly twice that of [P2,2,2,2O1][Tf_2N] [90]. This was correlated to the P_{cation}-N_{anion} RDFs for which [P2,2,2,5][Tf_2N] had a higher first peak [89]. RDFs of P_{cation}-$C\alpha_{anion}$ for [P1,1,1,1][Gly] and [P4,4,4,4][Gly] showed that the first peak was higher but at a longer distance for [P4,4,4,4][Gly]. This was believed to be caused by longer alkyl chains in the cations, which had stronger interactions with the anion even at a farther distance [90].

For the effect of anions, it has been reported earlier that viscosity increases with number

of hydrogen bonds, as observed for structurally similar anions paired with [P4,4,4,4] where the viscosity increased as [Gln] > [Glu] > [Lys] > [Ser] [69]. From Table 1.2, at room temperature, tetraalkylphosphonium (like [P2,2,2,2]) ILs with [PhO] anion have very low viscosity (about 2 mPa·s), while tetraalkylphosphonium ILs with other anions (like [Cl], [BMB], and [Tf_2N]) have a viscosity over 75 mPa·s. Another observation from Table 1.2 is that viscosity increases as [P6,6,6,14][BMB] < [P6,6,6,14][Cl] < [P6,6,6,14][Tf_2N] at around 373 K. However, this trend is inconsistent with experimental data that showed the viscosity of [P6,6,6,14][Tf_2N] is lower than that of [P6,6,6,14][Cl] [36, 131] at 298 K, indicating temperature also affecting viscosity trends. Further, these anions have significant structural differences that are likely to affect the viscosity more than hydrogen bonding. Therefore, additional simulation works should be carried out, ideally with anions for which the key difference is hydrogen bonding, to confirm the trends.

1.4.3 Self-diffusivity

Self-diffusivity describes the rate of net movement of molecules from a higher concentration region to a lower concentration region. This property is quantified by the self-diffusion coefficient. Te self-diffusion coefficient has been found to be proportional to temperature and inversely proportional to viscosity [53]. Self-diffusivity has been studied in MD simulations for phosphonium ILs to evaluate the ability of a given force field to predict transport properties or to explain observed trends [2, 53].

In MD simulations, the self-diffusion coefficient is usually calculated using the Einstein relation based on the mean-square displacement (MSD) of the center-of-mass of the ions [2, 53, 71, 132]. It can also be calculated by the time integral of the velocity autocorrelation function using the GK expression [74]. However, self-diffusion coefficients calculated using GK are typically higher than those obtained from the Einstein relation [74]. The self-diffusion coefficient is calculated separately for the cation and anion.

A summary of self-diffusion coefficients of phosphonium ILs from MD simulation is presented in Table 1.3. There are very few experimentally measured self-diffusion coefficients reported that can be used to evaluate the accuracy of model predictions, so error is not reported in Table 1.3. However, reference data is available for [P2,2,2,2O1][Tf_2N] [6]. For this IL, the self-diffusion coefficient was calculated using the AMBER force field to be 450×10^{-12} m^2/s for the anion and 410×10^{-12} m^2/s for the cation. These are larger than

Table 1.3: Self-diffusion coefficient ($10^{-12}m^2/s$) of cations and anions calculated using simulations (Sim) with different potentials at different temperatures (Temp, K).

IL	Temp	Cation	Anion	Potential	Reference
[P2,2,2,2O1][Tf_2N]	400	410	450	AMBER	[6]
[P2,2,2,5][Tf_2N]	298	8.5	10.1	APPLE&P	[53]
[P2,2,2,5][Tf_2N]	373	29.2	34.8	OPLS/CL&P	[123]
[P2,2,2,8][Tf_2N]	373	20	30.2	OPLS/CL&P	[123]
[P2,2,2,12][Tf_2N]	373	13.9	20.8	OPLS/CL&P	[123]
[P6,6,6,14][Tf_2N]	298 - 398	1.33 - 14.37	1.45 - 10.75	CL&P	[71]
[P6,6,6,14][Tf_2N]	273 - 573	2.08 - 421.44	2.08 - 421.44	AMBER	[80]
[P4,4,4,8][BMB]	333	2.634	3.237	A&D [1]	[2]
[P4,4,4,14][BMB]	333	2.066	2.711	A&D	[2]
[P6,6,6,14][BMB]	333	2.737	3.215	A&D	[2]
[P4,4,4,8][BMLB]	333	1.648	1.825	A&D	[2]
[P4,4,4,14][BMLB]	333	1.78	2.588	A&D	[2]
[P6,6,6,14][BMLB]	333	2.645	2.818	A&D	[2]
[P4,4,4,8][BOB]	333	2.079	3.63	A&D	[2]
[P4,4,4,14][BOB]	333	5.521	7.357	A&D	[2]
[P6,6,6,14][BOB]	333	2.054	2.254	A&D	[2]
[P4,4,4,8][BScB]	333	3.28	3.431	A&D	[2]
[P4,4,4,14][BScB]	333	2.645	2.851	A&D	[2]
[P6,6,6,14][BScB]	333	3.073	4.178	A&D	[2]
[P2,2,2,2][PhO]	298 - 420	37 - 611	36.7 - 827	OPLS/CL&P	[126]
[P3,3,3,3][PhO]	298 - 420	5.1 - 371	6.5 - 532	OPLS/CL&P	[126]
[P4,4,4,4][PhO]	298 - 420	1.2 - 161	2.1 - 269	OPLS/CL&P	[126]
[P6,6,6,6][PhO]	298 - 420	0.9 - 67	1.3 - 122	OPLS/CL&P	[126]
[P8,8,8,8][PhO]	298 - 420	0.7 - 32	1.1 - 42	OPLS/CL&P	[126]
[P2($Ph)_3$][PhO]	298 - 420	0.9 - 221	1.0 - 265	OPLS/CL&P	[126]
[P3($Ph)_3$][PhO]	298 - 420	0.5 - 147	0.9 - 191	OPLS/CL&P	[126]
[P4($Ph)_3$][PhO]	298 - 420	0.5 - 128	1.2 - 209	OPLS/CL&P	[126]
[P6($Ph)_3$][PhO]	298 - 420	0.5 - 100	0.9 - 182	OPLS/CL&P	[126]
[P8($Ph)_3$][PhO]	298 - 420	1.3 - 81	1.5 - 179	OPLS/CL&P	[126]
[P4,4,4,4][BnIm]	413	45.3	75.1	Class I	[102]
[P4,4,4,4][BnIm]+H_2O	413	47.5	89.9	Class I	[102]
[P4,4,4,4][BnIm-CO_2]	413	43.2	66.6	Class I	[102]
[P4,4,4,4][BnIm-CO_2]+H_2O	413	45.1	68.3	Class I	[102]
[P4,4,4,4][2-CNpyr]	333 - 413	8.6 - 99.6	13.1 - 150.6	GAFF	[70]
[P4,4,4,4][2-CNpyr]	413	78.5	145.4	Class I	[102]
[P4,4,4,4][2-CNpyr]+H_2O	413	95.4	161.5	Class I	[102]
[P4,4,4,4][2-Cnpyr-CO_2]	413	67.3	102.3	Class I	[102]
[P4,4,4,4][2-Cnpyr-CO_2]+H_2O	413	69.6	103.4	Class I	[102]
[P2,2,2,8][2-CNpyr]	333	33	47	Class I	[133]
[P2,2,2,8][2-CNpyr]+H_2O	333	44	70	Class I	[133]
[P2,2,2,8][3Triaz]	333	13	13	Class I	[133]
[P2,2,2,8][3Triaz]+H_2O	333	22	37	Class I	[133]
[P2,2,2,8][PhO]	333	26	30	Class I	[133]
[P2,2,2,8][PhO]+H_2O	333	23	34	Class I	[133]
[P1,1,1,1][Gly]	300	0.2	0.2	AMBER	[90]
[P1,1,1,1][Gly]+H_2O	300	0.3	0.2	AMBER	[90]
[P4,4,4,4][Gly]	300	0.8	0.7	AMBER	[90]
[P4,4,4,4][Gly]+H_2O	300	0.7	0.8	AMBER	[90]

[a] A&D represents for AMBER&DREIDING.

the experimental values of 340 $\times$ 10^{-12} m^2/s for the anion and 290 $\times$ 10^{-12} m^2/s for the cation [6].

For the influence of temperature, the self-diffusion coefficients of both cation and anion in phosphonium ILs increase with temperature, as observed for ILs like [P6,6,6,14][Tf_2N] and [P4,4,4,4][2-CNpyr] in Table 1.3. Further, the rate of increase of self-diffusion coefficient with temperature is faster at higher temperatures [70, 71, 80].

Self-diffusion and viscosity are inversely related [53]. In Table 1.3, for [P4,4,4,8] and [P4,4,4,14] cations, the self-diffusion coefficient is larger for [BScB] than [BMB]. The self-diffusion coefficients of these ILs exhibit the opposite trend with the viscosity of [BMB] larger than [BScB] [42]. The same inverse relationship is observed for [P6,6,6,14] ILs, for which the self-diffusion coefficients increase as [BOB] < [BMLB] < [BMB] < [BScB], while viscosity exhibits the opposite trend [42]. These results confirm that self-diffusion coefficient phosphonium ILs are generally inversely proportional to viscosity.

The presence of water is expected to increase self-diffusivity because the addition of water decreases counterion association, thereby allowing ions to diffuse more freely. For example, the self-diffusion coefficients of both the cation and anion increased when water was present in [P2,2,2,8][2-CNpyr] and [P2,2,2,8][3-Triaz] systems, with the anions exhibiting a larger increase [133]. The same trends were observed in an earlier study with [P4,4,4,4][2-CNpyr] and [P4,4,4,4][BnIm] ILs [102]. However, for ions with low self-diffusivity, the effect of water can be negligible. For example, the ions in [P1,1,1,1][Gly] and [P4,4,4,4][Gly] had similar self-diffusion coefficients in neat form and with 10% water [90].

The self-diffusion coefficients of ions were compared to that of water for [P4,4,4,4][2-CNpyr] and [P4,4,4,4][BnIm] ILs [102], and [P1,1,1,1][Gly] and [P4,4,4,4][Gly] [90]. In all cases, water diffused much faster than either ion. This is consistent with the fact that the ions are much larger than the water molecules [102]. Further, for [P4,4,4,4][2-CNpyr] and [P4,4,4,4][BnIm], the self-diffusion coefficient for water in [P4,4,4,4][2-CNpyr] was higher because of the hydrophobicity of the IL. Although hydrogen bond formation was found between water and the anions, cation–anion center-of-mass RDFs showed that the water did not affect the overall structure of the ILs [102].

As seen in Table 1.3, the self-diffusion coefficients of cations and anions are not the same for a given IL and that most anions have higher diffusion coefficients than cations in phosphonium ILs. It has been proposed that this is due to the fact that anions do not have

long alkyl chains and occupy a smaller volume, so they experience less steric hindrance and are able to move more easily than cations [71], suggesting that the shape of the ions plays an important role [102]. The only outlier in Table 1.3 is [P6,6,6,14][Tf_2N], where [P6,6,6,14] has a higher diffusion coefficient than [Tf_2N] at 398 K. This is due to the fact that the self-diffusion coefficient increased faster with temperature for the [P6,6,6,14] cation than the [Tf_2N] anion [71].

For the cations, self-diffusion coefficients are smaller for longer alkyl chains. For example, the self-diffusion coefficient decreases as [P2,2,2,5] > [P6,6,6,14] for the [Tf_2N] anion, [P2,2,2,8] > [P4,4,4,4] for the [2-CNpyr] anion, and [P2,2,2,2] > [P3,3,3,3] > [P4,4,4,4] > [P6,6,6,6] > [P8,8,8,8] for the [PhO] anion. This is consistent with the observed increase of viscosity with cation alkyl chain length, since self-diffusion coefficients and viscosity are inversely related [76, 80]. Therefore, the self-diffusion trends for cations may be explained using the same mechanisms as proposed for viscosity.

There is no consistent trend observed for the anions in Table 1.3. For example, the self-diffusion coefficient increases as [BMLB] < [BMB] < [BScB] < [BOB] for [P4,4,4,8] and [P4,4,4,14] cations, but the trend is [BOB] < [BMLB] < [BMB] < [BScB] for the [P6,6,6,14] cation. It is also observed that, for the [P2,2,2,8], the self-diffusion coefficient increases as [3Triaz] < [PhO] < [2-CNpyr]. However, there is no clear explanation for this trend.

1.4.4 Ionic Conductivity

Ionic conductivity is a measure of the IL's ability to conduct electricity. Ionic conductivity is important for lubricants that operate in the presence of electric contact [134]. For example, in electric motors, rolling bearings and their lubricants are subjected to stray current, which can lead to bearing damage. Usually, lubricants with moderate ionic conductivity are preferred to minimize static charge while also avoiding short-circuiting of lubricated contacts [135, 136].

There are various EMD simulation approaches for calculating ionic conductivity of a material, including GK, Einstein, and Nernst-Einstein. Like viscosity and thermal conductivity, the GK formula relates the time integral of the autocorrelation of electric current to the ionic conductivity [106, 137] whereas the Einstein equation relates the mean square displacement of electric current [53, 137, 138]. The Nernst-Einstein equation is a more

computationally efficient approach that relates the the self-diffusion coefficient of anions and cations and their charges to ionic conductivity [138, 139] if translation of counterions is excluded from the calculated diffusion coefficient [138].

A summary of the ionic conductivity of phosphonium-based ILs from MD simulation is presented in Table 1.4. Currently, there are only two previous studies that compared ionic conductivity between MD simulations and experiments. For [P2,2,2,5][Tf_2N], the difference between experiment and simulation was reported to be 23% [53], and for [P2,2,2,2O1][Tf_2N] it was around 40% [6]. Generally, the conductivity of ILs increases with temperature [80, 106] since temperature increases the mobility of the ions. This trend can be seen for the ILs in Table 1.4.

From the Einstein relation, ionic conductivity is proportional to self-diffusivity and inversely proportional to viscosity [76, 80]. This relationship can be seen by comparing the ionic conductivity in Table 1.4 and the viscosity in Table 1.2 for [P2,2,2,5][Tf_2N] and [P2,2,2,2O1][Tf_2N]. The high ionic conductivity and lower viscosity of [P2,2,2,2O1][Tf_2N] was attributed to the higher ionic mobility of the alkyl ether chain in the [P2,2,2,2O1] compared to the alkyl chain in the [P2,2,2,5] [89]. It was also found the addition of [Li] cation decreased ionic conductivity and increased viscosity for [P2,2,2,2O1][Tf_2N] [89]. Both trends are attributable to the strong interactions between the metallic cation and the [Tf_2N] anion.

For the effect of cation, it is observed in Table 1.4 that ionic conductivity decreases with cation alkyl chain length as [P2,2,2,5] > [P2,2,2,8] > [P2,2,2,12] with [Tf_2N]. The higher viscosity of ILs with longer cation alkyl chains have higher viscosity which hinders ionic mobility leading to lower ionic conductivity. For the effect of anions, currently there are too few MD simulation studies to identify trends. Future studies may analyze trends among anions in terms of previously reported correlations between ionic conductivity and both interionic interaction energy [86] and hydrogen bonding [69, 97].

1.4.5 Heat Capacity

Heat capacity is a measure of the amount of heat energy required for a unit change in temperature. Usually, higher heat capacity helps a lubricating oil to carry heat away from a sliding interface, thereby extending the life of mechanical parts. In MD simulations, constant-pressure heat capacity is calculated from the rate of change of the enthalpy of the

Table 1.4: Ionic conductivity (S/cm) calculated using simulations (Sim) with different potentials at different temperatures (Temp, K) and compared to data from experiments (Exp) and the difference between them reported as error (%).

IL	Temp	Exp	Sim	Error	Potential	Reference
[P2,2,2,5][Tf_2N]	298	0.00173	0.00134	23%	APPLE&P	[53]
[P2,2,2,5][Tf_2N]	298 -361		0.0021 - 0.01169		AMBER	[89]
[P2,2,2,5][Tf_2N]	373		0.0192		OPLS/CL&P	[123]
[P2,2,2,8][Tf_2N]	373		0.0151		OPLS/CL&P	[123]
[P2,2,2,12][Tf_2N]	373		0.0104		OPLS/CL&P	[123]
[Li]0.25[P2,2,2,2O1]0.75[Tf_2N]	298 -361		0.000612 - 0.00721		AMBER	[89]
[Li]0.39[P2,2,2,2O1]0.61[Tf_2N]	298 -361		0.000159 - 0.00353		AMBER	[89]
[P2,2,2,2O1][Tf_2N]	400 K	0.0302	0.0425	40%	AMBER	[6]
[P2,2,2,2O1][Tf_2N]	298 -361		0.00384 - 0.0184		AMBER	[89]
[Li]0.25[P2,2,2,2O1]0.75[Tf_2N]	298 -361		0.00142 - 0.01177		AMBER	[89]
[Li]0.39[P2,2,2,2O1]0.61[Tf_2N]	298 -361		0.00037 - 0.00501		AMBER	[89]
[P6,6,6,14][Tf_2N]	273 -573		0.000002 - 0.000383		AMBER	[80]
[$HP(Oct)_3$][TFO]	393 - 465 K		0.00045 - 0.0044		OPLS	[106]
[$HP(Ph)_3$][TFO]	393 - 465 K		0.002- 0.0138		OPLS	[106]

system with temperature [69, 80, 140].

A summary of the heat capacities of phosphonium ILs from MD simulations with comparisons to experimental data is presented in Table 1.5. Currently, only the AMBER and GAFF force fields have been used to calculate heat capacity for phosphonium ILs. GAFF was used to calculate the heat capacity of [P4,4,4,4][2-CNpyr], but there is no experimental data available to evaluate the accuracy of the predictions. The AMBER force field was used to calculate the heat capacity of [P4,4,4,4]-based ILs, with relative error ranging from 1% to 12% for most anions, but 18% error for [Gly] and more than 40% error for [Lys]. However, for [P4,4,4,4][Lys], another experimental study [141] reported heat capacity much closer to the simulation-calculated value, leading to error of less than 5%.

The heat capacity of phosphonium ILs has been reported to increase with temperature from experimental studies [7, 142, 143], but no MD simulation studies have investigated trend. Chemical adsorption of CO_2 has been shown to increase the heat capacity of [P4,4,4,4][2-CNpyr] [70]. The increase in heat capacity was attributed to the ions being slightly farther apart with little change to the nonbonded van der Waals and electrostatic interactions. This caused the [P4,4,4,4][2-CNpyr-CO_2] to require more heat to increase temperature than the unreacted system [70].

For the effect of the cation, the results in Table 1.5 show that the heat capacities of [P4,4,4,4]-based ILs are higher than those of [P6,6,6,14]-based ILs, suggesting that heat capacity decreases with increasing cation alkyl chain length. However, additional simu-

lations should be carried out to confirm the trend for other anions. In Table 1.5, the heat capacity for [P4,4,4,4] cations increases as [Glu] < [Asp] < [Leu] < [Ala], which is opposite to the anion mass trend [69]. This trend too could be investigated with future simulations of ILs with similar anion structures.

Table 1.5: Heat capacity (J/(K·g)) calculated using simulations (Sim) with different potentials at different temperatures (Temp, K) and compared to data from experiment (Exp) and the difference between them reported as error (%).

IL	Temp	Exp	Sim	Error	Potential	Reference
[P4,4,4,4][Lys]	310	1.8434	2.63405	42.9	AMBER	[69]
[P4,4,4,4][Lys]	310	2.5198	2.63405	4.4	AMBER	[141]
[P4,4,4,4][Gly]	310	2.1422	2.52506	17.8	AMBER	[69]
[P4,4,4,4][Gln]	310	2.1748	2.41312	11.0	AMBER	[69]
[P4,4,4,4][Glu]	310	2.2223	2.4051	8.2	AMBER	[69]
[P4,4,4,4][Pro]	310	2.2336	2.4931	11.6	AMBER	[69]
[P4,4,4,4][Tau]	310	2.2403	2.46605	10.1	AMBER	[69]
[P4,4,4,4][Ile]	310	2.3186	2.51507	8.5	AMBER	[69]
[P4,4,4,4][Leu]	310	2.3591	2.56406	8.7	AMBER	[69]
[P4,4,4,4][Ser]	310	2.3599	2.46806	4.6	AMBER	[69]
[P4,4,4,4][Met]	310	2.4424	2.47605	1.4	AMBER	[69]
[P4,4,4,4][Ala]	310	2.4582	2.58707	5.2	AMBER	[69]
[P4,4,4,4][β-Ala]	310	2.4577	2.66508	8.4	AMBER	[69]
[P4,4,4,4][Asp]	310		2.45209		AMBER	[69]
[P4,4,4,4][Phe]	310	2.6112	2.41506	7.5	AMBER	[69]
[P4,4,4,4][2-CNpyr]	333 - 413		2.237		GAFF	[70]
[P4,4,4,4][2-CNpyr-CO_2]	333 - 413		2.396		GAFF	[70]
[P6,6,6,14][Tf_2N]	273 - 573	1.79 - 2.04	2.078	8.3	AMBER	[80]

1.4.6 Water Solubility

Water is widely used during IL synthesis [144–147], and many ILs have high water affinity. Consequently, it can be difficult to remove water from a produced IL which can then significantly affect properties including density, viscosity, polarity, conductivity, and solubility [7, 96, 102, 133]. The solubility of ILs in water is also very important for reducing emulsification when preparing water-based lubricants [148].

The water solubility of five different [P4,4,4,4]-based ILs was compared based on the solvation free energy of water going from an ideal gas state to dissolved in IL. It was found that [2-CNpyr] had the lowest water solubility, while [BnIm] had highest water solubility [102]. Another study compared the solubility of ILs with [P4,4,4,4] cation and three different anions [91]. Results showed that [P4,4,4,4][CF_3COO] was completely miscible with water, [P4,4,4,4][CF_3COO]-H_2O was partially miscible with water, and [P4,4,4,4][PF_6] was not soluble in water. Analysis showed that cation-anion and anion-H_2O interactions

were primarily electrostatic, while van der Waals interactions were dominant for cation-H_2O [91].

MD simulations were used to study the mixing behavior between water and phosphonium ILs with chloride and acetate anions. While the anions were well solvated with water due to their small size, only the smallest cation [P2,2,2,2] was completely miscible with water forming a homogeneous binary solution. As the length of cation alkyl chain increased, the size of heterogeneous domains increased and ultimately led to stable interfaces between water and ILs [104]. Chemical reaction with CO_2 has been found to increase water solubility of [P4,4,4,4]-based ILs. Among several ILs studied, the increase of water solubility due to CO_2 was largest for the [2-CNpyr] anion [102].

Hydrogen bond analysis has been widely used to study interactions between ions and H_2O. Particularly, hydrogen bonding between water and anions can weaken the interactions between cations and anions [4, 91]. This relationship is shown in Figure 1.5 for [P6,6,6,14][BOB] where the effect of water is observed to be highly dependent on water concentration. This dependence was attributed to the competition between hydrogen-bond interactions, electrostatic interactions between the polar segments in the ionic species, and dispersion interactions between the hydrophobic alkyl chains in the cations [4]. Simulations of [P6,6,6,14]-orthoborate in water showed that, even after the bulk water was removed, some water molecules were trapped between the adjacent ionic species [81]. The number of hydrogen bonds between the ILs and water molecules was found to decrease rapidly with increasing temperature for [P4,4,4,4] paired with [CF_3COO], [CH_3COO], and [PF_6] [91].

1.4.7 Thermal Stability

The thermal stability of phosphonium ILs is important for their application as lubricants because chemical decomposition causes lubrication performance decreasing over time. Although there are quantum chemistry simulations and ab initio MD simulations studying thermal degradation of phosphonium ILs [149–152], classical MD simulation studies using an empirical force field are very limited. This is largely because thermal decomposition involves bond dissociation which cannot be modeled using non-reactive simulations.

An alternative simulation approach is reactive MD that can capture chemical reactions [153, 154]. Especially, reactive MD simulations using ReaxFF [83] have been used

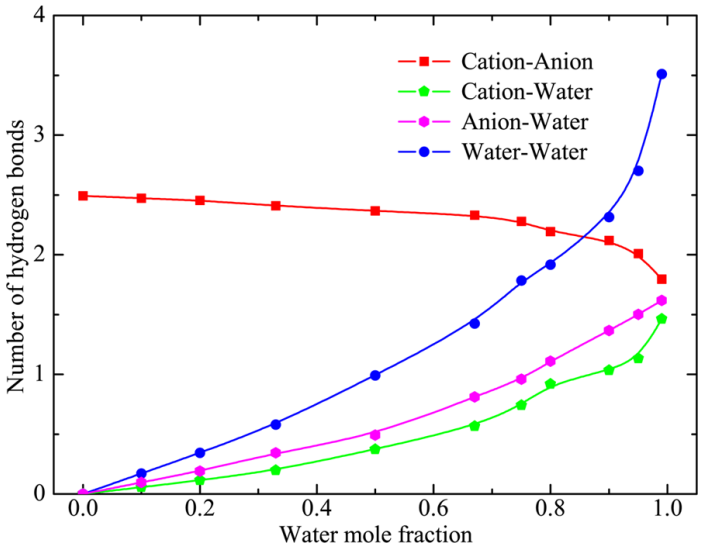

Figure 1.5: Number of hydrogen bonds in the cation-anion, cation-water, anion-water, and water-water pairs calculated from the [P6,6,6,14][BOB] IL/water mixtures as a function of water mole fraction [4]. Figure reprinted with permission from J. Phys. Chem. B 2015, 119, 16, 5251–5264. Copyright 2015 American Chemical Society.

to investigate thermal decomposition of various chemical species, including hydrocarbon fuels [155–157], polymers [158], insulation gas [159], refrigerants [160, 161], energetic materials [162, 163], and phosphate-based lubricant additives [85, 164]. One ReaxFF parameter set has been developed specifically for a phosphonium IL [3].

In a recent study, ReaxFF simulations with this parameter set were used to compare thermal decomposition of [Benz] and [Sali] anions with three phosphonium cations [5]. Simulation results and experimental measurements showed that the [Benz] ILs were less thermally stable than the [Sali] ILs, but there was little effect of the cation. Then, the simulations were used to isolate decomposition reaction pathways, one of which is shown for [P4,4,4,4] [Sali] in Figure 1.6. It was found that the hydroxyl groups in the [Sali] hindered proton transfer, thereby decreasing the likelihood of subsequent decomposition reactions [5].

1.4.8 Interactions with Solid Surfaces

The MD simulation studies covered so far have focused on predicting and understanding the physico-chemical properties of bulk phosphonium ILs. However, lubricating fluids are of-

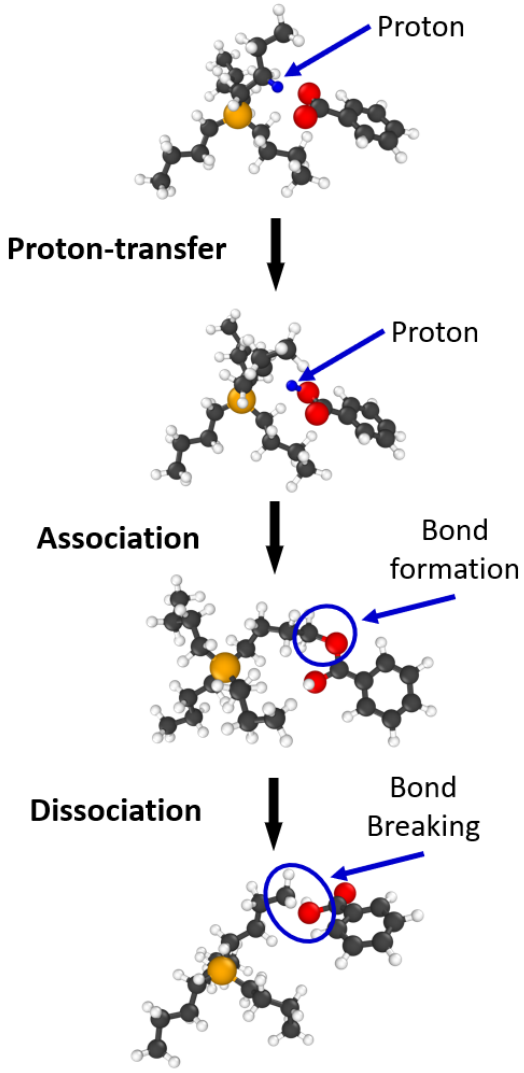

Figure 1.6: Representative thermal decomposition pathway for [P4,4,4,4] [Sali] obtained from reactive MD simulations [5]. Sphere colors correspond to atoms type: black C, white H, red O, and orange P.

ten interacting with solid surfaces and confined to very narrow gaps between those surfaces during operation. This confinement can affect their material properties and also directly relates to tribological parameters such as friction and wear. Several previous studies have explored the frictional behavior of confined ammonium and imidazolium ILs [165–169].

One MD simulation study investigated the wetting of [P2,2,2,5][Tf_2N] on face-centered cubic platinum surfaces [170]. They found that contact angle was smaller on (111) orientated surfaces than (100) surfaces, as shown in Fig 1.7. Regardless, the contact angle was much lower than 90°on both surfaces, indicating [P2,2,2,5][Tf_2N] exhibited favorable wettability and hydrophilicity.

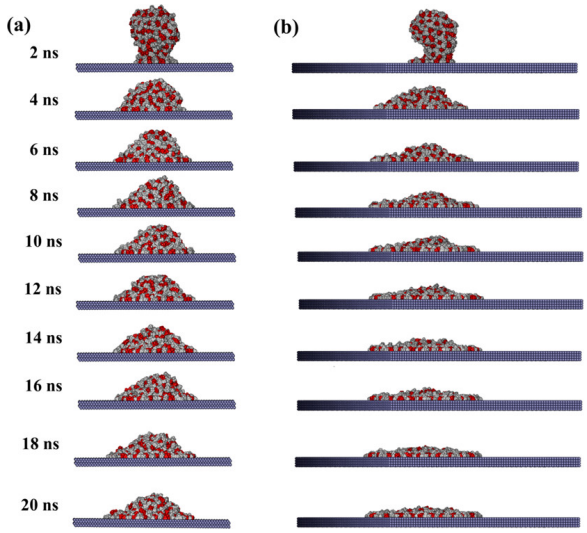

Figure 1.7: Dynamic spreading of a [P2,2,2,5][Tf_2N] IL nanodroplet on (a) Pt(100) and (b) Pt(111) surfaces [6]. Sphere colors correspond to items type: white [P2,2,2,5]; red [Tf_2N]; ice blue Pt. Figure reprinted with permission from J. Phys. Chem. B 2020, 124, 14, 2835–2847. Copyright 2020 American Chemical Society.

Simulations of phosphonium ILs confined to nanoscale gaps have also been performed, although not specifically related to lubrication. One study investigated the structure and capacitive behavior of phosphonium ILs confined between planar and porous graphene electrodes, as shown in Fig 1.8. It was found that the [P2,2,2,2O1][Tf_2N] ILs formed layers adjacent to the planar graphite electrodes but this ordering was disrupted by confinement between narrow nanoporous electrodes. Further, the differential capacitance on the negative electrode was lower than on the positive electrode, which was attributed to the larger size of the [P2,2,2,2O1] cations relative to the [Tf_2N] anions that prevented effi-

cient packing [6]. In another study, the interfacial ionic structure, molecular arrangement, and orientation of [P6,6,6,14][BMB] confined between neutral and charged gold electrodes was investigated. For both neutral and charged electrodes, the hexyl and tetradecyl chains in [P6,6,6,14] cations laid preferentially flat on the surface due to their elongated molecular conformation. In contrast, the [BMB] anions exhibited alternating parallel-perpendicular orientations adjacent to the neutral electrodes and gradually reached a parallel coordination pattern at the positively charged electrodes [171].

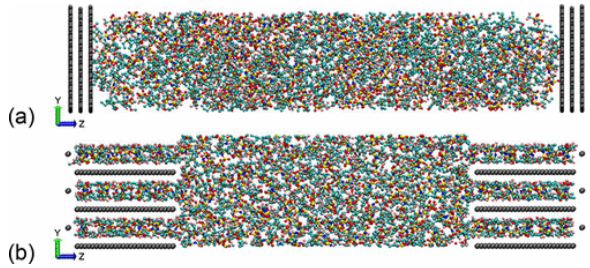

Figure 1.8: Snapshots of simulations of [P2,2,2,2O1][Tf_2N] confined between (a) planar and (b) porous electrodes [6]. Sphere colors correspond to items type: black electrodes; other colors [P2,2,2,2O1][Tf_2N] ILs. Figure reprinted with permission from J. Phys. Chem. C 2019, 123, 17, 10816–10825. Copyright 2019 American Chemical Society.

1.4.9 Summary of Previous MD Studies of Phosphonium ILs

In general, existing MD simulations of phosphonium IL are focused on predicting and understanding physico-chemical properties that are important for multiple current and potential applications of ILs. Previous simulations have used both non-reactive and reactive force fields, including AMBER, GAFF, OPLS, DREIDING, CL&P, APPLE&P, and ReaxFF.

The most frequently reported property is density and the simulation process is relatively simple and not time consuming. Density is often used as a first evaluation of the accuracy of a force field. The AMBER force field has been used most often and shown to predict density with error less than 3% for most ILs. However, for [P6,6,6,14][Cl], a comparison of multiple force fields showed that OPLS and CL&P were more accurate. Density was found to decrease due to the presence of water but increase when ILs chemically react with CO_2. An analysis of results for various ILs showed that density decreased with increasing cation size. This trend was attributed to higher interionic separation, quantified by interionic interaction energies and the position of the first cation-anion RDF peak, leading to

lower packing density. A similar trend was observed for some anions where density decreased with increasing anion molar mass. But this trend was not always found, suggesting factors other than ion size are likely contributing. Generally, MD simulations can successfully predict density for phosphonium ILs and explain the effect of the cation. However, additional studies are needed to understand the effect of the anion on density.

Simulations have also been widely used to study the viscosity, perhaps the most important property of lubricating fluids. Although both equilibrium and non-equilibrium simulation methods are available for calculating viscosity, at this point, equilibrium simulations with the Green-Kubo method have been most often used to model phosphonium ILs. The error of viscosity calculated is higher than that reported for density, with error commonly above 10%. Also, the error of viscosity predictions is consistently higher for more viscous fluids. Force fields used for viscosity calculation are APPLE&P, AMBER, OPLS, and CL&P. A comparison of predictions for [P2,2,2,5][Tf_2N] showed that the most accurate was APPLE&P, although this force field has been used less frequently than the others because APPLE&P force field parameters have only been developed for a small number of anions and cations.

Simulations showed that viscosity decreases with increasing temperature and the trend was explained by cation-anion RDFs and SDFs, where the height of the first peak decreased with increasing temperature, indicating weaker interactions between anion-cation. Unlike density, increasing cation chain length was generally found to increase viscosity for the same anion. This was explained by RDFs that showed stronger interactions between cation and anion, i.e., higher first RDF peak, albeit at a further distance. In terms of the effect of anion, there is some evidence that viscosity was affected by anion size. However, anion shape was also shown to be important; spherical anions were able to get closer to the cation, leading to higher viscosity, while the opposite was observed for angular shapes.

Self-diffusivity has been calculated from many simulations, primarily as a means of understanding trends in transport properties. This property is not readily measured experimentally, so accuracy cannot typically be evaluated. However, for [P2,2,2,2O1][Tf_2N], the AMBER force field was shown to over-predict self-diffusivity for both cation and anion. Generally, the self-diffusion coefficient has been reported to be higher for anions than cations and the trend was attributed to the small occupied volume of the anions which enabled them to move more easily. For cations, self-diffusion coefficient was smaller for longer alkyl chains, opposite the trend of viscosity, as expected since these two properties

are inversely related. There was no consistent trend observed for the anions. Lastly, it was shown that the self-diffusion coefficient usually increased in the presence of water because water molecules decrease counterion association such that ions can diffuse more freely.

Ionic conductivity has been calculated from a few simulation studies. Ionic conductivity was reported to increase with increasing temperature and decrease with increasing cation alkyl chain length, consistent with the trend for self-diffusion coefficient and opposite to that of viscosity. No consistent trend was observed for the anions. It has been suggested that higher ionic conductivity trends may be due to weaker hydrogen bonding.

Simulations have also been used to study heat capacity of selected phosphonium ILs using AMBER force fields. Some comparisons to experimental data have been performed and showed that the error ranges from 1% to tens of percent, depending on the IL. Although the relatively few number of studies performed precludes confirmation of trends, comparison of reported results suggested that heat capacities are higher for cations with longer alkyl chain lengths, consistent with the trend in viscosity. Lastly, it was shown that adsorption of CO_2 increases heat capacity.

The solubility of ILs and water has also been studied and found to depend on both the cation and anion. Smaller anions were more soluble in water than cations, with larger cations being the least soluble. Chemical reaction with CO_2 has been found to increase the water solubility of ILs. Interactions between water and ILs was primarily analyzed in terms of hydrogen bonding and the competition between hydrogen bond interactions, electrostatic interactions between the polar segments of the anions, and dispersion interactions between the hydrophobic alkyl chains in the cations.

Thermal degradation occurs through bond dissociation and so can be studied only using reactive force field. The availability of only one reactive force field has therefore limited such studies. However, a recent study [5] compared the thermal stability of phosphonium ILs with three different cations and two different anions. It was reported that size and branching on the cation had little effect on thermal decomposition temperature but that even subtle chemical differences between anions could affect decomposition reaction pathways and therefore the thermal stability.

Lastly, a few studies have used models of ILs confined between solid walls to explore confined fluid behavior. The limited examples of that involved phosphonium ILs showed that the ions exhibit ordering near the walls and this ordering is affected by the porosity and charge of the solids.

1.5 Research Opportunities for Phosphonium ILs

Although there have been previous MD simulation studies focusing on phosphonium ILs, there are still many opportunities for future research in this area.

First, as mentioned in the context of multiple properties of phosphonium ILs, the effect of the anion is neither well characterized nor understood. Attempts to identify trends primarily focused on anion size, based on the observation that cation size effects are typically monotonic. However, the same trends are not always observed. Some studies suggested anion shape is likely to be important, but it is likely that multiple factors contribute to the effect of the anion on a given property. As seen in the reactive simulation study of thermal decomposition [5], even minor differences in the chemical nature of the anion can affect behavior of phosphonium ILs. Since anion chemistry and structure can be varied systematically in a simulation, this is a suitable tool for understanding the important role of the anion.

Thermal conductivity, the ability of a material to conduct heat, is very important for phosphonium IL lubricants because it determines how efficiently they can dissipate heat generated by the shearing of moving mechanical parts. Like viscosity, thermal conductivity of liquids can be calculated using EMD simulations with the GK method and NEMD simulations [172, 173]. EMD methods of calculating thermal conductivity have been applied to characterize ionic compounds like NaCl, MgO, Mg_2SiO_4 [174] and molten alkali fluorides [175]. However, these methods have not yet been applied to phosphonium ILs.

Beyond the properties of the ILs themselves, the effectiveness of lubricants will depend on their response to interactions and confinement with solid materials. Studies of non-phosphonium ILs confined between solid wall have already shown this is a rich area of research. For example, differences in tribological behavior were reported for fatty acid ILs between steel-steel, steel-aluminum, steel-bronze, and steel-tungsten carbide [176]. Studies of ammonium and imidazolium ILs confined between various materials have shown that friction is affected by surface polarity, roughness, and charge because these factors affected the orientation and order of the ions [165–169, 177, 178]. Future MD simulations could use similar methods to model phosphonium ILs with solid materials to explore interactions between the ILs and surfaces, and the corresponding tribological behavior.

1.6 Research Objectives

As identified through the literature review in this chapter, there are still many opportunities for investigating phosphonium ILs and there is a significant potential for MD simulations to play an important role in the development of phosphonium ILs as environmentally benign lubricants and additives. The properties and behavior of these ILs depend on their chemical composition, i.e., cation and anion combination, and the operating conditions. To enable design and manufacture of high-performance biodegradable lubricants from phosphonium ILs, it is necessary to understand the relationship between ILs structure and their mechanical behavior. Toward this goal, we will use MD simulations to study the molecular scale mechanisms underlying the mechanical response of phosphonium ILs with different cation and anion combination under different operating conditions. The research in this dissertation mainly focused on select bulk fluid properties, wetting behavior, viscous friction, and corrosion behavior of phosphonium ILs.

In Chapter 2, MD simulation results for bulk property prediction are discussed. Here the non-reactive OPLS-AA force field is used to predict density, viscosity, and thermal conductivity. The accuracy of the modeling approach is evaluated by comparing to experiment/literature data. In particular, the effect of anions on these bulk properties is analyzed. In Chapter 3, the wetting behavior of phosphonium ILs on iron is studied for different cation-anion pairs to investigate the interaction of phosphonium ILs with solid surfaces. In Chapter 4, the viscous friction of 22 phosphonium ILs (11 cations paired with 2 anions) is calculated using non-equilibrium MD simulation approach. A predictive model of viscous friction is established that captures the effects of cation chain length, chain symmetry, and operating shear rates. In Chapter 5, reactive molecular dynamics simulations are used to explore the mechanisms underlying corrosion of ferrous surfaces by trihexyltetradecylphosphonium benzoate and trihexyltetradecylphosphonium salicylate. Lastly, in Chapter 6, a summary of the research, the impact of the results, and future work is provided.

Chapter 2

Bulk Property Prediction

2.1 Introduction

As mentioned in Section 1.4, density and viscosity are the two most commonly reported liquid properties for phosphonium ILs from MD simulations because these two properties play a fundamental role in how a lubricant functions and how machines perform. Thermal conductivity is another important property for lubricants because it determines how efficiently they can dissipate heat generated by the shearing of moving mechanical parts. However, no previous MD simulation study was carried to predict thermal conductivity for phosphonium ILs. For the phosphonium cation, we mainly focused on [P6,6,6,14] since it has been widely studied in previous experiment works and exhibited low wear and friction [29, 42, 179–181]. Therefore, density, viscosity, and thermal conductivity were studied for ILs with [P6,6,6,14] cation paired with three biodegradable anions [Benz], [Sali], and [Sacc]. Snapshots of the individual ions are shown in Fig 2.1.

2.2 Molecular Dynamics Simulation

As described in Section 1.4, when parameter sets are available, OPLS-AA force field has higher accuracy for predicting density. Therefore, OPLS-AA force field was used in current study for predicting bulk properties, wetting behavior and tribological behavior. OPLS-AA force field parameters were obtained from LigParGen [182].

The MD simulations in this study were carried out using an open source MD simulation

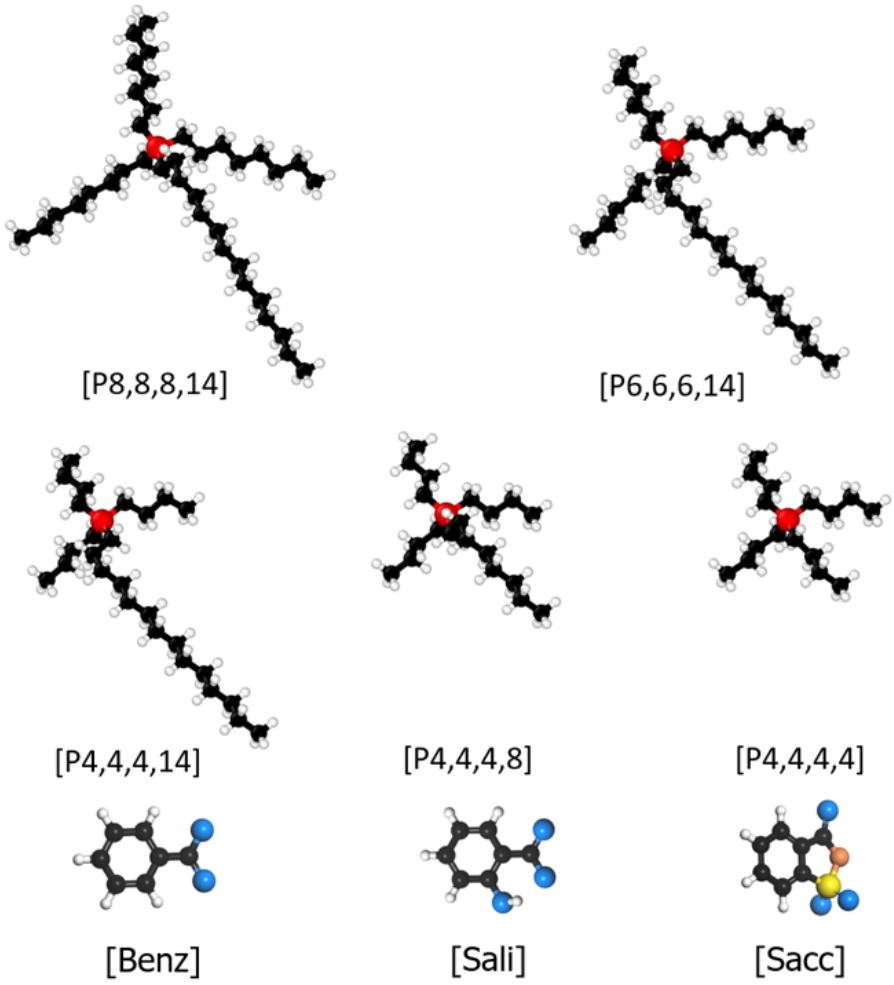

Figure 2.1: Snapshots of the molecular models of the five cations and three anions used in the simulations of phosphonium ILs. Sphere colors correspond to atoms type: white H, black C, red P, blue O, orange N, green F, and yellow S.

package LAMMPS (Large-scale Atomic/Molecular Massively Parallel Simulator) [183]. OVITO was used for model visualization [184]. For bulk properties prediction, the time step was 1.0 fs for MD simulations with non-reactive force fields. The Nosé–Hoover thermostat [185] and barostat [186] were used to control the temperature of the system with damping parameters of 100× and 1000× the time step, respectively. The velocity-Verlet algorithm [187] was applied to solve the equations of motion. The cutoff distance for Lennard-Jones and electrostatic interactions was 12 Å for non-reactive force fields. In all simulations, energy minimization was performed first using the conjugate gradient algorithm until reaching a stopping tolerance of 1.0×10^{-6} for energy and 1.0×10^{-8} for force.

2.3 Density

For density prediction, after energy minimization, simulations were run in the canonical (NVT: constant number of atoms N, volume V, and temperature T) ensemble to decorrelate the positions and velocities of the atoms [188] for 0.1-1 ns. Then, the system was equilibrated with an isothermal–isobaric (NPT: constant number of atoms N, pressure P, and temperature T) ensemble until steady potential energy was reached for 1-5 ns. The details of how density is calculated in MD simulations was mentioned previously in Section 1.4.

The comparison of density calculated from simulations and experimental measurements (data from P. Menezes and H. Rahman at University of Nevada, Reno) for the three phosphonium ILs at temperatures from 25 - 100°C are shown in Fig. 2.2. It is observed that density increases as [Benz] < [Sali] < [Sacc] in both experiment and simulation. For the effect of temperature, density decreased with increasing temperature for all three ILs. For the difference between simulation and experiments, the simulated density of [Sacc] is slightly larger than experiment measurements, while simulated density of [Benz] and [Sali] are slightly lower than experiment measurements. However, the relative error between simulation and experiment Was around 1-2% for all three ILs, indicating that OPLS-AA force field is capable of modelling the static properties of the phosphonium ILs studied with reasonable accuracy.

The structures of the three anions are similar, so the difference in their densities can be analyzed in terms of the molecule mass/volume ratio [189]. Based on this method, mass/volume ratio increases as H < C < N < O < S within the anions. Since the maximum mass/volume ratio for [Benz] and [Sali] is from O atoms, the density of [Sali], with addi-

tional O atoms, is larger than [Benz]. Similarly, [Sacc] has more N, O, and S atoms than the other two anions, leading to the highest density.

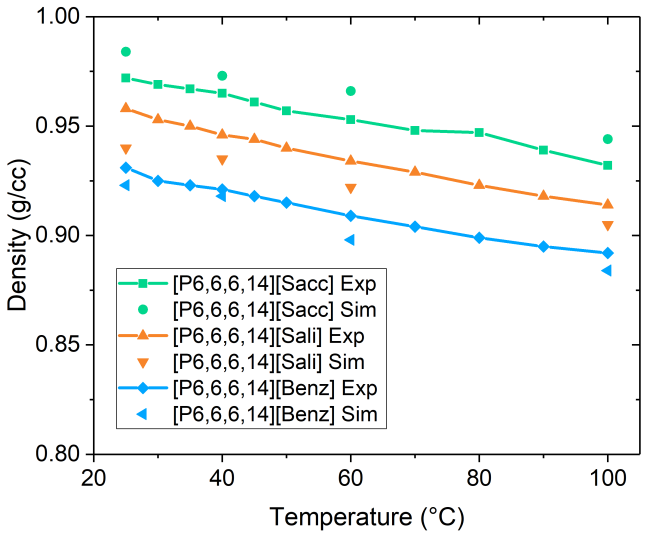

Figure 2.2: Comparison of density between simulation and experiment (data from P. Menezes and H. Rahman at University of Nevada, Reno).

2.4 Viscosity

To calculate viscosity, the Green–Kubo approach, which relates the viscosity to the time integral of the stress autocorrelation function [190], was used. Following the equilibration process, after system density and potential energy reached steady state, further equilibrium molecular dynamics simulations were carried out with 2 ns in the NPT ensemble followed by NVE ensemble production runs. Here, the pressure tensor components were saved every 5 fs for 5 ns at 100°C and 20 ns at 40°C during the NVE simulations. An average low-shear viscosity and its standard deviation values were calculated from 10 NVE trajectories and by applying the Green–Kubo formalism following the time decomposition approach [191].

The comparison of viscosity calculated from simulations and experiment measurements (Data from P. Menezes and H. Rahman at University of Nevada, Reno) is shown in Fig. 2.3. Like density, viscosity also decreased with increasing temperature for all three ILs. For the accuracy of EMD simulations using Green-Kubo method, the relative error between simu-

lation and experiment is around 10-20% for temperature at 40°C, while the error increases to 30-40% for temperature at 100°C.

Comparing the three ILs, it is observed that viscosity increases as [Sali] < [Benz] < [Sacc] for both experiment and simulation. It has been reported that viscosity increases with hydrogen bonds for ILs with similar structure [69, 130], which may explain the trend observed here. [Sacc] has four hydrogen bond acceptors while [Sali] and [Benz] have three and two [192], respectively. Therefore, [Sacc] has stronger interaction with cations, resulting in overall lower ion mobility and higher viscosity. Although [Sali] has more hydrogen bond acceptors than [Benz], it has a rotatable bond [192] that could allow additional internal rotation of [Sali], leading to relatively lower viscosity.

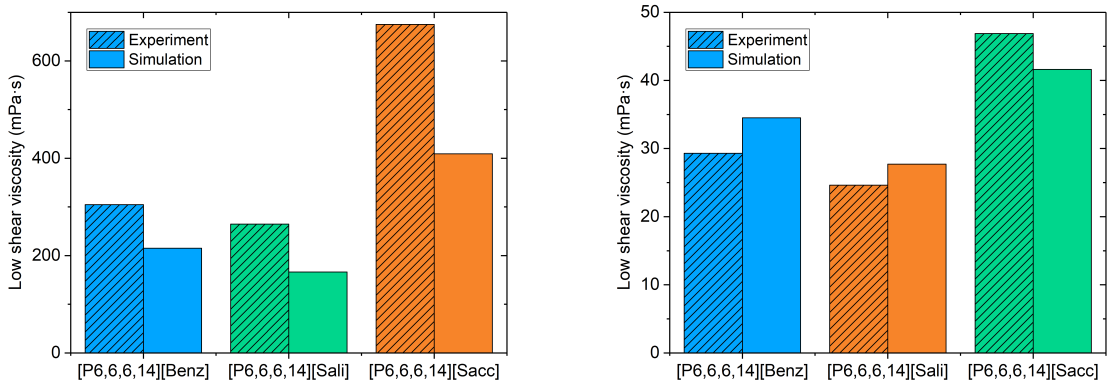

Figure 2.3: Comparison of viscosity between simulation and experiment under (a) 40°C and (b) 100°C.

2.5 Thermal conductivity

Similar to the viscosity simulation, after steady-state was reached, further equilibrium molecular dynamics simulations using Green-Kubo method were carried out to predict thermal conductivity at 40°C and 100°C. In contrast to viscosity that is related to the autocorrelation of stress, thermal conductivity is related to the autocorrelation of heat flux [190].

Since there is no available experimental data for thermal conductivity for the three phosphonoum ILs, the simulated thermal conductivity was compared with [P6,6,6,14] car-

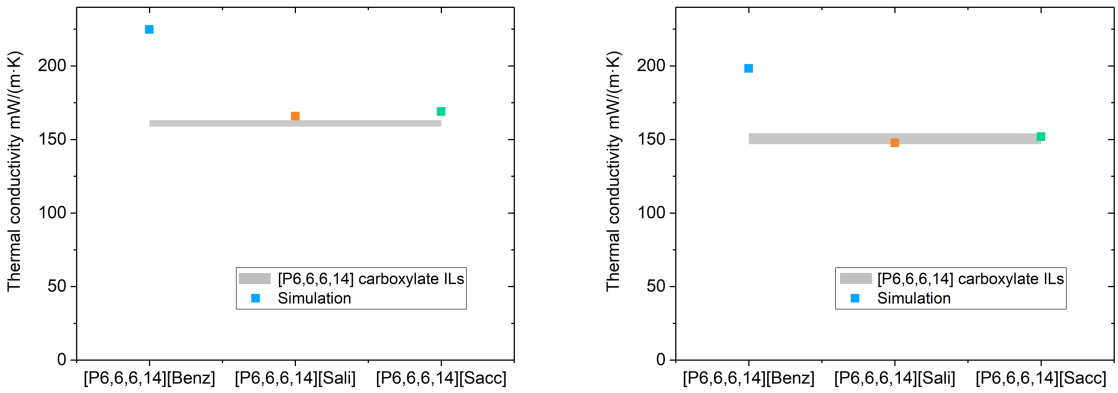

Figure 2.4: Comparison of simulated thermal conductivity three phosphonoum ILs with [P6,6,6,14] carboxylate ILs from a previous study [7] under (a) 40°C and (b) 100°C.

boxylate ILs from a previous study [7], as shown in Fig. 2.4. For the effect of temperature, thermal conductivity decreased with increasing temperature for all three ILs.

It is observed that thermal conductivity increases as [Sali] < [Sacc] < [Benz] from MD simulations with [Sali] and [Sacc] having thermal conductivity close to [P6,6,6,14] carboxylate ILs, while the value of for [Benz] is much larger. It has been reported that anions with larger molar mass is related to lower thermal conductivity with similar structure [7]. This could be the reason that [Benz] has higher thermal conductivity than [Sali]. However, atom types and molecule structure of [Sacc] are not the same to the other two anions. Therefore, more analysis, like cation-anion Coulombic interactions, hydrogen bonding, and van der Waals interactions should also take into account, as suggested in previous work [193], although this is outside the scope of the current study.

2.6 Conclusions

In general, MD simulations with the non-reactive OPLS-AA force field can accurately predicted density and thermal conductivity across a wide range of temperatures, and viscosity at high temperature when using EMD-GK for phosphonium ILs. This provided confidence for using this force field to investigate the wetting behavior in Chap 3 and frictional behavior in Chap 4 for phosphonium ILs.

Chapter 3

Wetting Behavior of Phosphonium ILs

3.1 Introduction

In many applications, phosphonium ILs are in contact with a solid surface and form a solid-liquid interface. Therefore, the adsorption and spreading of phosphonium ILs on solid surfaces, i.e., wettability, plays an important role in their performance [194–196]. Wettability is controlled by the balance between the intermolecular adhesion (liquid-solid) and cohesion (liquid-liquid) interactions [197]. For phosphonium ILs used as lubricants, wettability is important because it affects the fluid's ability to spread and protect solid surfaces [195, 198]. Wetting is also important for phosphonium ILs used as electrolytes since the utilization rate of electrode surface area and energy density of supercapacitors can be improved by increasing wettability [199].

Usually, wettability is quantified as the contact angle between a liquid droplet and a solid surface [200]. Strong adhesion to the substrate surface and weak cohesion within the liquid lead to a high degree of wetting with low contact angles, while a combination of weak adhesion and strong cohesion results in high contact angles and poor wetting. When a droplet is placed on a surface, there is initially transient evolution of contact angle as the liquid droplet is wetting the surface and then the contact angle reaches steady state. Both the transient and steady-state contact angles are used to characterize wetting behavior. Usually, a steady-state contact angle less than 90 $^{\circ}$ indicates good wettability [201]. Wetting time, the time required for the contact angle to reach steady state, can be used to determine the relative strengths of adhesion and cohesion. Longer wetting times indicate adhesion dom-

ination, whereas shorter wetting times indicate the dominance of cohesion [202]. These properties can be measured experimentally using a goniometer as well as with molecular dynamics (MD) simulations that give an atomistic view of contact angle mechanisms.

Experimental studies have reported the contact angle of neat phosphonium ILs measured on a variety of surfaces and at a range of temperatures. All reported good wettability with contact angles less than 90° [194, 195, 202–206]. Some studies have compared contact angles on different substrates and shown that wettability is better on materials with high surface free energy, i.e, lower contact angle on steel than PTFE [204] and lower contact angle on TiN than steel, CrN, and ZrN [195]. Temperature has also been shown to affect contact angle. However, while the contact angle of some ILs decreases with increasing temperature [194], other ILs exhibit the opposite trend [202].

Lastly, the wettability of phosphonium ILs in solution has also been measured experimentally and it has been reported that contact angles of IL solutions could be smaller or larger than those of the neat ILs, depending on the solvent and substrate material [207, 208].

MD simulations have been used to complement experiments by exploring the atomistic origins of IL wettability [170, 209–213]. However, currently there are few simulation studies focused on the wettability of phosphonium ILs. Simulations showed that the steady state contact angle of [P4,4,4,4][Cpy] on silanol and silane surfaces was less than 90°, indicating a strong liquid-surface interaction, but the contact angle was slightly larger on the silane surface [214]. The steady-state contact angle of [P2,2,2,5][Tf_2N] nanodroplets on platinum surfaces at 298 K was calculated in simulations. The results showed that the contact angle on Pt(100) was higher than on Pt(111), demonstrating that the crystallographic nature of the surface can affect spreading. The simulations also compared two different ILs and found that the contact angle of [P2,2,2,5][Tf_2N] nanodroplets was lower than that of its ammonium counterpart [N2,2,2,5][Tf_2N] on both Pt surfaces [170].

IL properties, including wettability, are significantly affected by the chemistry and structure of the cation and anion combination [20, 215]. No previous studies of phosphonium ILs focused on the effect of the cation. However, some studies that characterized the effect of cation for other ILs and reported that longer alkyl chains corresponding to lower contact angle. For example, the contact angle of [TF_2N] anion-based ILs with different cations was experimentally found to be lower for longer alkyl chain with contact angle increasing as [$C_{10}C_1$im] < [C_4C_1im] < [C_2C_1im] [210]. This trend was consistent with simulation results that showed radial distribution function (RDF) peaks were

sharper and higher for longer chains, indicating better ordering near the surface [210]. In another simulation study, the contact angle of [BF_4]-based ILs on graphite surface was lower for [PrMIM] cation with a longer alkyl chain compared to [BF_4] cation with a shorter alkyl chain. The interaction energy between graphite and [PrMIM][BF_4] was found to be higher than that for [DMIM][BF_4] which implied that the longer [PrMIM] cations had a stronger affinity towards the graphite surface, leading to a lower contact angle [211]. Lastly, simulations showed that contact angles of ILs with [BMIM] with long alkyl chains were lower than [EMIM] ILs with short chains for anions including [Cl], [Br], [BF_4], [PF_6], and [TF_2N] on bismuth telluride surfaces [213].

For the effect of anion, it was reported that, for [P6,6,6,14] cations, contact angle increased as [p-TsO] $<$ [Tf_2N] $<$ [Cl] $<$ [DCA] $<$ [BF_4] on PTFE surfaces. The lower contact angle of [p-TsO] was attributed to the planarity and electron density of the aromatic ring [205]. An experimental study reported that contact angle increased as [BEHP] $<$ [$(iC8)_2PO_2$] $<$ [Cl] $<$ [DCA] on AISI 52100 steel, CrN, and ZrN surface for the same [P6,6,6,14] cation. This trend was attributed to the inverse relationship between anion size and surface tension [195]. The effect of anion size was also observed in simulations of non-phosphonium ILs that showed larger anions had better wetting on bismuth telluride surfaces and the contact angle decreased as [Cl] $>$ [Br] $>$ [BF_4] $>$ [PF_6] $>$ [TF_2N] for imidazolium-based ([BMIM] and [EMIM]) ionic liquids. This trend was attributed to higher cohesion energy for the larger anions [213].

Studies so far have shown that cation and anion can affect contact angle, but there has been no systematic study of these effects for phosphonium ILs nor the underlying mechanisms. To understand this effect, here we explored the relationship between phosphonium cation-anion pairs and contact angle. In particular, the effect of different anions (especially with similar chemistries) on contact angle for the same cation and the effect of alkyl chain length in tetra-alkyl-phosphonium cations on contact angle for the same anion were studied. The origins of observed cation and anion trends were explored in terms of the strength of the adhesion and cohesion interactions.

3.2 Molecular Dynamics Simulation

For wetting behavior, after energy minimization, the IL was partially relaxed as the temperature was increased from 1 K to 298 K over 1 ns in a NVT ensemble. This relaxation

procedure ensured the cohesion in the ionic liquid and droplet formation. During this relaxation stage, the cube IL droplet became a more physically realistic spherical cap shape. Then, the simulation was run at temperature of 298 K for another 10 ns to allow the contact angle to reach steady state.

First, the wettability of three ionic liquids with benzoate [Benz], salicylate [Sali], and saccharinate [Sacc] anions paired with [P6,6,6,14] cation on a model iron surface was calculated by MD simulations. This is validated by comparing experimental measurements on 52100 stainless steel as shown in Appendix [**?**]. Since the alkyl chain length in cations affect contact angle, then simulations were extended beyond the IL systems studied experimentally to include five different cations [P4,4,4,4], [P4,4,4,8], [P4,4,4,14], [P6,6,6,14], and [P8,8,8,14] in combination with three anions [Benz], [Sali], and [Sacc]. The phosphonium ILs models were initially constructed using BIOVIA Materials Studio [216]. For iron substrates, body-centered cubic crystal structures Fe(1,1,1) were obtained from Materials Project [217].

The interatomic interactions within and between the ILs were described by the OPLS-AA Force field [66] based on LigParGen [182]. Interactions with the iron substrate were modeled using the Lennard-Jones (LJ) potential with ε_{ss} = 0.2007 eV and σ_{ss} = 2.4193 Å [218]. Interactions between substrate and ILs were modeled using the LJ potential, combining the Fe parameters with the LJ parameters of OPLS-AA using geometric mixing rules [219].

It has been found that contact angle generally increases linearly with droplet size until it converges to a constant values after a critical number of ions or droplet radius is reached [220, 221]. In previous simulations, the contact angle was found to converge for [BMIM][BF_4] on graphene with at least 100 ion pairs [221] or an initial cubic box size of 50 Å [211] and for [EMIM][BF_4] on silicon with a droplet radius of at least 20 Å [222]. Based on these, all model phosphonium IL systems here were created using PACKMOL [223] with at least 100 ion pairs, corresponding to the liquid in a 50 Å cubic volume. The IL cube was placed 10 Å above iron surface as shown in Fig 3.1(a). All MD simulations were performed using the open-source Large Atomic/Molecular Massively Parallel Simulation (LAMMPS) package [183] with a timestep of 1 fs.

First, energy minimization was performed using the conjugate gradient algorithm until reaching a stopping tolerance of 1.0×10^{-6} for energy and 1.0×10^{-8} for force. After energy minimization, the IL was partially relaxed as the temperature was increased from 1 K

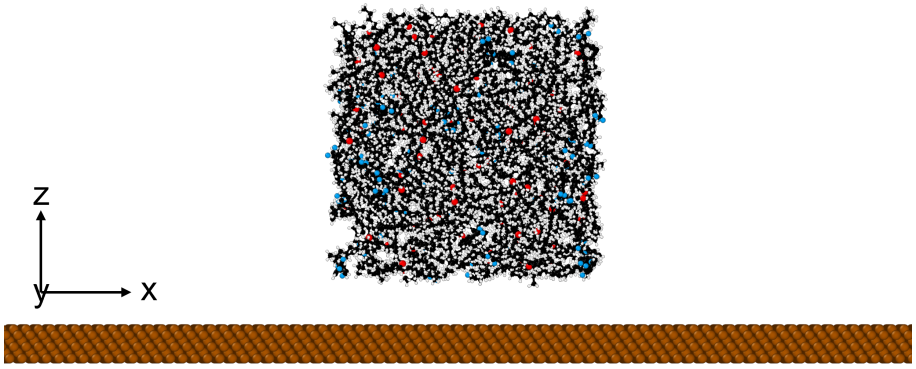

(a)

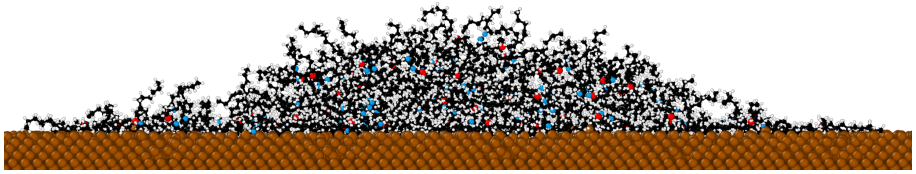

(b)

Figure 3.1: Side view snapshots of (a) the initial simulation ensemble and (b) the simulation after 10 ns relaxation for [P6,6,6,14][Benz]. Note that only part of the 250 $\times$ 250 Å substrate is shown here.

to 298 K over 1 ns in a canonical ensemble (NVT). The Nosé–Hoover thermostat [185] was used to control the temperature of the system and the velocity-Verlet algorithm [187] was applied to solve the equations of motion. This relaxation procedure ensured the cohesion in the ionic liquid and droplet formation. During this relaxation stage, the cube IL droplet became a more physically realistic spherical cap shape. Then, the simulation was run at temperature of 298 K for another 10 ns to allow the contact angle to reach steady state. The configuration of simulation ensemble after 10 ns relaxation is shown in Fig 3.1(b). Each simulation was run three times from the same atomic configuration with different initial velocity distributions.

In previous simulation studies [170, 213, 214], the contact angle was determined using a simple two-dimension method as the angle between the horizontal line at the liquid-solid

interface and the line tangent to the droplet surface at the liquid-solid-valor three phase contact point. This calculation has also been performed using more complicated three-dimensional algorithms [222, 224, 225]. However, the tangent line is difficult to define for the relatively large and branched ions here. Therefore, the contact angle was determined by the equation $\theta = 2(tan^{-1}(h/r))$, where r is the radius of the liquid-solid contact circle fit to the positions of the outermost IL atoms in the XY plane and the h is the height of the apex [209, 226]. The radius of the liquid-solid contact circle was averaged over eight different radial directions at each time. After the potential energy reached steady state, the contact angle was calculated by averaging 20 trajectories (time steps) during the last 1 ns of the simulation. To explain the contact angle trends, the average adhesive and cohesive energies were calculated as the sum of the pairwise interactions between the atoms in the ILs and surface or between atoms in different ILs, respectively, during the last 1 ns of the simulation. A negative adhesive or cohesive energy correspond to net attraction.

3.3 Comparison of Simulations and Experiments

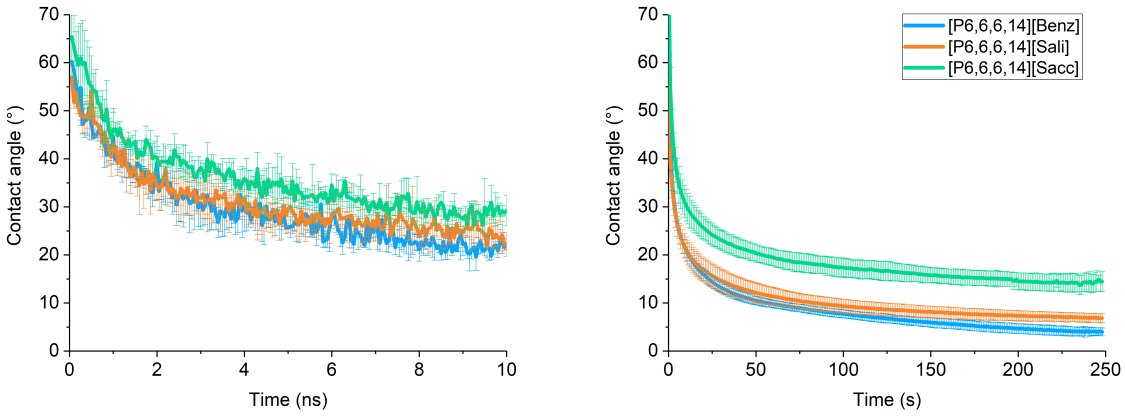

(a) **(b)**

Figure 3.2: Contact angle as a function of time for [P6,6,6,14][Benz], [P6,6,6,14][Sacc], and [P6,6,6,14][Sali] from (a) simulation calculations on Fe (111) surface with error bars reflecting the standard deviation across three independent MD simulations; and (b) experimental measurements on polished AISI 52100 steel surface with error bars reflecting the standard deviation across four independent measurements (Data from P. Menezes and H. Rahman at University of Nevada, Reno).

MD simulations were carried out for ILs comprised [P6,6,6,14] with three different anions. As shown in Fig. 3.2(a), the contact angle of all the three [P6,6,6,14]-based ILs gradually decreased during the 10 ns simulation. The average contact angles over the last 1 ns of the simulation for [P6,6,6,14][Sacc], [P6,6,6,14][Sali], and [P6,6,6,14][Benz] were 21.5º, 24.5º, and 28.7º, respectively.

Experimental measurements were carried out (by P. Menezes and H. Rahman at University of Nevada, Reno) for the same three [P6,6,6,14]-based ILs. As shown in Fig. 3.2(b), the contact angle of all three ILs decreased rapidly to approach a steady-state value. At steady state, the contact angles of [P6,6,6,14][Sacc], [P6,6,6,14][Sali], and [P6,6,6,14][Benz] were 14.2º, 6.89º, and 4.10º, respectively. The small contact angles measured here are consistent with previous studies of [P6,6,6,14][Tf_2N] ILs on stainless steel surface [202, 206], which also reported contact angles less than 20º.

Although both simulation and experiment indicate that all three phosphonium ILs have a good wettability on stainless steel, the magnitudes of the simulation contact angles are larger than those in experiment. This is mainly due to the limited size and timescales of the simulations. However, in both simulation and experiment, [P6,6,6,14][Sacc] had the largest steady-state contact angle and [P6,6,6,14][Benz] had the smallest. These results indicate that the anion can affect contact angle, as observed in previous studies [194, 202–204, 206, 227].

As mentioned previously, both the cation and anion can affect contact angle. The simulations were used to explore these effects further by comparing the contact angle for ILs with the three anions analyzed above and five different cations. Based on the expectation that contact angle is determined by the relative strengths of cohesion and adhesion, the contact angle trends were analyzed in terms of adhesive and cohesive energies in the simulations.

3.4 Effect of Cations

The steady-state contact angle is plotted with respect to cation in Fig 3.3. It is observed that steady-state contact angles decreased with increasing alkyl chain length for all three anions. This trend was also reported in previous studies for imidazolium cations [210, 211, 213]. Another observation in Fig 3.3 is that contact angle decreased with increasing cation size, regardless of whether the size increase was in one chain (compare [P4,4,4,4], [P4,4,4,8],

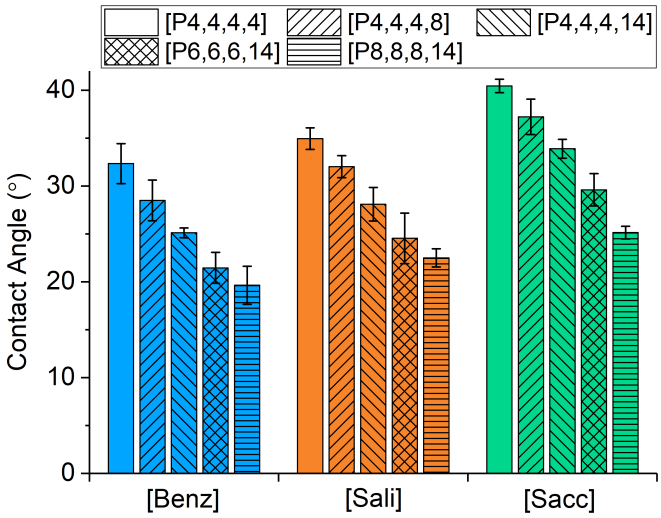

Figure 3.3: Comparison of the steady state contact angle for cations with different alkyl chain lengths paired with three different anions. Error bars reflect standard deviation among three independent MD simulations.

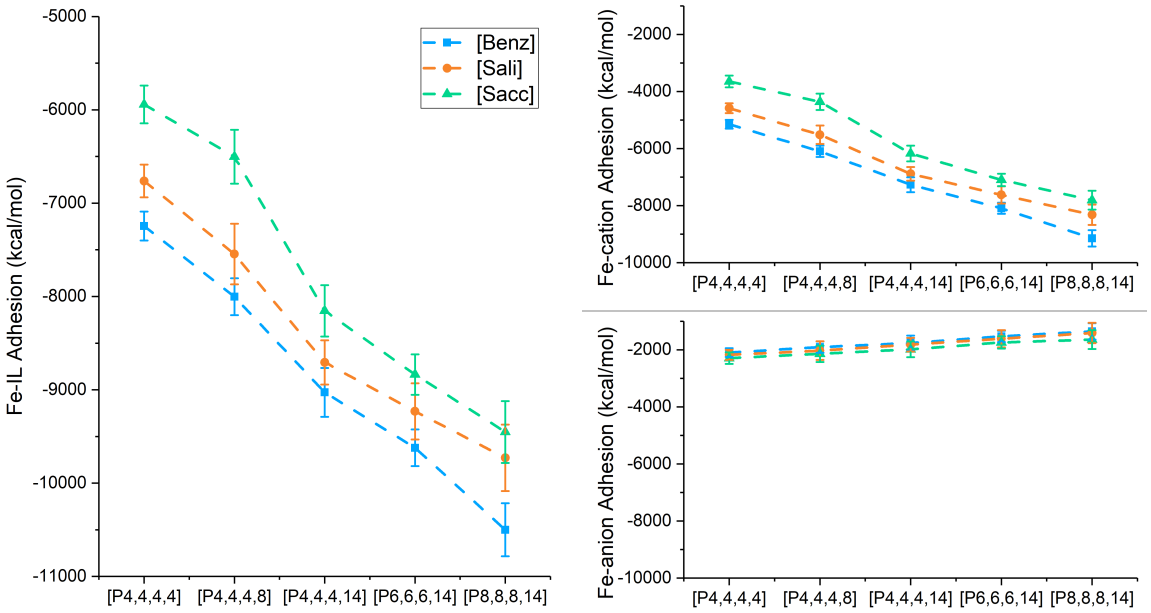

(a) **(b)**

Figure 3.4: Adhesive interaction energy between the surface and the ILs, and (b) separated into the cation (top) and anion (bottom) contributions, plotted as functions of increasing alkyl chain length for the three anions.

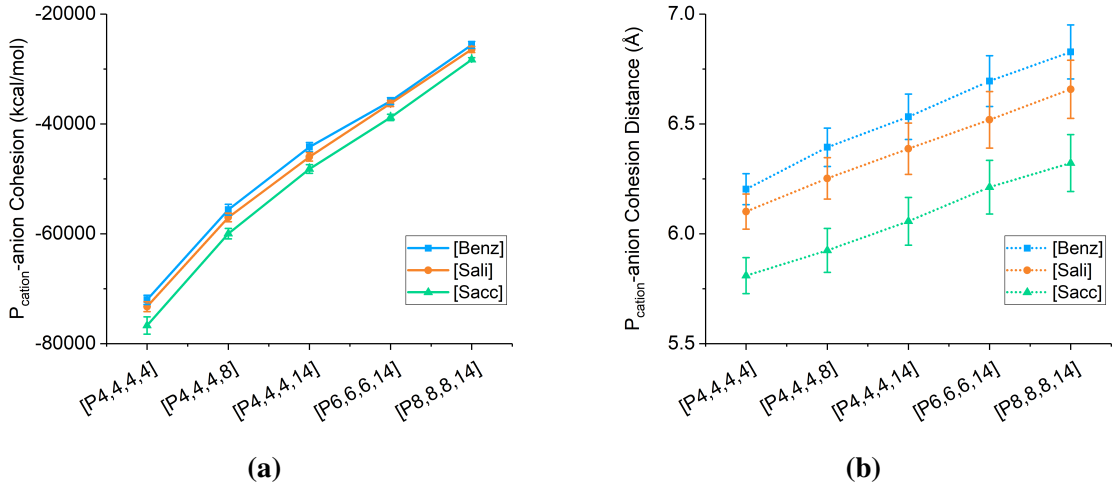

Figure 3.5: (a) Cohesive energy between P atoms in the cations and all atoms in the anions, and (b) average distance between cation P atoms and anions, plotted as functions of increasing alkyl chain length for the three anions.

and [P4,4,4,14]) or multiple chains ([P4,4,4,14], [P6,6,6,14], and [P8,8,8,14]). The overall trend may be due to the longer chains increasing adhesion or decreasing cohesion, or both.

The total Fe-IL adhesion energy, reported in Fig. 3.4(a), increased (became more negative) with increasing cation chain length, consistent with the trend of decreasing contact angle. The adhesive force was separated into contributions from the cation and anion, as shown in Fig. 3.4(b). The Fe-cation energy increased with chain length while the Fe-anion energy decreased with chain length. However, the magnitude of the cation adhesion was much larger than that for the anion, so the cation trend dominated the overall adhesion with the surface. The Fe-cation interaction energy was further broken down by atom type and it was found that the C atoms contribute most to the total adhesion. Therefore, the increasing adhesive energy trend can be attributed to the fact that there are more C atoms present in the longer chains.

The cohesion between ions was also analyzed. It was found that the only attractive inter-ionic interactions were between the P atoms in the cation and the atoms in the anions. The cohesive energy between the cation P atoms and anions, shown in Fig. 3.5a, decreased (becomes less negative) with increasing chain length. The trend could be due to the interference of the longer chains that separated the anion and cation, thereby decreasing cohesion. This hypothesis was confirmed by calculating the average distance between the

cation P atom and the atoms in the nearest anion. As shown in Fig. 3.5b, the cation-anion distance increased with alkyl chain length, consistent with the decreasing cohesive energy and the corresponding lower contact angle.

3.5 Effect of Anions

The steady-state contact angles are plotted with respect to anion in Fig. 3.6. For all five cations, the contact angle increased as [Benz] < [Sali] < [Sacc]. It has been proposed that larger anions will have lower contact angle [195]. Anions with aromatic rings like [p-TsO] have also been reported to have lower contact angle than anions without aromatic rings like [BF_4], [DCA], [Cl] and [Tf_2N] because of the planarity and delocalised electron density of the ring [205]. However, [Benz], [Sali], and [Sacc] are all aromatic ring-based anions with similar size, so the difference in their contact angles should be attributed to other mechanisms. First, the adhesion and cohesion were analyzed, following the approach used to explain the cation trends.

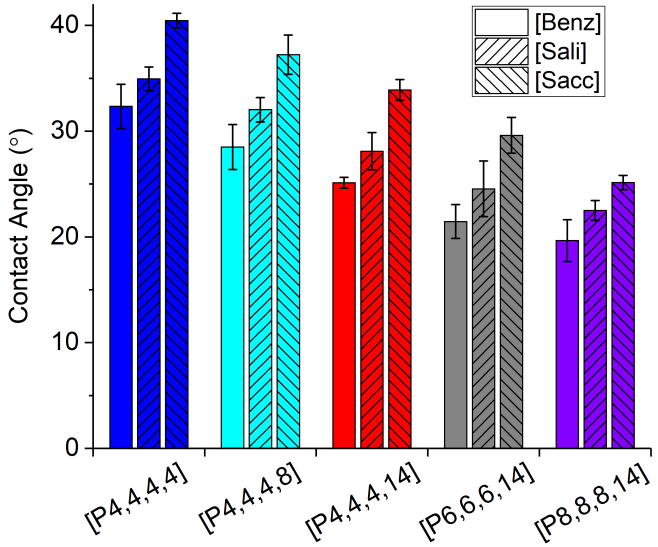

Figure 3.6: Comparison of the steady state contact angle for anions [Benz], [Sali], and [Sacc] paired with five different cations. Error bars reflect standard deviation among three independent MD simulations.

The total Fe-IL adhesion energy, plotted vs. anion in Fig. 3.7(a), was largest for [Benz] and smallest for [Sacc]. This trend is consistent with the observation that [Benz] has the

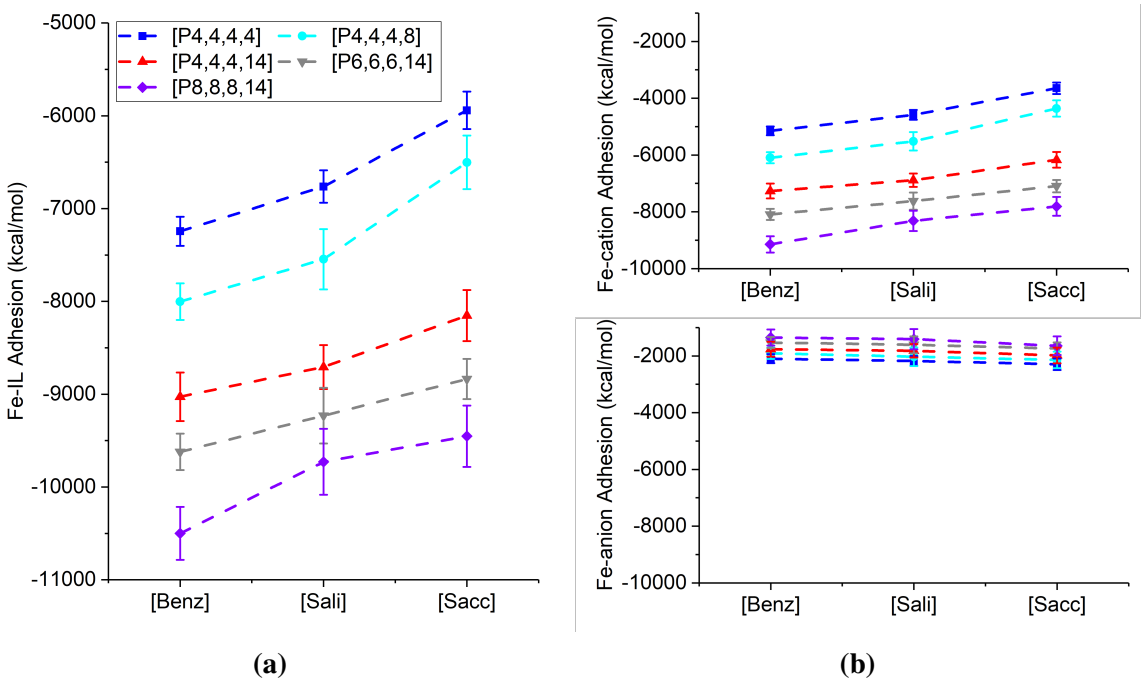

(a) **(b)**

Figure 3.7: Adhesive interaction energy between the surface and the ILs, and (b) separated into the cation (top) and anion (bottom) contributions, plotted vs. anion for the five cations.

lowest contact angle while [Sacc] has the largest contact angle. To explain how the anions affect total adhesion, the Fe-anion and Fe-cation adhesive energy were analyzed separately.

As shown in Fig. 3.7(b), Fe-anion adhesive energy increases as [Benz] $<$ [Sali] $<$ [Sacc]. This may be due to the fact that [Sacc] has the most atoms and, as shown in Fig 3.8, the biggest contribution to adhesion in [Sacc], the S atom, is not present in the other two anions. Similarly, for [Sali], there is one more O atom in the hydroxyl group than [Benz] which could contribute to the higher interaction energy observed for [Sali]. However, this difference in Fe-anion energy is very small compared to the difference between the anions in terms of Fe-cation adhesion. The Fe-cation adhesion is largest for [Benz] and smallest for [Sacc], consistent with the contact angles. Therefore, the anion contact angle trend can be attributed to the indirect effect of the anion on interactions between the cations and substrate.

Since the Fe-anion energy is not very different for the three anions, their effect on cation adhesion may be due to the orientation of the anions with respect to the surface [228, 229]. An orientation order parameter [209, 211, 212] was calculated from the relative directions

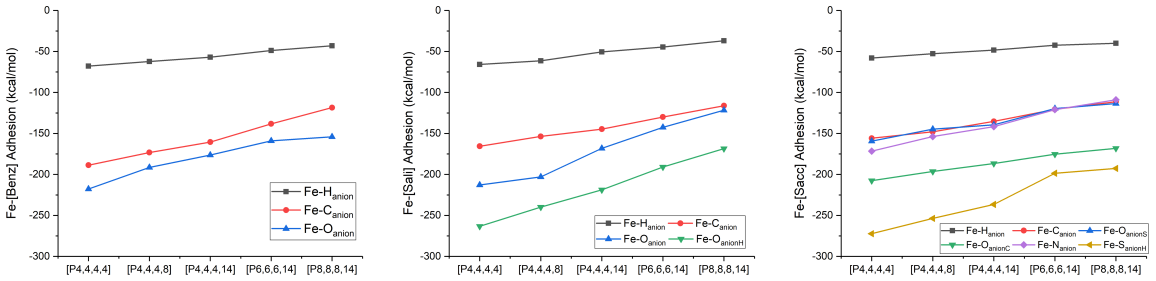

Figure 3.8: Adhesive interaction energy between Fe atoms in the substrate and each atom types in (a) [Benz], (b) [Sali], and (c) [Sacc] anions.

of the Fe surface-normal and the direction normal to the plane of the anion atoms, as illustrated in Fig 3.9. The value of orientation order parameter can vary from -0.5 when the anion ring is parallel to the surface to 1 when the anion ring is perpendicular to the surface. The distributions of the orientation order parameter for anions within 5 Å of the substrate (cutoff distance identified from the first peak of the anion position distribution functions were calculated from the last 1 ns of all three independent simulations for each anion. The results for the [P6,6,6,14] cation are shown in Fig. 3.10 with similar distributions observed for other cations. It can be seen that more of the [Benz] anions have an orientation order parameter near 1, meaning they are perpendicular to the surface, whereas the orientation order parameter for the [Sacc] anions is lower, indicating fewer are perpendicular. It has been reported that all three anions can orient perpendicular to metal surfaces [230–234], but the asymmetry of the [Sacc] anion causes it to tilt towards the surface [234]. The preferred perpendicular alignment of the [Benz] anions allows the cations more access to the surface, consistent with the stronger Fe-cation adhesion for the [Benz] ILs than the [Sacc] ILs in Fig. 3.7(b).

The cohesive energy between the cation P atoms and anions is plotted vs. anion in Fig. 3.11a. The results show that the cohesion was strongest for [Sacc] and weakest for [Benz] with any cation. This trend was explained by the average distance between the cation P atom and the atoms in the nearest anion, in Fig. 3.11b, that increased as [Sacc] $<$ [Sali] $<$ [Benz]. It was found there are more atoms in [Sacc] that have attractive interactions with the cation than the other two anions, and the extra O atom in [Sali] enables stronger cohesion than [Benz]. The cohesion energy and distance trends are consistent with the contact angle results.

$$OP = \frac{1}{2}(3\ cos^2\theta - 1)$$

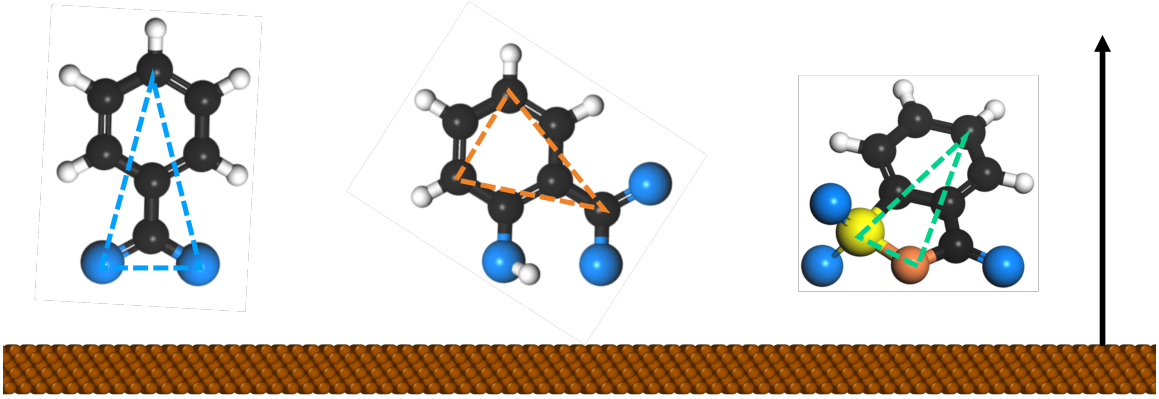

Figure 3.9: Illustration of the orientation order parameter calculation. θ is the angle between the normal vector perpendicular to the surface (black arrow) and the plane covering the aromatic ring represented by the triangle in each anion. When the anion is perpendicular to the surface, $\theta = 0°$ and the order parameter (OP) is 1.

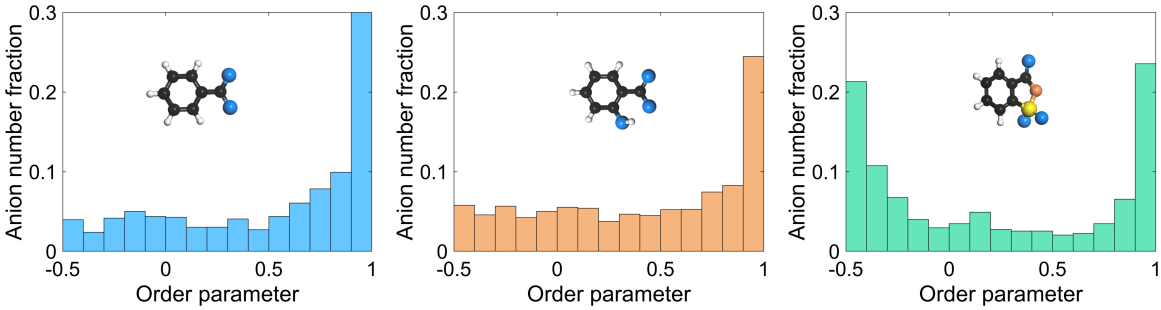

Figure 3.10: Orientation order parameter distribution for (a) [Benz], (b) [Sali], (c) [Sacc] paired with [P6,6,6,14] calculated from the last 1 ns of three independent simulations for each anion. The parameter ranges from -0.5 when the anion ring is parallel to the surface to 1 when the anion ring is perpendicular to the surface.

3.6 Conclusions

Overall, the wetting of phosphonium ILs with systematically varied cation and anion combinations on ferrous surfaces was evaluated. It was found that longer alkyl chains in the cations led to lower contact angle. This was explained by the effect of more C atoms that both increased adhesion with the substrate and separated the P atom in the cation from the

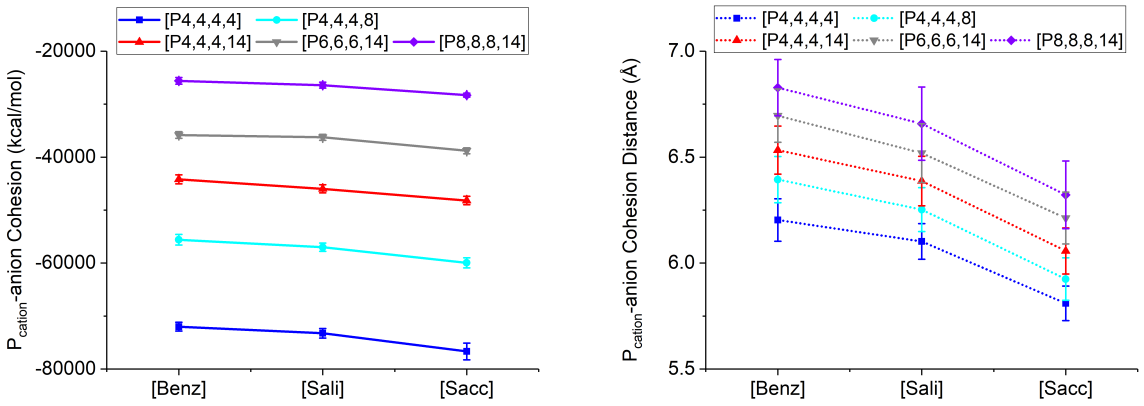

Figure 3.11: (a) Cohesive energy between P atoms in the cations and all atoms in the anions, and (b) average distance between cation P atoms and anions, plotted vs. anions for the five cations.

anion, thereby decreasing cohesion. For anions, the contact angle increased as [Benz] $<$ [Sali] $<$ [Sacc] when paired with the same cation. Like the cations, the anion contact angle trend was consistent with cohesion energy, and explained by the number and type of atoms in the anions that had attractive interactions with P atom in the cations. The adhesion energy was also consistent with the anion contact angle trend, but this case was explained by the orientation of the anions with respect to the surface. Specifically, perpendicular anion alignment allowed the cations more access to the surface, thereby increasing adhesion. The alignment trends were associated with asymmetry of the anion structures, where greater symmetry led to more perpendicular alignment, higher cation-Fe adhesion, and lower contact angle.

Chapter 4

Viscous Friction of Phosphonium ILs

4.1 Introduction

As mentioned in Section 1.5, beyond the properties of the ILs themselves, the effectiveness of lubricants will depend on their response to confinement and interactions with solid materials. Studies of non-phosphonium ILs confined between solid walls have already shown this is a rich area of research [165–169, 177, 178]. Therefore, it is important to investigate the frictional behavior of phosphonium ILs for their application as lubricants.

Frictional behavior follows the Stribeck curve with three distinct regimes: full film, mixed, and boundary lubrication. Friction in the full-film regime is determined by lubricant viscous shearing as contacting surfaces are completely separated by a hydrodynamic lubricant film such that asperity interaction is minimal or non-existent. Friction in the boundary lubrication regime depends on the properties of the boundary film and interactions between surface asperities. Friction in the mixed lubrication regime is due to both resistance within the fluid and at asperity contacts [235]. Therefore, friction can be categorized into two types - contact friction (mixed lubrication and boundary lubrication) associated with surface interactions and viscous friction (full film lubrication) entirely due to the fluid properties.

Unlike contact friction, viscous friction is determined by lubricant viscous shearing since the contacting surfaces are completely separated by a hydrodynamic lubricant film. Under this lubrication condition, asperity interactions are minimal or non-existent. Therefore, only viscous friction that doesn't involve asperity-asperity contact was investigated in

this study.

Currently there is a limited studies reporting viscous friction for phosphonium ILs. In one study viscous friction of [P6,6,6,14][3-Triaz] and [P4,4,4,12][3-Triaz] were compared with hydrocarbon lubricants by experiment. Results showed that both ILs outperformed hydrocarbon lubricants such as paraffin and hexadecane [236]. Viscous friction of phosphonium ILs as lubricant additive were also studied. Results showed that [P6,6,6,14][BEHP]/PAO 4 mixture presented similar viscous friction as pure PAO 4, while the [P6,6,6,14][$(iC8)_2PO_2$] mixture had a similar behavior compared to the ZDDP/PAO 4 mixture [237]. No simulation work was found for viscous friction for phosphonium ILs.

However, viscous friction for plenty of other ILs as lubricants have been reported by both experimental and simulation studies. For experiment studies, viscous friction of [BMIM] and [HMIM] paired with [BF_4] and [PF_6] was studied. It was found that viscous friction was determined by the inorganic anion as [PF_6] showed higher friction than [BF_4] [238]. Viscous friction and the tribo film formation on steel surfaces of three fatty acid -[N8,8,8,1][OctO], [N8,8,8,1][Lau], and [N8,8,8,1][Pmt] - were studied under different entrainment speeds at different temperatures. It was found [N8,8,8,1][Lau] and [N8,8,8,1][Pmt] showed lower traction coefficient than [N8,8,8,1][OctO], and the thickness of the tribofilm was highest for the [N8,8,8,1][Pmt] [239]. For another three fatty acid -[N8,8,8,1][HexO], [N8,8,8,1][Ste], and [N8,8,8,1][Ole], [N8,8,8,1][HexO] and [N8,8,8,1][Ste] exhibited similar viscous friction behavior at 40 and 60 °C. At high temperatures and low speeds [N8,8,8,1][HexO] showed the lowest viscous friction values, while [N8,8,8,1][Ole] showed higher viscous friction values [240].

There are also molecular dynamics simulation studies about viscous friction for non-phosphonium ILs [165–169, 177, 178]. For the effect of ion pairs, it has been shown that the length and branching of the alkyl chains in the cation and the anion chemistry played a vital role in determining physico-chemical and lubricating properties of phosphonium ILs [20, 241, 242]. Since viscous friction is only related to liquid property, ion pairs can also affect viscous friction for ILs. For the effect of cation, some studies reported that longer alkyl chains correspond to lower viscous friction. For example, [P6,6,6,14][3-Triaz] showed lower viscous friction than [P4,4,4,12][3-Triaz] under all slide-to-roll ratio studied [236].

The anion moiety also affect viscous friction. When paired with [BMIM] and [HMIM] cations, [PF_6] showed higher viscous friction than [BF_4] [238]. It was reported that viscous friction is lower for fatty acid anions with longer alkyl chains as [N8,8,8,1][Lau]

and [N8,8,8,1][Pmt] showed lower traction coefficient than [N8,8,8,1][OctO]. This was attributed to a linear relationship between tribofilm thickness, which control friction reduction, and alkyl chain length, as the thickness of the tribofilm was highest for [N8,8,8,1][Pmt] [239].

Results reported so far have shown that cation and anion can affect viscous friction. However, there has been no systematic study of these effects for phosphonium ILs nor the underlying mechanisms. A full understanding of how ion pair affect viscous friction of phosphonium ILs is required to optimize phosphonium ILs' application in lubrication. Since the difference in anions is much more complicated than phosphonium cations, here we mainly focus on the the effects of the phosphonium cations paired with identical anions. Although there are several categories of phosphonium cations [241], tetraalkylphosphonium cations only containing alkyl chains were investigated. As viscous friction is highly dependent on shear rate [243], the effect of shear rate was also considered.

Table 4.1: Chain length parameter *CL* and chain symmetry parameter *CS* for different cations.

Cations	Length (*CL*)	Symmetry (*CS*)
[P1,1,1,5]	2.000	2.333
[P2,2,2,2]	2.000	1.000
[P2,2,2,8]	3.500	2.000
[P4,4,4,2]	3.500	1.167
[P2,2,2,10]	4.000	2.333
[P4,4,4,4]	4.000	1.000
[P4,4,4,6]	4.500	1.167
[P4,4,4,8]	5.000	1.333
[P4,4,4,10]	5.500	1.500
[P4,4,4,12]	6.000	1.667
[P6,6,6,6]	6.000	1.000
[P6,6,6,14]	8.000	1.444
[P8,8,8,8]	8.000	1.000

In this study, 13 phosphonium cations, as listed in Table 4.1, were included to allow a systematic investigation of the effects of alkyl chain length and alkyl chain symmetry on viscous friction. In particular, [P1,1,1,5], [P2,2,2,2], [P2,2,2,10],[P4,4,4,4], [P4,4,4,12], [P6,6,6,6], [P6,6,6,14], and [P8,8,8,8] were compared for the effect of alkyl chain length and alkyl chain symmetry separately, while [P4,4,4,4], [P4,4,4,6], [P4,4,4,8], [P4,4,4,10], and [P4,4,4,12] were compared for the combined effect of alkyl chain length and alkyl chain

symmetry. After the model between viscous friction and alkyl chain length, alkyl chain symmetry, and shear rates was established, another two cations [P2,2,2,8] and [P4,4,4,2] were used for model validation. The anions used in the current study were the halogen-based [Tf_2N], which is the most frequently used anion in previous studies [241], and bio-based [Sacc], which is used to demonstrate that the cation trends observed are applicable for multiple anions.

4.2 Non-equilibrium molecular dynamics simulations

Modeling the dynamic behavior of fluid molecules confined between two solid surfaces is the most common approach to simulate friction. In this approach, a constant pressure is applied in the surface-normal direction and solid surfaces are slid simultaneously with a constant velocity to shear the liquid. However, since viscous friction is only related to fluid properties, a simple approach can be applied to calculate viscous friction. In this methodology, the pressure and shear are applied directly to the fluid molecules by deforming the simulation box without confining walls [243]. Since there is no solid surface and solid–fluid interactions, this simulation approach is very computationally efficient compared to the common approach as mentioned above.

Table 4.2: Experiment Parameters for Coefficient of Friction Tests (data from P. Menezes and H. Rahman at University of Nevada, Reno).

Disk	SS 52100 stainless steel
Ball	SS 440C stainless steel
Ball diameter	6.33 mm
Load	80 N
Speed	0.26 m/sec
Test period	1 h
Hertzian contact pressure	2740.2 MPa

This approach mainly includes two steps, loading simulations and then non-equilibration molecular dynamics (NEMD) simulations. First, in loading simulations, normal pressures of 0.9, 1.8, or 2.7 GPa will be applied after the liquid system is fully equilibrated at 40 °C and 1 atm. The highest normal pressure used here was selected to match that calculated based for experiment measurement conditions (data from P. Menezes and H. Rahman

at University of Nevada, Reno) as listed in Table 4.2. Following the simulation protocol from previous study, the size of the simulation box was decreased in the direction of the applied normal pressure until that the component of stress tensor, or pressure, in this direction reached the target value. Then, the simulation with the new size was run in the NVT ensemble at 40°C for 5 ns followed by the NVE ensemble for 5 ns to relax the system [243].

Based on experiment measurement conditions, the shear rate was calculated as 1.4×10^7 1/s. However, this shear rate is too low for the simulation to converge. Therefore, in the second step, NEMD simulations were carried out at three shear rates, 1×10^9, 1×10^{10}, and 1×10^{11} 1/s. In this step, the shear rate was imposed on the simulation box by deforming it in the direction perpendicular to the normal pressure direction. After the system to achieves steady state as the goodness of a linear fit to the average atom velocities was 98% or greater, the normal pressure and shear stress were collected for post processing. Here normal pressure and shear stress are the two components of pressure tensor P_{zz} and P_{xz} calculated based on virial theorem by summing the contributions from pairwise interactions between atoms [244]. The average shear stress vs. normal pressure data was fit linearly at each shear rate, and the slope taken is the viscous friction [245, 246]. Am example of how viscous friction is obtained for [p6,6,6,14][Tf_2N] and [p6,6,6,14][Sacc] at three different shear rates is shown in Fig 4.1. More details of simulation protocol can be found in previous study[243].

4.3 Viscous friction trends comparison

Viscous Friction results for eight phosphonium cations - [P1,1,1,5], [P2,2,2,2], [P2,2,2,10],[P4,4,4,4], [P4,4,4,12], [P6,6,6,6], [P6,6,6,14], and [P8,8,8,8] - paired with [Tf_2N] and [Sacc] is shown in Fig 4.2. It is observed that cations with longer chains showed higher viscous friction as the trends follow by [P1,1,1,5] $<$ [P2,2,2,10] $<$ [P4,4,4,12] $<$ [P6,6,6,14] for phosphonium cations with asymmetry alkyl chains and [P2,2,2,2] $<$ [P4,4,4,4] $<$ [P6,6,6,6] $<$ [P8,8,8,8] for phosphonium cations with symmetry alkyl chains. Cations with more symmetric structure showed higher viscous friction for all four symmetry and asymmetry phosphonium cations with the same alkyl chain length.

These two observations are consistent with previous study showed that either longer alkyl chain or higher cation symmetry induce a higher viscosity for phosphonium ILs. For the effect of alkyl chain length, more carbons per chain increase interionic interaction.

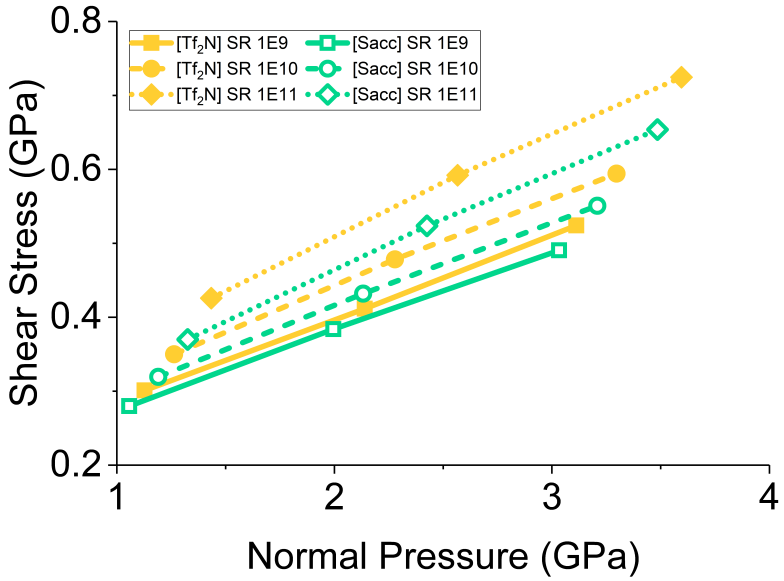

Figure 4.1: Shear stress vs.normal pressure from simulations of [p6,6,6,14][Tf_2N] and [p6,6,6,14][Sacc] at three different shear rates. The slope of the linear fit at each shear rate is the viscous friction.

Higher symmetry causes closer packing among ions and thus stronger interionic interactions. As a result, the resistance to shear flow increased by these two effects and a higher viscosity is induced [127]. Since viscous friction is directly related to fluid viscosity, these two effects could affected viscous friction in a similar manner.

Viscous Friction results for another five phosphonium cations [P4,4,4,4], [P4,4,4,6], [P4,4,4,8], [P4,4,4,10], and [P4,4,4,12] were compared for the combined effect of alkyl chain length and alkyl chain symmetry as shown in Fig 4.3. Interestingly, the viscous friction trend didn't increase monotonically with alkyl chain length. Instead, viscous friction decreased first as [P4,4,4,4] $>$ [P4,4,4,6] $>$ [P4,4,4,8] and then increased as [P4,4,4,8] $<$ [P4,4,4,10] $<$ [P4,4,4,12]. Among [P4,4,4,4], [P4,4,4,6] and [P4,4,4,8], the former has a slightly higher symmetry, but the latter has a slightly longer alkyl chains. According to the viscous friction trend, the effect of higher symmetry is over longer alkyl chains for these three cations. However, for [P4,4,4,8], [P4,4,4,10], and [P4,4,4,12], the effect of longer alkyl chains is over higher symmetry chains. This could be attributed to the fact that the degree of symmetry becomes lower for these three cations. These results showed that there is actually competition between alkyl chain length and alkyl chain symmetry. This com-

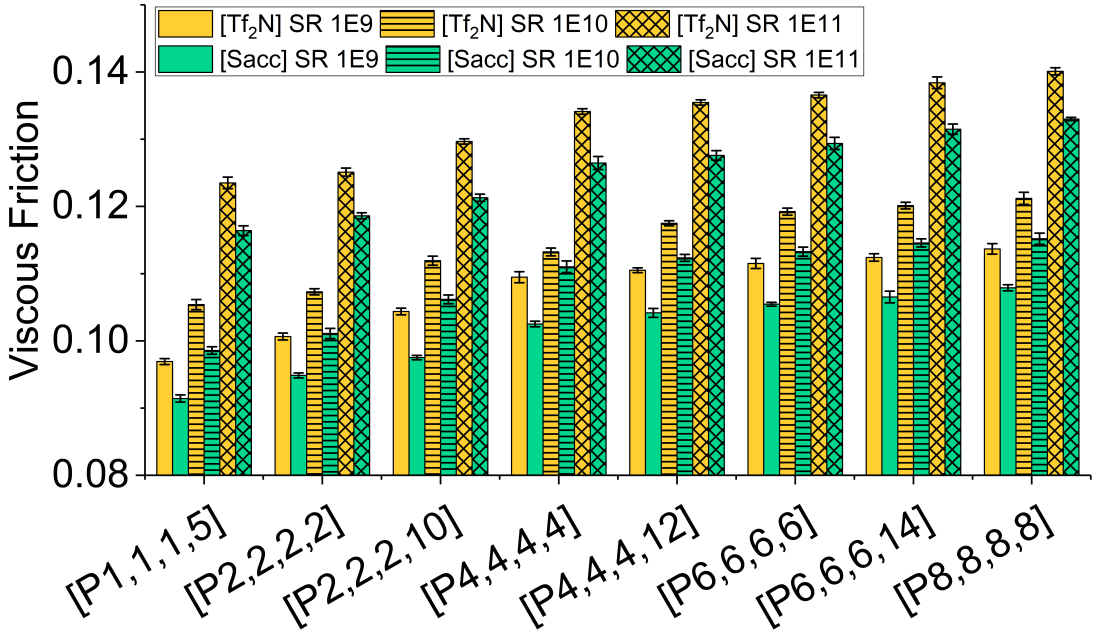

Figure 4.2: Viscous friction trends for the effect of alkyl chain length and alkyl chain symmetry, separately.

bined effect was also found on viscosity among [P4,4,4,4][DEHP], [P4,4,4,8][DEHP] and [P4,4,4,14][DEHP] as the viscosity turns out to be similar between [P4,4,4,8][DEHP] and [P4,4,4,14][DEHP], but the effect of cation symmetry was more significant between for [P4,4,4,4][DEHP] and [P4,4,4,14][DEHP] [127].

Although viscous friction increases with shear rate and phosphonium ILs with [Tf_2N] anion showed higher viscous friction than that of [Sacc], the effect of alkyl chain length and alkyl chain symmetry is independent on shear rate and anion types.

4.4 Viscous friction prediction model based on multiple linear analysis

In previous study, predictive model for viscous friction was established by molecule properties based on molecule chemistry and positions of atoms in the simulations [243]. However, for tetraalkylphosphonium cations, cation alkyl chain length and chain symmetry are better parameters to quantify the difference between cation structures. Since viscous friction

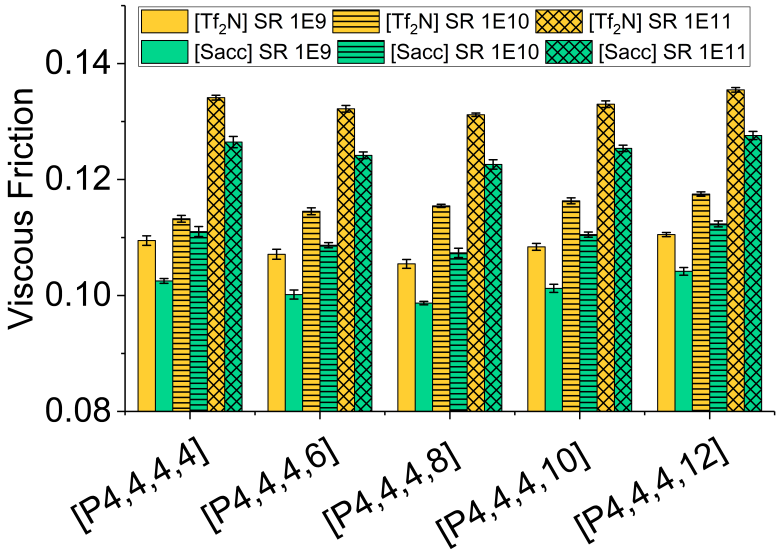

Figure 4.3: Viscous friction trends for the combined effect of alkyl chain length and alkyl chain symmetry.

is highly related to shear rate, multiple linear regression was used to establish predictive model that correlate viscous friction with cation alkyl chain length, chain symmetry, and shear rate for tetraalkylphosphonium ILs.

For the 13 tetraalkylphosphonium cations, chain length parameter *CL* is defined as the average number of C atoms per alkyl chain, and chain symmetry parameter is defined as $CS = 1 + |\frac{NCS-NCA}{NS \times NCS}|$, where *NCS* is the number of C atoms of symmetric chains, *NCA* is the number of C atoms of asymmetric chains, and *NS* is the number of symmetric chains. The *CL* and *CS* for different cations are summarized in Table 4.1. As viscous friction increases nonlinearly with shear rate, the logarithm with base 10 of the shear rate $log_{10}(SR)$ is used to quantify the effect of shear rates.

For viscous friction prediction model, viscous friction for nine out of eleven cations types under each shear rate were randomly selected for model establishment as shown by the black data points in Fig 4.4a. The other two cations were used for model testing as shown by the red data points. The relationship between viscous friction and *CL*, *CS*, and $log_{10}(SR)$ was then established for phosphonium cations paired with [Tf_2N] first as shown by the blue line in Fig 4.4a. The model for viscous friction was obtained as $VF = 0.01615 + 0.01275 \cdot log_{10}(SR) + 0.00217 \cdot CL - 0.00294 \cdot CS$ with $R^2 = 0.944$. A similar process was conducted with phosphonium cations paired with [Sacc] as shown in Fig 4.4c.

The model for viscous friction was obtained as $VF = -0.01642 + 0.01217 \cdot log_{10}(SR) + 0.00216 \cdot CL - 0.00321 \cdot CS$ with $R^2 = 0.958$. Based on the coefficients of each parameter and Fig 4.4b and d, it can be observed that viscous friction increases with $log_{10}(SR)$ and CL but decreases with CS for phosphonium cations paired with both anions.

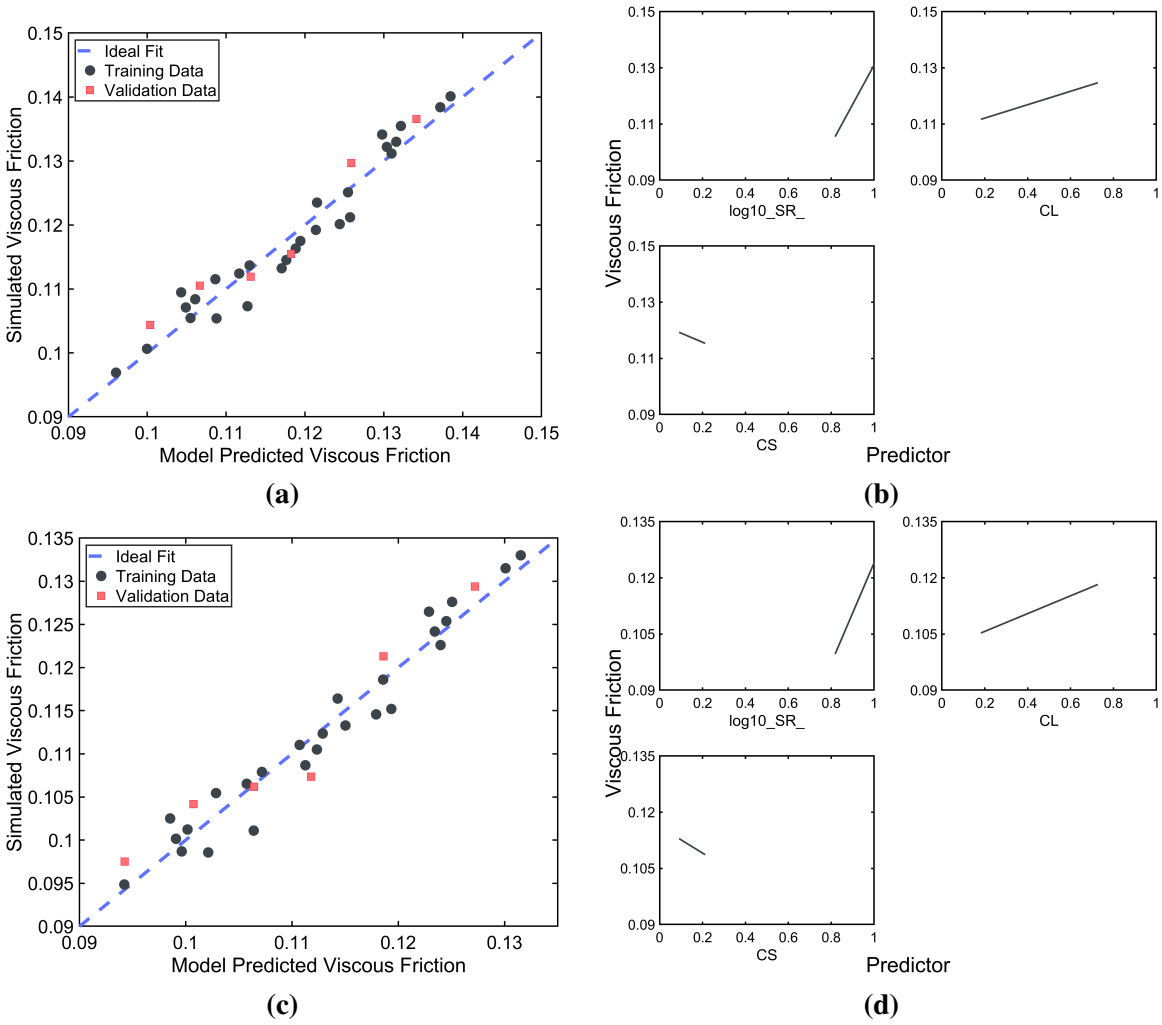

Figure 4.4: Multiple linear analysis model for viscous friction trends.

Since the models obtained for the two anions follow the same pattern, this indicates that the viscous friction trends among different phosphonium cations could be independent on different anion types. To test this hypothesis, viscous friction data were normalized based on the maximum value for each anion type. Then the normalized viscous friction values were combined by the two anion types for linear regression analysis to obtain a model

that relates normalized viscous friction and cation alkyl chain length, chain symmetry and shear rates. For this model, 54 out of 66 normalized viscous friction values were randomly selected for model establishment as shown by the black data points and the remaining 12 values were used for model testing as shown by the red data points in Fig 4.5a. The relationship between normalized viscous friction and CL, CS, and $log_{10}(SR)$ was then established as $VF^* = 0.119 + 0.09125 \cdot log_{10}(SR) + 0.01584 \cdot CL - 0.0226 \cdot CS$ with $R^2 = 0.953$. According to this model, viscous friction for tetraalkylphosphonium cations can be calculated as $VF = C_{an} \cdot VF^*$, where C_{an} is the normalizing constant for different anions. In current study, C_{an} is 0.141 for [Tf_2N] and 0.133 for [Sacc]. By comparing the geometric parameters for cations using the PyL3dMD Python package [247], the difference in normalizing constant is due to the difference in ion packing, for which phosphonium cations have denser packing for [Tf_2N] than [Sacc].

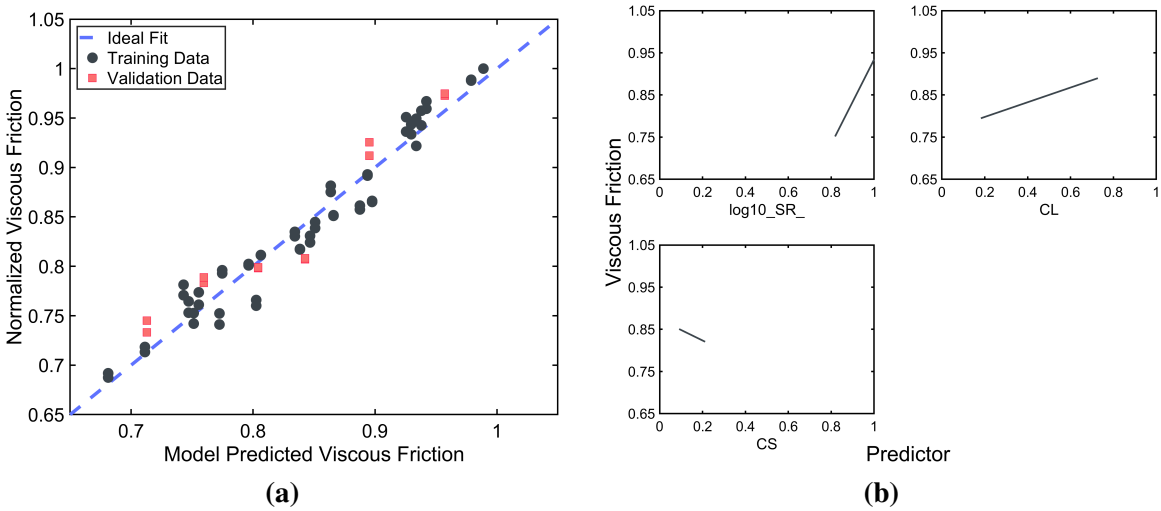

Figure 4.5: Multiple linear analysis model for viscous friction trends by normalizing two anion types.

In a previous study, a predictive model of viscous friction for polymers was established using molecule property parameters including relative shape anisotropy, molecular length, molecular weight, percentage molecular weight, and gyration tensor [243]. By comparing over 90 ion geometric parameters obtained by the PyL3dMD Python package [247] with the three parameters used in the predictive model, here how alkyl chain length, chain symmetry and shear rate related to ion property parameters was also analyzed. Alkyl chain length mainly affects parameters like relative shape anisotropy, asphericity, molecu-

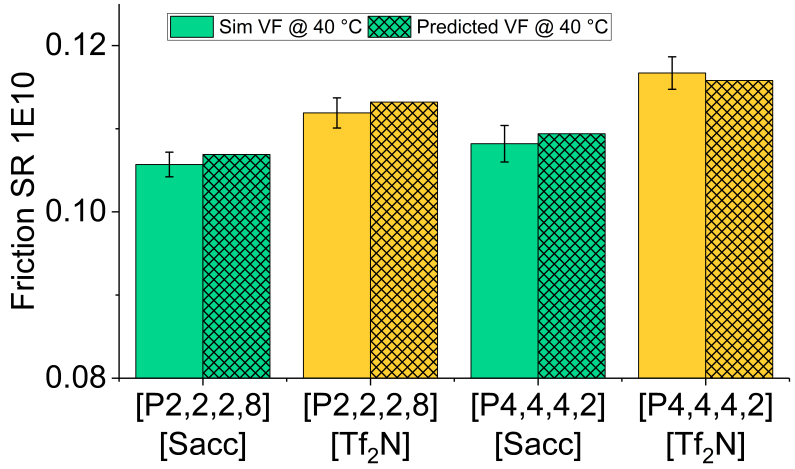

Figure 4.6: Comparison between viscous friction predicted by multiple linear analysis model under the shear rate of 1×10^{10} and coefficient of friction from experiment.

lar length, molecular weight, radius of gyration, and end-to-end distance. These parameters are highly related to interionic interactions. Alkyl chain symmetry mainly affects acylindricity, molecular eccentricity, folding degree index and dipole moment. Shear rate mainly affects molecular length in all directions and the length to width ratio of molecules, which in return affects relative shape anisotropy, asphericity, and acylindricity.

To validate the predictive model, viscous friction calculated based on the obtained model and NEMD simulations for two cations - [P2,2,2,8] and [P4,4,4,2] - under shear rate of 1×10^{10} 1/s are compared as shown in Fig 4.6. It is observed that the model accurately predicts viscous friction for these two cations paired with [Tf_2N] and [Sacc]. MD simulations cannot directly reach the shear rate at experiment conditions, but this model may be able to predict viscous friction for tetraalkylphosphonium ILs under low shear rates close to experiment conditions.

4.5 Conclusions

Viscous friction of 22 tetraalkylphosphonium ILs (11 cations paired with 2 anions) was calculated using non-equilibrium MD simulation approach. By comparing viscous friction among different cations, it was found that viscous friction increases with longer alkyl

chains and decreases with higher alkyl chain asymmetry and there is a combined effect between chain length and symmetry. To capture the effects of cation moiety and operating conditions on viscous friction, a predictive model of viscous friction for tetraalkylphosphonium ILs with [Tf_2N] and [Sacc] anions was established by cation chain length *CL*, chain symmetry *CS*, and shear rate $log_{10}(SR)$ based on the obtained viscous friction values. The accuracy of the model was validated by another two cations not included during model establishment with good accuracy achieved. This model can be used to predict viscous friction for tetraalkylphosphonium ILs under low shear rates close to experiment conditions.

Chapter 5

Corrosion Behavior of Phosphonium ILs

5.1 Introduction

In many applications, ILs are in direct contact with a metal surface and form a solid-liquid interface. In such cases, ILs have been found to form adsorption layers composed of their decomposition products where the layers can have either a corrosive or protective effect, depending on the combination of IL and metal, as well as on temperature [248]. ILs are usually less corrosive than typical oxidizing species like water and oxygen [249], so they may be used as corrosion inhibitors for metals [250, 251]. However, many ILs are highly polar and have low vapor pressures, and therefore can be more corrosive to metal surfaces than traditional organic solvents [9, 252]. Generally, corrosion is a concern because it can reduce the strength and durability of equipment and structures [252, 253]. To minimize corrosion in applications involving ILs, it is important to understand the mechanisms by which ILs interact with and affect corrosion of metal surfaces.

There have been a number of experimental studies that have examined the corrosion of metals in contact with ILs. The rate of corrosion of metals interacting with ILs has been measured by the weight loss method using a rotating cage experiment [252, 254, 255]. Electrochemical tests, like corrosion potential, corrosion current density, and electrochemical impedance spectroscopy, have also been applied to measure corrosivity of ILs [249, 254–258]. Such studies reported that corrosion processes were controlled by charge transfer at the metal/IL interface [249, 255, 256, 259] and the corrosivity of ILs strongly depends on the surface material and morphology, the presence of impurities, and the tem-

perature [249, 252–257, 260, 261]. Corrosion of metals by ILs has also been shown to be affected by the chemical nature of the IL cation and anion [248, 249, 252, 253, 257, 258, 261, 262].

The cation can affect the way that ILs interact with metal surfaces and, therefore, the corrosion of the metal [248, 258, 261, 262]. For example, (2-hydroxyethyl)-trimethyl-ammonium bistriflimide (choline [Tf_2N]) caused less corrosion of a copper surface than butyl-trimethyl-ammonium [Tf_2N] [248]. The incorporation of a hydroxyl group into the cation alkyl side chain was found to decrease corrosivity [256]. Electrochemical tests showed that protic ILs had a narrower electrochemical stability window and were generally more reactive toward metals than aprotic ILs [258]. Corrosion of aluminium and copper in imidazolium-based ILs with different alkyl chain lengths showed that corrosion decreased with increasing alkyl chain length [261]. For steel surfaces, alkyl substituents like polar groups, fragments, conjugated bonds, and various heteroatoms in the cation structure led to lower corrosion rate due to the improved adsorption of cations on the surface [262].

It has also been reported that the anion moiety plays the dominant role in corrosion of metal surfaces [257, 258, 263] since the polarization behavior of ILs is mainly governed by anions [257]. For example, anions like tosylate and dimethyl phosphate generally had higher corrosivity on carbon steel and aluminium than ethyl sulfate, octyl sulfate, and chloride [252]. Severe corrosion on iron based alloys was found for choline methanesulfonate while choline [Tf_2N] exhibited significantly lower corrosiveness [256]. On copper surfaces, 1-ethyl-3-methylimidazolium phosphonate ([EMIM][$EtPO_3H$]) showed more corrosion than 1-ethyl-3-methylimidazolium octylsulfate ([EMIM][$C_8H_{17}SO_4$]) due to the formation of a soluble phosphonate-copper complex. Also, 1-hexyl-3-methylimidazolium tetrafluoroborate ([HMIM][BF_4]) showed more corrosion than 1-hexyl-3-methylimidazolium hexafluorophosphate ([HMIM][PF_6]) since the [BF_4] anion formed a soluble species with copper while the [PF_6] anion formed a uniform protective layer on the copper surface [263]. ILs composed of strongly coordinating anions such as bis(trifluoromethylsulfonyl)imide (TFSI) are more corrosive to metal surfaces than chloroaluminate ILs or ILs with weakly coordinating anions such as tetrafluoroborate (BF_4) and hexafluorophosphate (PF_6) because TFSI can facilitate metal dissolution by forming a tight solvation layer with dissolved metal ions [253].

Results reported so far have shown that the chemical nature of the ions can affect the corrosion of metal surfaces interacting with ILs and that the anion plays a key role. How-

ever, the mechanisms by which anions affect metal corrosion are still not fully understood. Here, we characterized corrosion of steel in the presence of phophonium ILs experimentally and then applied reactive molecular dynamics (MD) simulations to understand ion-surface interactions. We focused on phosphonium-based ILs that are used in various applications where they come into contact with ferrous materials [20, 36, 38, 241]. Specifically, we studied trihexyltetradecylphosphonium benzoate ([P6,6,6,14][Benz]) and trihexyltetradecylphosphonium salicylate ([P6,6,6,14][Sali]). These ILs have been used as lubricants for stainless steel [181] and the anions are derived from organic sources. [P6,6,6,14][Benz] and [P6,6,6,14][Sali] were also chosen because they have the same cation but slightly different anions. This enabled isolation of the effect of the anion such that the IL-surface interactions underlying trends observed in the experiments could be explained using the atomistic detail available in the reactive MD simulations.

5.2 Reactive Molecular Dynamics Simulation

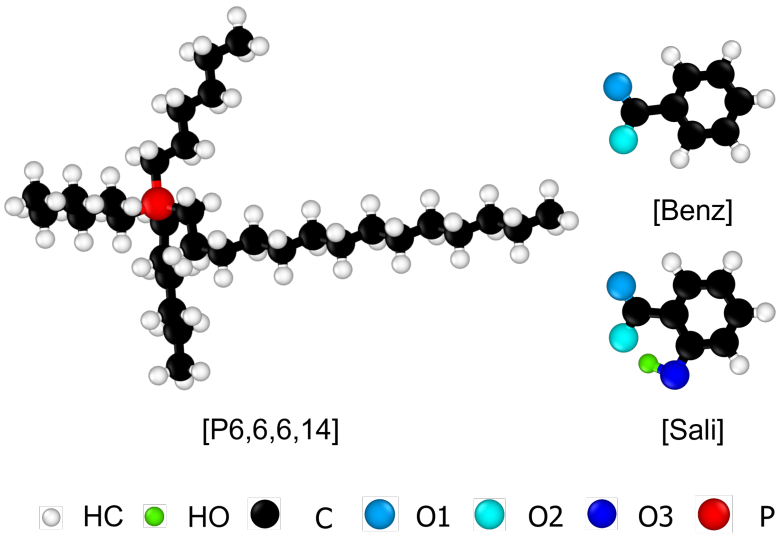

Figure 5.1: Chemical structures of the [P6,6,6,14] cation, [Benz] anion, and [Sali] anion evaluated in current study. HC: hydrogen atoms bonded to carbon atoms; HO: hydrogen atoms bonded to oxygen atoms; O1: oxygen type 1 of the carboxyl group; O2: oxygen type 2 of the carboxyl group; O3: oxygen atom in the hydroxyl group.

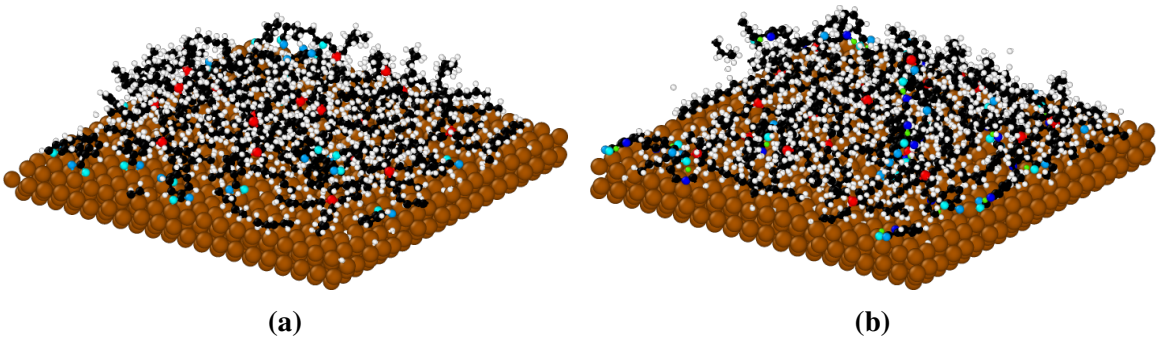

(a) (b)

Figure 5.2: Perspective-view snapshots at the end of the simulations at 300 K for (a) [P6,6,6,14][Benz] and (b) [P6,6,6,14][Sali].

As corrosion experiment results (carried out by P. Menezes and H. Rahman at University of Nevada, Reno) showed different corrosion behavior of [P6,6,6,14][Benz] and [P6,6,6,14][Sali] on AISI 52100 steel, reactive MD simulations of [P6,6,6,14][Benz] and [P6,6,6,14][Sali] on an ideal 56.8 $\times$ 56.8 Å Fe(100) surface were performed to complement the experiments. All simulations were performed using the open-source Large-scale Atomic/Molecular Massively Parallel Simulator (LAMMPS) package [183]. Simulations were based on the ReaxFF force field with parameters for Fe/P/C/H/O [84]. This potential has been used previously to model thermal decomposition of phosphonium benzoate and phosphonium salicylate [5]. The model system comprised a body-centered cubic Fe(100) slab and 20 ion pairs in a periodic simulation box. The structures of the individual ions are shown in Fig 5.1. The ion models were created by Packmol [223] and 20 ion pairs of either [P6,6,6,14][Benz] or [P6,6,6,14][Sali] were randomly placed 1 nm above the Fe(100) surface.

After energy minimization, the simulations were performed with a canonical ensemble with a time step of 0.25 fs. The temperature was maintained at 300 K with a damping parameter of 25 fs using a Nosé–Hoover thermostat [185]. During this simulation, the ions approached and reacted with the surface atoms. It was found that the number of ion-surface bonds reached steady-state after about 0.6 ns at 300 K. Therefore, the simulations were performed for a total duration of 1 ns by which time the potential energy of the simulation system and number of bonds had reached steady state. Simulations were also run at 400 K and 500 K for 1 ns. Fig. 5.2 show snapshots from the end of representative simulations after reactions between the ions and surface reached steady state. Chemical

bonding between atoms in ILs and Fe atoms in surface was analyzed based on the ReaxFF bond table using user-defined Python scripts. Results were averaged over 20 time frames during the last 25 ps of the simulation.

5.3 Results and Discussion

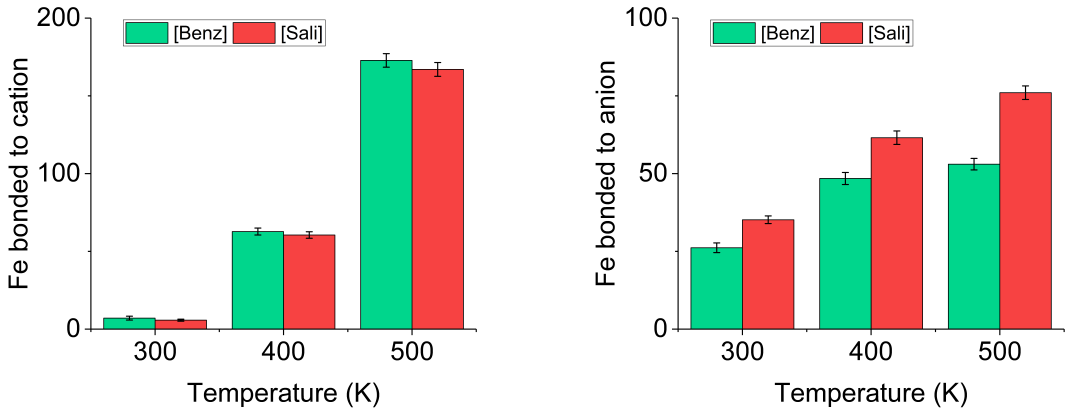

Figure 5.3: Steady-state number of Fe atoms bonded to (a) cations and (b) anions from simulations of the two ILs interacting with a Fe(100) surface at three different temperatures with error bars showing the standard deviation for three independent tests.

Simulations were used to investigate the interactions and reactions between the ILs and an ideal Fe(100) surface to understand the mechanisms underlying the experimentally observed trends. First, we analyzed the bonding between surface Fe atoms and the cations and anions in the ILs. As shown in Fig. 5.3, the surface bonding increased with temperature, as expected since more thermal energy facilitates bond dissociation and formation. There are more cation-Fe bonds than anion-Fe bonds because there is a greater number of atoms in the cations than the anions. However, comparing the two ILs, the key difference is observed for the anions where [Sali] exhibits more bonding with the surface than [Benz].

Since the cation is the same in both ILs and the difference between Fe-cation bonding for the two ILs was negligible, we focused subsequent analysis on reactions between Fe and the anions. Anion chemisorption reactions can occur through formation of either Fe–C or Fe–O bonds. The number of Fe atoms bonded to anion C or O atoms is given in Fig. 5.4.

This analysis shows that bonding with C is dominant for the [Sali] while O bonding is dominant for the [Benz] at all temperatures. Since the reactions with O atoms are the cause of corrosion, the Fe–O bonding was further analyzed, where oxygen atoms are identified by the labels in Fig. 5.2.

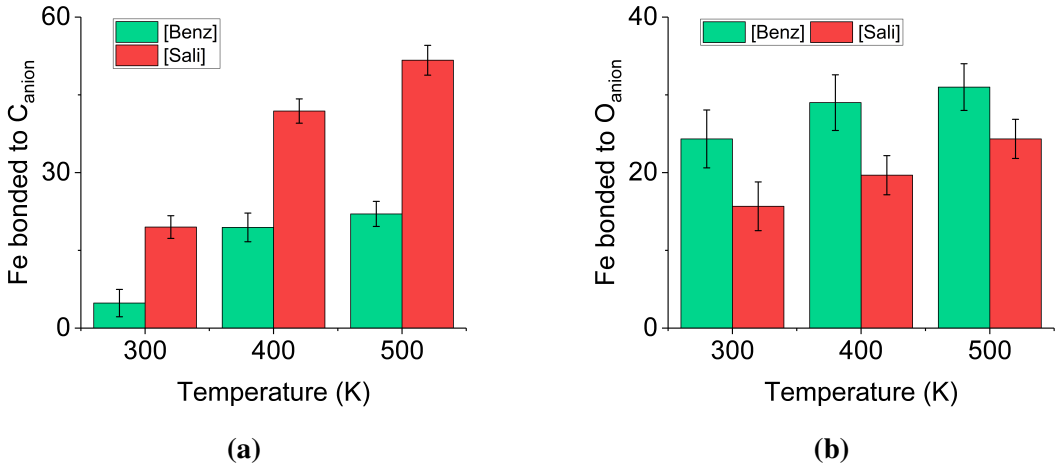

Figure 5.4: Steady-state number of Fe atoms bonded to (a) C atoms and (b) O atoms in the anions from simulations of the two ILs interacting with a Fe(100) surface at three different temperatures with error bars showing the standard deviation for three independent tests.

For [Benz], as shown in Fig 5.5(a), the number of Fe–O1 and Fe–O2 bonds was similar at all temperatures, as expected since the ion is symmetric. In these simulations, there were only two bonding scenarios: (i) Fe–O1 and Fe–O2 (Fe–O1&O2), or (ii) Fe–O1 or Fe–O2 (Fe–O1||O2). Snapshots of representative examples of these two bonding scenarios are shown in Figs. 5.5(b) and (c). The likelihood of each bonding scenario was calculated from the number of anions exhibiting a given bonding scenario divided by the total number of chemisorbed anions. The calculation was performed at the end of the simulation using data from all three temperatures (no statistical difference between the temperatures was observed). The anion reacted with the surface through Fe–O1&O2 bonding 93.1% of the time, consistent with a previous experimental study that reported bonding at the two O atoms in [Benz] and a TiO_2 surface [230]. The Fe–O1||O2 bonding scenario was only observed 6.9% of the time.

For [Sali], as shown in Fig. 5.6(a), the reactivity of the O atoms with Fe on the surface decreased as O1 $>$ O2 $>$ O3 at all temperatures. The O1 was more reactive than the O2 in [Sali] due to the presence of the hydroxyl group. As mentioned in a previous

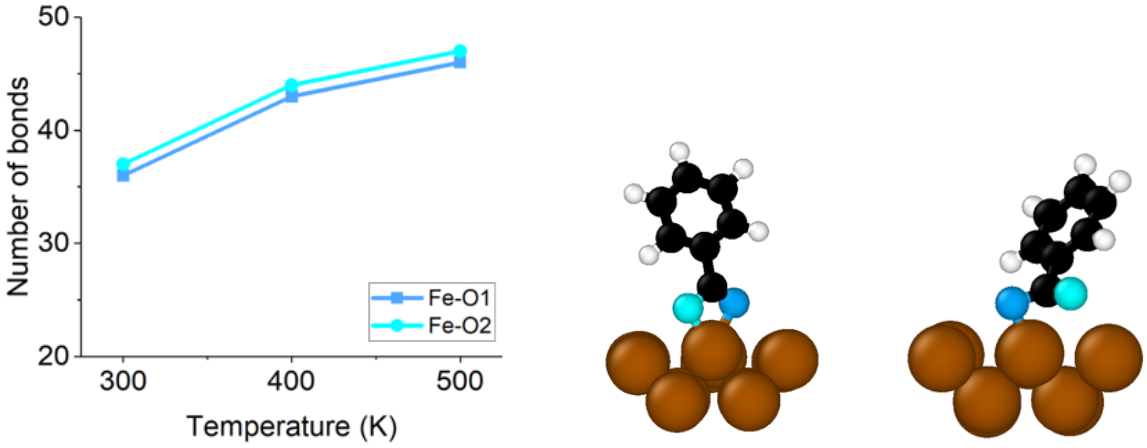

(a) **(b)** 93.1% **(c)** 6.9%

Figure 5.5: (a) Number of Fe–O1 and Fe–O2 bonds as a function of temperature for [Benz], with representative snapshots of the two possible bonding scenarios (b) Fe–O1&O2 or (c) Fe–O1‖O2, and the percent of all bonded anions in which each scenario was observed.

study, the hydroxyl group (H–O3) pointing to O2 indicates intramolecular interaction between the H atom in the hydroxyl group and O2, which hinders the ability of O2 to take part in reactions with other atoms [5]. For [Sali], there were four bonding scenarios: Fe–O1&O2, Fe–O1&O2&O3, Fe–O1, and Fe–O3. This is consistent with the multiple possible bonding scenarios for [Sali] on metal surfaces found in previous studies using experiments and simulations showing both the hydroxyl group and carboxyl group can interact with metal [233, 264–267]. Like [Benz], for [Sali], Fe–O1&O2 bonding was the dominant scenario with a probability of 51.9%. This was followed by Fe–O1&O2&O3 with 22.3%, Fe–O1 with 19.1%, and Fe–O3 with 6.7%. In [Sali,] both the carboxyl group and the hydroxyl groups can interact with Fe atoms [268], so there are more possible bonding scenarios for [Sali] than [Benz].

For both [Benz] and [Sali], the key difference between the different bonding scenarios is the orientation of the benzene ring relative to the surface. The orientation of anions has previously been found to affect the interaction between ILs and surfaces. For example, anion orientation was found to affect metal-IL binding energy [242, 269], IL film formation on alumina [270], and interactions between ILs and graphene [229]. Therefore, the anion orientation for each Fe–O bonding scenario was analyzed for both ILs.

Anion orientation angle was calculated as the angle between the anion plane (defined

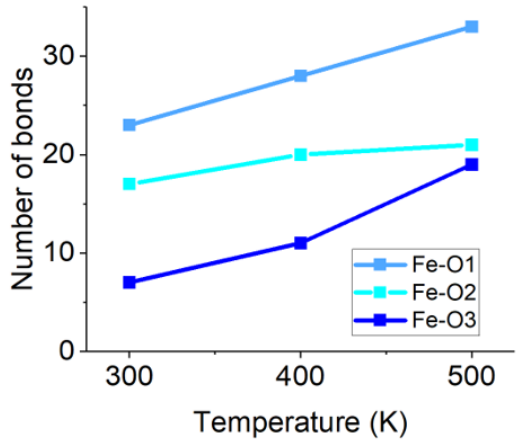

(a)

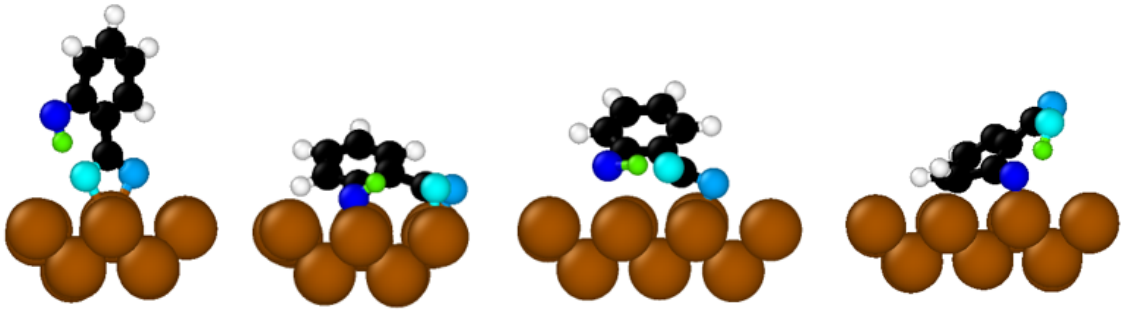

(b) 51.9% **(c)** 22.3% **(d)** 19.1% **(e)** 6.7%

Figure 5.6: (a) Number of Fe–O1, Fe–O2, and Fe–O3 bonds as a function of temperature for [Sali] with representative snapshots of the four possible bonding scenarios (b) Fe–O1&O2, (c) Fe–O1&O2&O3, (d) Fe–O1 or (e) Fe–O3, and the percent of all bonded anions in which each scenario was observed.

by the positions of O1, O2, and the carbon atom in the benzene ring farthest from the carboxyl group), and the plane of the Fe(100) surface. This calculation was performed for each bonding scenario observed in simulations at all three temperatures (no difference in the trends was observed at the different temperatures). As shown in Fig 5.7, the anions with Fe–O1&O2 bonding tended to be orientated more vertically (angles approaching 90°) than the other bonding scenarios for both anions. The frequency of Fe–O1&O2 bonding scenario was much higher for [Benz] than [Sali], indicating [Benz] was oriented more vertically relative to the ferrous surface than [Sali]. This is consistent with the dominant O bonding for the [Benz] and dominant C bonding for the [Sali] observed in Fig 5.4.

The vertical orientation of [Benz] anions enabled more [Benz] anions to reach the sur-

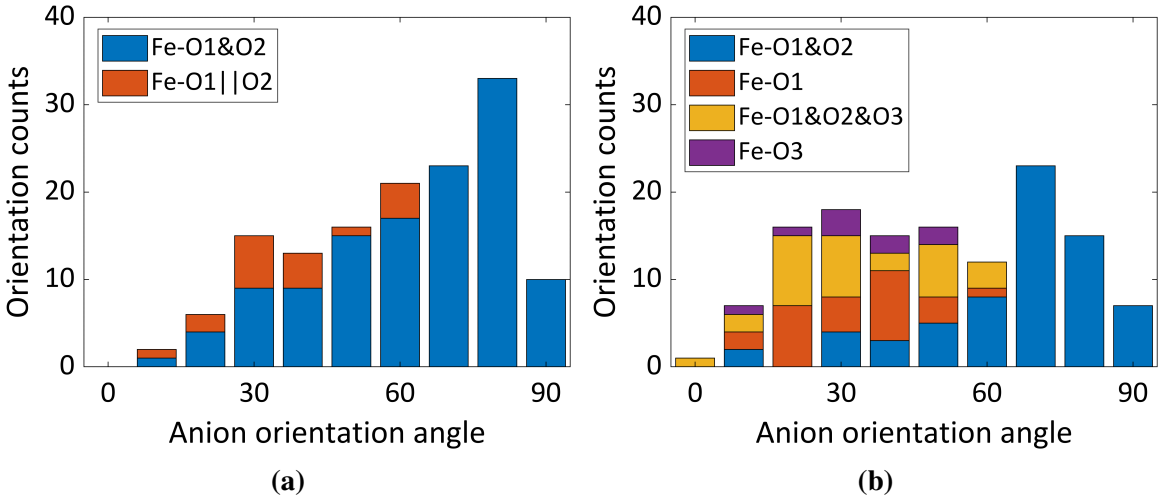

Figure 5.7: Distribution of the anion orientation angle relative to the surface (at 0°, the benzene ring is parallel to the surface and at 90°the ring is perpendicular to the surface) for the different Fe–O bonding scenarios exhibited by (a) [Benz] and (b) [Sali].

face than the [Sali]. This was confirmed by calculating the average anion number density (number of ions per nm^2) chemisorbed on the surface, which was found to be 0.42, 0.58, and 0.62 for [Benz] and 0.25, 0.39, and 0.41 for [Sali] at the three different temperatures. A previous study also reported that [Benz] can be absorbed more easily on ferrous surfaces compared to [Sali] [268]. The higher density of [Benz] can lead to a faster rate of charge transfer at the metal/IL interface, consistent with the higher OCP voltage magnitude in Fig. **??** and higher PDP current flow in Fig. **??** for [P6,6,6,14][Benz] than [P6,6,6,14][Sali].

The orientation of the ions on the surface also affects the stability of the Fe-anion complexes formed. It has been reported previously that Fe-[Sali] complexes are stronger and more stable than Fe-[Benz] complexes [268]. Here, the relative stability of the two anions on the surface was estimated using the Fe–O bond order available from ReaxFF [153]. The results in Fig. 5.8(a) show that the bond order was consistently higher for [Sali], indicating stronger bonds and greater stability of the Fe–[Sali] complex. The bond order analysis was repeated for each oxygen atom separately and, as shown in Fig. 5.8(b), the strongest Fe–[Sali] bonds were for O3. This bonding site was not available in [Benz], leading to lower chemical stability of the Fe-[Benz] complex. This may explain the qualitative differences between the ILs in the long-duration corrosion tests in Fig. **??**. Since Fe-[benz] complexes are relatively unstable chemically, they are more likely to dissociate, promoting dissolution

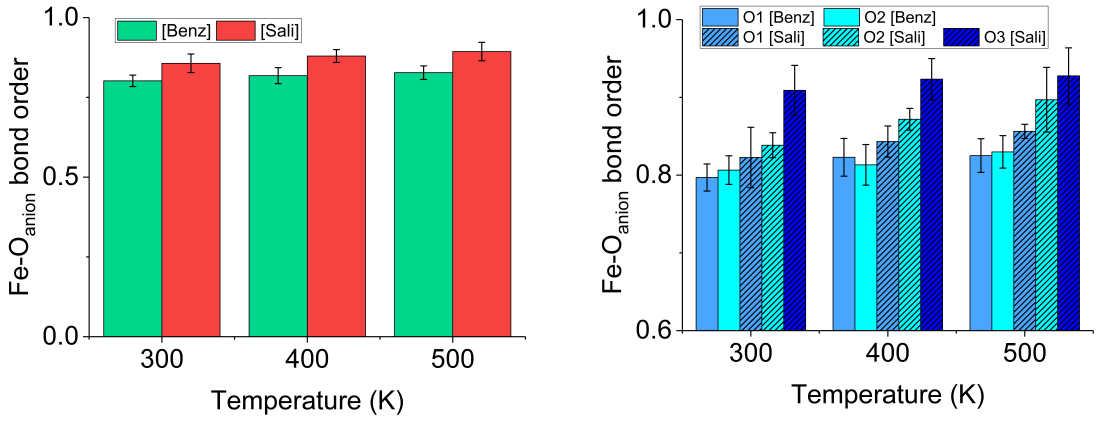

Figure 5.8: Steady-state Fe–O bond order (a) for the two anions and (b) separated by O type at three different temperatures with error bars showing the standard deviation for three independent tests.

of the surface and making available new active sites for subsequent corrosion reactions. The dissolution of the ferrous surface is localized around the initial Fe–O bonding leading to, over time, the formation of deep and narrow corrosion pits. In contrast, the stability of the Fe-[Sali] complexes hinders localized dissolution and leads to subsequent bonding and dissolution over a larger area, resulting in the formation of wider and shallower corrosion pits.

5.4 Conclusions

Reactive MD simulations and experimental corrosion tests were used to explore the interactions between ferrous surfaces and phosphonium benzoate or phosphonium salicylate. From experiments, both ILs showed much less corrosion of steel than water. However, OCP, PDP and surface topography analysis showed that the corrosion behavior of the two ILs differed, with the [Benz]-based IL exhibiting higher OCP magnitude and narrower, deeper corrosion pits. To understand these differences, simulations were used to investigate IL-surface interactions. The key observations were that the interactions between Fe and [Benz] were localized at the O atoms in the carboxyl group leading to preferentially vertical alignment relative to the surface. In contrast, the interactions between Fe and [Sali]

were distributed across the anion such that [Sali] had more possible bonding scenarios and tended to be oriented parallel to the surface. These results confirm previous observations that the anion plays a critical role in the corrosion behavior of ILs and further show that the effect is important even for anions that are not typically considered corrosive. The sensitivity of the corrosion to the anion is emphasized by the fact that the chemical difference between [Benz] and [Sali] is so subtle. For these two anions, the reactive simulations showed that the orientation of the anion after bonding to the surface can directly affect corrosion behavior, indicating both chemical and physical factors determine the corrosivity of ILs on ferrous surfaces.

Chapter 6

Summary and Future Work

6.1 Summary

This research aimed to study the relationship between tribology-related properties and cation & anion chemistry for phosphonium ILs that can ultimately be used to guide the design of high performance phosphonium ILs lubricants and lubricant additives. Toward this goal, classical MD simulations were used to study bulk properties, wetting behavior, and viscous friction while reactive MD simulations were used to study corrosion behavior. The molecular scale mechanisms underlying the mechanical response of phosphonium ILs with different cation and anion combinations were thoroughly discussed to establish the structure-property relationship for phosphonium ILs.

First, research performed using MD simulations to explore the lubricant-relevant properties of phosphonium ILs was summarized. This review demonstrated the significant potential for simulations to play an important role in the development of phosphonium ILs as environmentally benign lubricants and additives. More importantly, this review provided guidelines for how to choose potentials for MD simulations and apply analysis methods to explain observations and trends in physico-chemical properties.

Then classical MD simulations with non-reactive OPLS-AA force field were used to predict bulk properties, including density, viscosity, and ionic conductivity. In particular, the effect of anions on these bulk properties was analyzed. The accuracy of the modeling approach was evaluated by comparing to experiment/literature data. The accuracy in predicting bulk properties provided confidence for using this force field to investigate the

wetting behavior and frictional behavior.

Next, the wetting of phosphonium ILs with systematically varied cation and anion combinations on ferrous surfaces was evaluated using experiments and MD simulations. Contact angles of less than 20° in experiments indicated that the ILs have a good wettability on stainless steel, but contact angles are different for [Benz], [Sali], and [Sacc]. The same trend was reproduced in MD simulations. Next, the simulations were extended to include five different cations [P4,4,4,4], [P4,4,4,8], [P4,4,4,14], [P6,6,6,14], and [P8,8,8,14] in combination with three anions. It was found that longer alkyl chains in the cations led to lower contact angle. This was explained by the effect of more C atoms that both increased adhesion with the substrate and separated the P atom in the cation from the anion, thereby decreasing cohesion. For anions, the contact angle increased as [Benz] $<$ [Sali] $<$ [Sacc] when paired with the same cation. Like the cations, the anion contact angle trend was consistent with cohesion energy, and explained by the number and type of atoms in the anions that had attractive interactions with P atom in the cations. The adhesion energy was also consistent with the anion contact angle trend, but this case was explained by the orientation of the anions with respect to the surface. Specifically, perpendicular anion alignment allowed the cations more access to the surface, thereby increasing adhesion. The alignment trends were associated with asymmetry of the anion structures, where greater symmetry led to more perpendicular alignment, higher cation-Fe adhesion, and lower contact angle.

Viscous friction was investigated for 11 cations paired with 2 anions using non-equilibrium MD simulations. By comparing viscous friction among different cations, it was found that viscous friction increases with longer alkyl chains and decreases with higher alkyl chain asymmetry and there is a combined effect between chain length and symmetry. To capture the effect of cation moiety and operating conditions on viscous friction, a the predictive model of viscous friction for tetraalkylphosphonium ILs with [Tf_2N] and [Sacc] anions was established by cation chain length CL, chain symmetry CS, and shear rate $log_{10}(SR)$ based on the obtained viscous friction values. The accuracy of the model was validated by another two cations not included during model, showing that good accuracy was achieved. This model can be used to predict viscous friction for tetraalkylphosphonium ILs under low shear rates close to experimental conditions.

Reactive MD simulations and experimental corrosion tests were used to explore the interactions between ferrous surfaces and phosphonium benzoate or phosphonium salicylate. From experiments, both ILs showed much less corrosion of steel than water. However,

OCP, PDP and surface topography analysis showed that the corrosion behavior of the two ILs differed, with the [Benz]-based IL exhibiting higher OCP magnitude and narrower, deeper corrosion pits. To understand these differences, simulations were used to investigate IL-surface interactions. The key observations were that the interactions between Fe and [Benz] were localized at the O atoms in the carboxyl group leading to preferentially vertical alignment relative to the surface. In contrast, the interactions between Fe and [Sali] were distributed across the anion such that [Sali] had more possible bonding scenarios and tended to be oriented parallel to the surface. These results confirm previous observations that the anion plays a critical role in the corrosion behavior of ILs and further show that the effect is important even for anions that are not typically considered corrosive. The sensitivity of the corrosion to the anion is emphasized by the fact that the chemical difference between [Benz] and [Sali] is so subtle. For these two anions, the reactive simulations showed that the orientation of the anion after bonding to the surface can directly affect corrosion behavior, indicating both chemical and physical factors determine the corrosivity of ILs on ferrous surfaces.

6.2 Future work

Overall, this study provided fundamental understanding of correlations between tribology-related properties and cation and anion chemistry for phosphonium ILs, which can ultimately be used to guide the design of high performance phosphonium ILs lubricants. Although the scope of this study was limited to phosphonium ILs, the structure-property relationship discussed in this study are relevant to other IL types. However, there are still many aspects remaining to be investigated to fully understand the tribological properties of investigating phosphonium ILs.

First, the current study mainly focused on tetraalkylphosphonium ILs. As mentioned in Section 1.2, there are several types of phosphonium ILs. The structure-property relationship obtained for tetraalkylphosphonium ILs may not be the case for other types of phosphonium ILs, which requires further investigation. However, potentials currently available for both classical and reactive MD simulations can only accommodate anions with specific chemistries. Therefore, the anion types investigated in current study was limited. Future studies could investigate and quantify the effect of anion type.

Second, the presence of other chemical species can significantly affect the bulk prop-

erties of ILs. For the use of ILs in lubricants additives, the effects of water and base oil are particularly important. The effect of water is relevant because water is known to be introduced during IL synthesis [144–147] and phosphonium ILs are applied in water-based lubricants [271–273]. However, previous studies mainly focused on solubility of phosphonium ILs in water [4, 7, 81, 91, 96, 102, 104, 133]. These studies have shown that the presence of water molecules can affect anion-cation interactions, which in turn may affect properties like density, viscosity, polarity, conductivity, and solubility. However, there are few studies investigating how these properties change due to the presence of water. Therefore, there is a need to explore how water interact with cations and anions in phosphonium ILs and then affect trobology-related properties in atomistic level. Particularly, it is important to understand how water interacts with anions and cations and through what mechanisms water interactions affect fluid properties.

Interactions with base oil are important because phosphonium ILs are also used as additives in smaller amounts in lubricant formulations, to decrease cost [35]. When phosphonium ILs are used as additives, they will necessarily interact with base oil molecules, so there is a need to understand how ILs interact with base oil molecules. MD simulations have not been used for this purpose so far. Therefore, MD simulations can be carried out to gain a fundamental understanding of such interactions at a molecular level to understand the function of phosphonium ILs as an additive in oil-based lubricants.

Although viscous friction is entirely dependent on fluid properties, the fluid is in contact with surfaces and the solid-liquid interaction during sliding also affect frictional behavior. Therefore, frictional behavior for phosphonium ILs confined between walls should also be studied to directly compare with experiment. Since friction is affected by surface material, polarity, roughness, and charge because these factors affected the orientation and order of the ions [165–169, 177, 178]. Future MD simulations could use similar methods to model phosphonium ILs with different solid materials to explore interactions between the ILs and surfaces, and the corresponding tribological behavior.

Bibliography

[1] X. Liu, Y. Zhao, X. Zhang, G. Zhou, and S. Zhang, *Microstructures and interaction analyses of phosphonium-based ionic liquids: a simulation study*, J. Phys. Chem. B **116**, 4934–4942 (2012).

[2] Y.-L. Wang, F. U. Shah, S. Glavatskih, O. N. Antzutkin, and A. Laaksonen, *Atomistic insight into orthoborate-based ionic liquids: force field development and evaluation*, J. Phys. Chem. B **118**, 8711–8723 (2014).

[3] B. Zhang, A. C. van Duin, and J. K. Johnson, *Development of a ReaxFF reactive force field for tetrabutylphosphonium glycinate/CO2 mixtures*, J. Phys. Chem. B **118**, 12008–12016 (2014).

[4] Y.-L. Wang, S. Sarman, S. Glavatskih, O. N. Antzutkin, M. W. Rutland, and A. Laaksonen, *Atomistic insight into tetraalkylphosphonium-bis (oxalato) borate ionic liquid/water mixtures. I. Local microscopic structure*, J. Phys. Chem. B **119**, 5251–5264 (2015).

[5] A. Khajeh, M. H. Rahman, T. Liu, P. Panwar, P. L. Menezes, and A. Martini, *Thermal decomposition of phosphonium salicylate and phosphonium benzoate ionic liquids*, J. Mol. Liq. **352**, 118700 (2022).

[6] G. F. L. Pereira, R. G. Pereira, M. Salanne, and L. J. A. Siqueira, *Molecular dynamics simulations of ether-modified phosphonium ionic liquid confined in between planar and porous graphene electrode models*, J. Phys. Chem. C **123**, 10816–10825 (2019).

[7] K. Oster, P. Goodrich, J. Jacquemin, C. Hardacre, A. Ribeiro, and A. Elsinawi, *A new insight into pure and water-saturated quaternary phosphonium-based carboxylate ionic liquids: Density, heat capacity, ionic conductivity, thermogravimetric analysis, thermal conductivity and viscosity*, J. Chem. Thermodyn. **121**, 97–111 (2018).

[8] Z. Lei, B. Chen, Y.-M. Koo, and D. R. MacFarlane. *Introduction: ionic liquids*, (2017).

[9] S. K. Singh and A. W. Savoy, *Ionic liquids synthesis and applications: An overview*, J. Mol. Liq. **297**, 112038 (2020).

[10] M. D. Joshi and J. L. Anderson, *Recent advances of ionic liquids in separation science and mass spectrometry*, RSC Adv. **2**, 5470–5484 (2012).

[11] J. P. Hallett and T. Welton, *Room-temperature ionic liquids: solvents for synthesis and catalysis. 2*, Chemical reviews **111**, 3508–3576 (2011).

[12] Y. Zhou and J. Qu, *Ionic liquids as lubricant additives: a review*, ACS Appl. Mater. Interfaces **9**, 3209–3222 (2017).

[13] A. K. Kasar, C. J. Reeves, and P. L. Menezes, *The effect of particulate additive mixtures on the tribological performance of phosphonium-based ionic liquid lubricants*, Tribol. Int. **165**, 107300 (2022).

[14] M. Sivapragasam, J. R. Jaganathan, J.-M. Levêque, M. Moniruzzaman, and M. A. Mutalib, *Microbial biocompatibility of phosphonium-and ammonium-based ionic liquids*, J. Mol. Liq. **273**, 107–115 (2019).

[15] T. P. T. Pham, C.-W. Cho, and Y.-S. Yun, *Environmental fate and toxicity of ionic liquids: a review*, Water research **44**, 352–372 (2010).

[16] K. N. Marsh, J. A. Boxall, and R. Lichtenthaler, *Room temperature ionic liquids and their mixtures—a review*, Fluid phase equilibria **219**, 93–98 (2004).

[17] A. J. Greer, J. Jacquemin, and C. Hardacre, *Industrial applications of ionic liquids*, Molecules **25**, 5207 (2020).

[18] A. Hajipour and F. Rafiee, *Basic ionic liquids. A short review*, Journal of the Iranian Chemical Society **6**, 647–678 (2009).

[19] S. K. Singh, *Solubility of lignin and chitin in ionic liquids and their biomedical applications*, International journal of biological macromolecules **132**, 265–277 (2019).

[20] M. H. Rahman, A. Khajeh, P. Panwar, M. Patel, A. Martini, and P. L. Menezes, *Recent progress on phosphonium-based room temperature ionic liquids: Synthesis, properties, tribological performances and applications*, Tribol. Int. **167**, 107331 (2022).

[21] C. J. Reeves, A. Siddaiah, and P. L. Menezes, *Tribological study of imidazolium and phosphonium ionic liquid-based lubricants as additives in carboxylic acid-based natural oil: advancements in environmentally friendly lubricants*, J. Cleaner Prod. **176**, 241–250 (2018).

[22] J. Yang, Z. Zhou, Y. Liang, J. Tang, Y. Gao, J. Niu, H. Dong, R. Tang, G. Tang, and Y. Cao, *Sustainable Preparation of Microcapsules with Desirable Stability and Bioactivity Using Phosphonium Ionic Liquid as a Functional Additive*, ACS Sustainable Chem. Eng. **8**, 13440–13448 (2020).

[23] J. Singh, S. S. Chatha, and R. Bhatia, *Behaviour and applications of ionic liquids as lubricants in tribology: A review*, Materials Today: Proceedings (2021).

[24] C. Ye, W. Liu, Y. Chen, and L. Yu, *Room-temperature ionic liquids: a novel versatile lubricant*, Chemical Communications , 2244–2245 (2001).

[25] M.-D. Bermúdez, A.-E. Jiménez, J. Sanes, and F.-J. Carrión, *Ionic liquids as advanced lubricant fluids*, Molecules **14**, 2888–2908 (2009).

[26] I. Minami, *Ionic liquids in tribology*, Molecules **14**, 2286–2305 (2009).

[27] A. E. Somers, P. C. Howlett, D. R. MacFarlane, and M. Forsyth, *A review of ionic liquid lubricants*, Lubricants **1**, 3–21 (2013).

[28] T. Welton, *Ionic liquids: a brief history*, Biophys. Rev. **10**, 691–706 (2018).

[29] X. Liu, F. Zhou, Y. Liang, and W. Liu, *Tribological performance of phosphonium based ionic liquids for an aluminum-on-steel system and opinions on lubrication mechanism*, Wear **261**, 1174–1179 (2006).

[30] L. Weng, X. Liu, Y. Liang, and Q. Xue, *Effect of tetraalkylphosphonium based ionic liquids as lubricants on the tribological performance of a steel-on-steel system*, Tribol. Lett. **26**, 11–17 (2007).

[31] I. Minami, M. Kita, T. Kubo, H. Nanao, and S. Mori, *The tribological properties of ionic liquids composed of trifluorotris (pentafluoroethyl) phosphate as a hydrophobic anion*, Tribol. Lett. **30**, 215–223 (2008).

[32] I. Minami, T. Inada, R. Sasaki, and H. Nanao, *Tribo-chemistry of phosphonium-derived ionic liquids*, Tribol. Lett. **40**, 225–235 (2010).

[33] L. K. Scarbath-Evers, P. A. Hunt, B. Kirchner, D. R. MacFarlane, and S. Zahn, *Molecular features contributing to the lower viscosity of phosphonium ionic liquids compared to their ammonium analogues*, Phys. Chem. Chem. Phys. **17**, 20205–20216 (2015).

[34] P. K. Naik, S. Paul, and T. Banerjee, *Physiochemical properties and molecular dynamics simulations of phosphonium and ammonium based deep eutectic solvents*, J. Solution Chem. **48**, 1046–1065 (2019).

[35] I. Otero, E. R. Loépez, M. Reichelt, M. Villanueva, J. Salgado, and J. Fernaéndez, *Ionic liquids based on phosphonium cations as neat lubricants or lubricant additives for a steel/steel contact*, ACS Appl. Mater. Interfaces **6**, 13115–13128 (2014).

[36] K. J. Fraser and D. R. MacFarlane, *Phosphonium-based ionic liquids: an overview*, Aust. J. Chem. **62**, 309–321 (2009).

[37] C. Maton, N. De Vos, and C. V. Stevens, *Ionic liquid thermal stabilities: decomposition mechanisms and analysis tools*, Chem. Soc. Rev. **42**, 5963–5977 (2013).

[38] S. Khazalpour, M. Yarie, E. Kianpour, A. Amani, S. Asadabadi, J. Y. Seyf, M. Rezaeivala, S. Azizian, and M. A. Zolfigol, *Applications of phosphonium-based ionic liquids in chemical processes*, J. Iran. Chem. Soc. **17**, 1775–1917 (2020).

[39] B. Yu, D. G. Bansal, J. Qu, X. Sun, H. Luo, S. Dai, P. J. Blau, B. G. Bunting, G. Mordukhovich, and D. J. Smolenski, *Oil-miscible and non-corrosive phosphonium-based ionic liquids as candidate lubricant additives*, Wear **289**, 58–64 (2012).

[40] M. Cai, Q. Yu, W. Liu, and F. Zhou, *Ionic liquid lubricants: When chemistry meets tribology*, Chem. Soc. Rev. **49**, 7753–7818 (2020).

[41] R. R. Henriques and B. G. Soares, *Sepiolite modified with phosphonium ionic liquids as anticorrosive pigment for epoxy coatings*, Appl. Clay Sci. **200**, 105890 (2021).

[42] F. U. Shah, S. Glavatskih, D. R. MacFarlane, A. Somers, M. Forsyth, and O. N. Antzutkin, *Novel halogen-free chelated orthoborate–phosphonium ionic liquids: synthesis and tribophysical properties*, Phys. Chem. Chem. Phys. **13**, 12865–12873 (2011).

[43] V. Totolin, I. Minami, C. Gabler, and N. Dörr, *Halogen-free borate ionic liquids as novel lubricants for tribological applications*, Tribol. Int. **67**, 191–198 (2013).

[44] L. Zhu, J. Dong, Y. Ma, Y. Jia, C. Peng, W. Li, M. Zhang, K. Gong, and X. Wang, *Synthesis and investigation of halogen-free phosphonium-based ionic liquids for lubrication applications*, Tribol. Trans. **62**, 943–954 (2019).

[45] M. Sydow, M. Owsianiak, G. Framski, M. Woźniak-Karczewska, A. Piotrowska-Cyplik, Ł. Ławniczak, A. Szulc, A. Zgoła-Grześkowiak, H. J. Heipieper, and Ł. Chrzanowski, *Biodiversity of soil bacteria exposed to sub-lethal concentrations of phosphonium-based ionic liquids: Effects of toxicity and biodegradation*, Ecotoxicol. Environ. Saf. **147**, 157–164 (2018).

[46] P. Oulego, D. Blanco, D. Ramos, J. Viesca, M. Díaz, and A. H. Battez, *Environmental properties of phosphonium, imidazolium and ammonium cation-based ionic liquids as potential lubricant additives*, J. Mol. Liq. **272**, 937–947 (2018).

[47] P. Rohlmann, B. Munavirov, I. Furó, O. Antzutkin, M. W. Rutland, and S. Glavatskih, *Non-halogenated ionic liquid dramatically enhances tribological performance of biodegradable oils*, Front. Chem. **7**, 98 (2019).

[48] S. Nazir, M. Khawar Rauf, M. Ebihara, and S. Hameed, *[4-(Methoxycarbonyl) benzyl] triphenylphosphonium bromide hemihydrate*, Acta Crystallogr., Sect. E: Struct. Rep. Online **64**, o423–o423 (2008).

[49] M. T. Dove, *An introduction to atomistic simulation methods*, Seminarios de la SEM **4**, 7–37 (2008).

[50] R. W. Balluffi, S. M. Allen, and W. C. Carter, *Kinetics of materials*, John Wiley & Sons (2005).

[51] M. P. Allen and D. J. Tildesley, *Computer simulation of liquids*, Oxford university press, Oxford (2017).

[52] T. Yan, C. J. Burnham, M. G. Del Pópolo, and G. A. Voth, *Molecular dynamics simulation of ionic liquids: The effect of electronic polarizability*, J. Phys. Chem. B **108**, 11877–11881 (2004).

[53] O. Borodin, *Polarizable force field development and molecular dynamics simulations of ionic liquids*, J. Phys. Chem. B **113**, 11463–11478 (2009).

[54] O. N. Starovoytov, H. Torabifard, and G. A. Cisneros, *Development of AMOEBA force field for 1, 3-dimethylimidazolium based ionic liquids*, J. Phys. Chem. B **118**, 7156–7166 (2014).

[55] D. Bedrov, J.-P. Piquemal, O. Borodin, A. D. MacKerell Jr, B. Roux, and C. Shroder, *Molecular dynamics simulations of ionic liquids and electrolytes using polarizable force fields*, Chem. Rev. **119**, 7940–7995 (2019).

[56] K. Goloviznina, J. N. Canongia Lopes, M. Costa Gomes, and A. A. Pádua, *Transferable, polarizable force field for ionic liquids*, J. Chem. Theory Comput. **15**, 5858–5871 (2019).

[57] E. A. Vázquez-Montelongo, J. E. Vázquez-Cervantes, and G. A. Cisneros, *Current Status of AMOEBA–IL: A Multipolar/Polarizable Force Field for Ionic Liquids*, Int. J. Mol. Sci. **21**, 697 (2020).

[58] J. N. Canongia Lopes, J. Deschamps, and A. A. Pádua, *Modeling ionic liquids using a systematic all-atom force field*, J. Phys. Chem. B **108**, 2038–2047 (2004).

[59] J. N. Canongia Lopes and A. A. Pádua, *Molecular force field for ionic liquids composed of triflate or bistriflylimide anions*, J. Phys. Chem. B **108**, 16893–16898 (2004).

[60] J. N. Canongia Lopes and A. A. Pádua, *Molecular force field for ionic liquids III: Imidazolium, pyridinium, and phosphonium cations; chloride, bromide, and dicyanamide anions*, J. Phys. Chem. B **110**, 19586–19592 (2006).

[61] J. N. Canongia Lopes, A. A. Pádua, and K. Shimizu, *Molecular force field for ionic liquids IV: Trialkylimidazolium and alkoxycarbonyl-imidazolium cations; alkylsulfonate and alkylsulfate anions*, J. Phys. Chem. B **112**, 5039–5046 (2008).

[62] K. Shimizu, D. Almantariotis, M. F. C. Gomes, A. A. Padua, and J. N. Canongia Lopes, *Molecular force field for ionic liquids V: Hydroxyethylimidazolium, dimethoxy-2-methylimidazolium, and fluoroalkylimidazolium cations and bis (fluorosulfonyl) amide, perfluoroalkanesulfonylamide, and fluoroalkylfluorophosphate anions*, J. Phys. Chem. B **114**, 3592–3600 (2010).

[63] J. N. C. Lopes and A. A. Pádua, *CL&P: A generic and systematic force field for ionic liquids modeling*, Theor. Chem. Acc. **131**, 1–11 (2012).

[64] M. Xia, Z. Chai, and D. Wang, *Polarizable and non-polarizable force field representations of ferric cation and validations*, J. Phys. Chem. B **121**, 5718–5729 (2017).

[65] W. D. Cornell, P. Cieplak, C. I. Bayly, I. R. Gould, K. M. Merz, D. M. Ferguson, D. C. Spellmeyer, T. Fox, J. W. Caldwell, and P. A. Kollman, *A second generation force field for the simulation of proteins, nucleic acids, and organic molecules*, J. Am. Chem. Soc. **117**, 5179–5197 (1995).

[66] W. L. Jorgensen, D. S. Maxwell, and J. Tirado-Rives, *Development and testing of the OPLS all-atom force field on conformational energetics and properties of organic liquids*, J. Am. Chem. Soc. **118**, 11225–11236 (1996).

[67] Z. Liu, S. Huang, and W. Wang, *A refined force field for molecular simulation of imidazolium-based ionic liquids*, J. Phys. Chem. B **108**, 12978–12989 (2004).

[68] X. Wu, Z. Liu, S. Huang, and W. Wang, *Molecular dynamics simulation of room-temperature ionic liquid mixture of [bmim][BF4] and acetonitrile by a refined force field*, Phys. Chem. Chem. Phys. **7**, 2771–2779 (2005).

[69] G. Zhou, X. Liu, S. Zhang, G. Yu, and H. He, *A force field for molecular simulation of tetrabutylphosphonium amino acid ionic liquids*, J. Phys. Chem. B **111**, 7078–7084 (2007).

[70] H. Wu, J. K. Shah, C. M. Tenney, T. W. Rosch, and E. J. Maginn, *Structure and dynamics of neat and CO2-reacted ionic liquid tetrabutylphosphonium 2-cyanopyrrolide*, Ind. Eng. Chem. Res. **50**, 8983–8993 (2011).

[71] Q. Parker, R. G. Bell, and N. H. de Leeuw, *Structural and dynamical properties of ionic liquids: a molecular dynamics study employing DL_POLY 4*, Mol. Simul. **47**, 152–160 (2021).

[72] Q. R. Sheridan, W. F. Schneider, and E. J. Maginn, *Role of molecular modeling in the development of CO2–reactive ionic liquids*, Chem. Rev. **118**, 5242–5260 (2018).

[73] S. V. Sambasivarao and O. Acevedo, *Development of OPLS-AA force field parameters for 68 unique ionic liquids*, J. Chem. Theory Comput. **5**, 1038–1050 (2009).

[74] B. Doherty, X. Zhong, S. Gathiaka, B. Li, and O. Acevedo, *Revisiting OPLS force field parameters for ionic liquid simulations*, J. Chem. Theory Comput. **13**, 6131–6145 (2017).

[75] F. Dommert and C. Holm, *Refining classical force fields for ionic liquids: theory and application to [MMIM][Cl]*, Phys. Chem. Chem. Phys. **15**, 2037–2049 (2013).

[76] I. V. Voroshylova and V. V. Chaban, *Atomistic force field for pyridinium-based ionic liquids: reliable transport properties*, J. Phys. Chem. B **118**, 10716–10724 (2014).

[77] V. V. Chaban and I. V. Voroshylova, *Systematic refinement of canongia Lopes–Pádua force field for pyrrolidinium-based ionic liquids*, J. Phys. Chem. B **119**, 6242–6249 (2015).

[78] T. Köddermann, D. Paschek, and R. Ludwig, *Molecular dynamic simulations of ionic liquids: A reliable description of structure, thermodynamics and dynamics*, ChemPhysChem **8**, 2464–2470 (2007).

[79] N. Vergadou, E. Androulaki, J.-R. Hill, and I. G. Economou, *Molecular simulations of imidazolium-based tricyanomethanide ionic liquids using an optimized classical force field*, Phys. Chem. Chem. Phys. **18**, 6850–6860 (2016).

[80] X. Liu, G. Zhou, S. Zhang, and G. Yu, *Molecular simulations of phosphonium-based ionic liquid*, Mol. Simul. **36**, 79–86 (2010).

[81] Y.-L. Wang, S. Sarman, L. Kloo, O. N. Antzutkin, S. Glavatskih, and A. Laaksonen, *Solvation structures of water in trihexyltetradecylphosphonium-orthoborate ionic liquids*, J. Chem. Phys. **145**, 064507 (2016).

[82] S. Sarman, Y.-L. Wang, P. Rohlmann, S. Glavatskih, and A. Laaksonen, *Rheology of phosphonium ionic liquids: a molecular dynamics and experimental study*, Phys. Chem. Chem. Phys. **20**, 10193–10203 (2018).

[83] A. C. Van Duin, S. Dasgupta, F. Lorant, and W. A. Goddard, *ReaxFF: a reactive force field for hydrocarbons*, J. Phys. Chem. A **105**, 9396–9409 (2001).

[84] A. Khajeh, X. Hu, K. Mohammadtabar, Y. K. Shin, A. C. Van Duin, S. Berkebile, and A. Martini, *Statistical analysis of tri-cresyl phosphate conversion on an iron oxide surface using reactive molecular dynamics simulations*, The Journal of Physical Chemistry C **123**, 12886–12893 (2019).

[85] A. Khajeh, F. H. Bhuiyan, J.-E. Mogonye, R. A. Pesce-Rodriguez, S. Berkebile, and A. Martini, *Thermal Decomposition of Tricresyl Phosphate on Ferrous Surfaces*, J. Phys. Chem. C **125**, 5076–5087 (2021).

[86] S. Tsuzuki, H. Tokuda, K. Hayamizu, and M. Watanabe, *Magnitude and directionality of interaction in ion pairs of ionic liquids: Relationship with ionic conductivity*, J. Phys. Chem. B **109**, 16474–16481 (2005).

[87] L. Maschio, B. Civalleri, P. Ugliengo, and A. Gavezzotti, *Intermolecular interaction energies in molecular crystals: comparison and agreement of localized Møller–Plesset 2, dispersion-corrected density functional, and classical empirical two-body calculations*, J. Phys. Chem. A **115**, 11179–11186 (2011).

[88] L. Gontrani, O. Russina, F. Lo Celso, R. Caminiti, G. Annat, and A. Triolo, *Liquid structure of trihexyltetradecylphosphonium chloride at ambient temperature: An x-ray scattering and simulation study*, J. Phys. Chem. B **113**, 9235–9240 (2009).

[89] V. L. Martins, N. Sanchez-Ramirez, M. C. Ribeiro, and R. M. Torresi, *Two phosphonium ionic liquids with high Li+ transport number*, Phys. Chem. Chem. Phys. **17**, 23041–23051 (2015).

[90] A. R. Shaikh, M. Ashraf, T. AlMayef, M. Chawla, A. Poater, and L. Cavallo, *Amino acid ionic liquids as potential candidates for CO2 capture: combined density functional theory and molecular dynamics simulations*, Chem. Phys. Lett. **745**, 137239 (2020).

[91] Y. Zhao, L. Tian, Y. Pei, H. Wang, and J. Wang, *Effect of anionic structure on the LCST phase behavior of phosphonium ionic liquids in water*, Ind. Eng. Chem. Res. **57**, 12935–12941 (2018).

[92] X. Zhang, F. Huo, X. Liu, K. Dong, H. He, X. Yao, and S. Zhang, *Influence of microstructure and interaction on viscosity of ionic liquids*, Ind. Eng. Chem. Res. **54**, 3505–3514 (2015).

[93] A. Laaksonen, P. Kusalik, and I. Svishchev, *Three-dimensional structure in water-methanol mixtures*, J. Phys. Chem. A **101**, 5910–5918 (1997).

[94] K. Kulińska, T. Kuliński, A. Lyubartsev, A. Laaksonen, and R. W. Adamiak, *Spatial distribution functions as a tool in the analysis of ribonucleic acids hydration—molecular dynamics studies*, Comput. Chem. **24**, 451–457 (2000).

[95] P. G. Kusalik and I. M. Svishchev, *The spatial structure in liquid water*, Science **265**, 1219–1221 (1994).

[96] K. Dong and S. Zhang, *Hydrogen bonds: a structural insight into ionic liquids*, Chem. - Eur. J. **18**, 2748–2761 (2012).

[97] J. Luo, O. Conrad, and I. F. Vankelecom, *Physicochemical properties of phosphonium-based and ammonium-based protic ionic liquids*, J. Mater. Chem. **22**, 20574–20579 (2012).

[98] E. Guardia, J. Martí, L. García-Tarrés, and D. Laria, *A molecular dynamics simulation study of hydrogen bonding in aqueous ionic solutions*, J. Mol. Liq. **117**, 63–67 (2005).

[99] E. C. Fitch, *Proactive maintenance for mechanical systems*, Elsevier, Stillwater (2013).

[100] G. Quercia, R. Belisario, and R. Rengifo, *Reduction of erosion rate by particle size distribution (PSD) modification of hematite as weighting agent for oil based drilling fluids*, Wear **266**, 1229–1236 (2009).

[101] X. Gao, J. Fang, and H. Wang, *Sampling the isothermal-isobaric ensemble by Langevin dynamics*, J. Chem. Phys. **144**, 124113 (2016).

[102] H. Wu and E. J. Maginn, *Water solubility and dynamics of CO2 capture ionic liquids having aprotic heterocyclic anions*, Fluid Phase Equilib. **368**, 72–79 (2014).

[103] Y.-L. Wang, M. R. Shimpi, S. Sarman, O. N. Antzutkin, S. Glavatskih, L. Kloo, and A. Laaksonen, *Atomistic insight into tetraalkylphosphonium bis (oxalato) borate ionic liquid/water mixtures. 2. volumetric and dynamic properties*, J. Phys. Chem. B **120**, 7446–7455 (2016).

[104] S. S. Venkatesan, M. M. Huda, and N. Rai, *Molecular insights into ionic liquid/aqueous interface of phosphonium based phase-separable ionic liquids*, AIP Adv. **9**, 045115 (2019).

[105] S. Sharma, A. Gupta, D. Dhabal, and H. K. Kashyap, *Pressure-dependent morphology of trihexyl (tetradecyl) phosphonium ionic liquids: A molecular dynamics study*, J. Chem. Phys. **145**, 134506 (2016).

[106] A. Mondal and A. P. Sunda, *Molecular dynamics simulations of ammonium/phosphonium-based protic ionic liquids: influence of alkyl to aryl group*, Phys. Chem. Chem. Phys. **20**, 19268–19275 (2018).

[107] M. R. Shimpi, P. Rohlmann, F. U. Shah, S. Glavatskih, and O. N. Antzutkin, *Transition anionic complex in trihexyl (tetradecyl) phosphonium-bis (oxalato) borate ionic liquid–revisited*, Phys. Chem. Chem. Phys. **23**, 6190–6203 (2021).

[108] S. Kasahara, E. Kamio, and H. Matsuyama, *Improvements in the CO2 permeation selectivities of amino acid ionic liquid-based facilitated transport membranes by controlling their gas absorption properties*, J. Membr. Sci. **454**, 155–162 (2014).

[109] M. Blahušiak and Š. Schlosser, *Physical properties of phosphonium ionic liquid and its mixtures with dodecane and water*, J. Chem. Thermodyn. **72**, 54–64 (2014).

[110] J. Marták and S. Schlosser, *Density, viscosity, and structure of equilibrium solvent phases in butyric acid extraction by phosphonium ionic liquid*, J. Chem. Eng. Data **62**, 3025–3035 (2017).

[111] S. Seo, M. A. DeSilva, H. Xia, and J. F. Brennecke, *Effect of cation on physical properties and CO2 solubility for phosphonium-based ionic liquids with 2-cyanopyrrolide anions*, J. Phys. Chem. B **119**, 11807–11814 (2015).

[112] C. Kolbeck, J. Lehmann, K. Lovelock, T. Cremer, N. Paape, P. Wasserscheid, A. Froba, F. Maier, and H.-P. Steinruck, *Density and surface tension of ionic liquids*, J. Phys. Chem. B **114**, 17025–17036 (2010).

[113] M. Tariq, P. Forte, M. C. Gomes, J. C. Lopes, and L. Rebelo, *Densities and refractive indices of imidazolium-and phosphonium-based ionic liquids: Effect of temperature, alkyl chain length, and anion*, J. Chem. Thermodyn. **41**, 790–798 (2009).

[114] S. Seki, T. Kobayashi, Y. Kobayashi, K. Takei, H. Miyashiro, K. Hayamizu, S. Tsuzuki, T. Mitsugi, and Y. Umebayashi, *Effects of cation and anion on physical properties of room-temperature ionic liquids*, J. Mol. Liq. **152**, 9–13 (2010).

[115] M. Montalbán, C. Bolívar, F. G. Diaz Banos, and G. Víllora, *Effect of temperature, anion, and alkyl chain length on the density and refractive index of 1-alkyl-3-methylimidazolium-based ionic liquids*, J. Chem. Eng. Data **60**, 1986–1996 (2015).

[116] M. Ebrahimi and F. Moosavi, *The effects of temperature, alkyl chain length, and anion type on thermophysical properties of the imidazolium based amino acid ionic liquids*, J. Mol. Liq. **250**, 121–130 (2018).

[117] B. Hess, *Determining the shear viscosity of model liquids from molecular dynamics simulations*, J. Chem. Phys. **116**, 209–217 (2002).

[118] U. S. Ramasamy, M. Len, and A. Martini, *Correlating molecular structure to the behavior of linear styrene–butadiene viscosity modifiers*, Tribol. Lett. **65**, 1–8 (2017).

[119] M. Len, U. S. Ramasamy, S. Lichter, and A. Martini, *Thickening mechanisms of polyisobutylene in polyalphaolefin*, Tribol. Lett. **66**, 1–9 (2018).

[120] P. Panwar, P. Michael, M. Devlin, and A. Martini, *Critical Shear Rate of Polymer-Enhanced Hydraulic Fluids*, Lubricants **8**, 102 (2020).

[121] D. Mathas, W. Holweger, M. Wolf, C. Bohnert, V. Bakolas, J. Procelewska, L. Wang, S. Bair, and C.-K. Skylaris, *Evaluation of methods for viscosity simulations of lubricants at different temperatures and pressures: a case study on PAO-2*, Tribol. Trans. **64**, 1138–1148 (2021).

[122] A. Noda, K. Hayamizu, and M. Watanabe, *Pulsed-gradient spin- echo 1H and 19F NMR ionic diffusion coefficient, viscosity, and ionic conductivity of non-chloroaluminate room-temperature ionic liquids*, J. Phys. Chem. B **105**, 4603–4610 (2001).

[123] M. H. Ghatee and M. Bahrami, *Emergence of innovative properties by replacement of nitrogen atom with phosphorus atom in quaternary ammonium ionic liquids: Insights from ab initio calculations and MD simulations*, Chem. Phys. **490**, 92–105 (2017).

[124] D. J Evans and G. P Morriss, *Statistical mechanics of nonequilbrium liquids*, ANU Press, Canberra (2007).

[125] A. Li, Z. Tian, T. Yan, D.-e. Jiang, and S. Dai, *Anion-functionalized task-specific ionic liquids: molecular origin of change in viscosity upon CO2 capture*, J. Phys. Chem. B **118**, 14880–14887 (2014).

[126] D. S. Firaha, A. V. Gibalova, and O. Holloczki, *Basic Phosphonium Ionic Liquids as Wittig Reagents*, ACS omega **2**, 2901–2911 (2017).

[127] W. C. Barnhill, J. Qu, H. Luo, H. M. Meyer III, C. Ma, M. Chi, and B. L. Papke, *Phosphonium-organophosphate ionic liquids as lubricant additives: effects of cation structure on physicochemical and tribological characteristics*, ACS Appl. Mater. Interfaces **6**, 22585–22593 (2014).

[128] D. Rauber, P. Zhang, V. Huch, T. Kraus, and R. Hempelmann, *Lamellar structures in fluorinated phosphonium ionic liquids: the roles of fluorination and chain length*, Phys. Chem. Chem. Phys. **19**, 27251–27258 (2017).

[129] T. Yamaguchi, *Shear Thinning and Nonlinear Structural Deformation of Ionic Liquids with Long Alkyl Chains Studied by Molecular Dynamics Simulation*, J. Phys. Chem. B **123**, 6260–6265 (2019).

[130] Y. Ma, Y. Liu, H. Su, L. Wang, and J. Zhang, *Relationship between hydrogen bond and viscosity for a series of pyridinium ionic liquids: Molecular dynamics and quantum chemistry*, J. Mol. Liq. **255**, 176–184 (2018).

[131] E. Santos, J. Albo, C. Daniel, C. Portugal, J. Crespo, and A. Irabien, *Permeability modulation of Supported Magnetic Ionic Liquid Membranes (SMILMs) by an external magnetic field*, Journal of membrane science **430**, 56–61 (2013).

[132] T. C. Lourenço, Y. Zhang, L. T. Costa, and E. J. Maginn, *A molecular dynamics study of lithium-containing aprotic heterocyclic ionic liquid electrolytes*, J. Chem. Phys. **148**, 193834 (2018).

[133] Q. R. Sheridan, W. F. Schneider, and E. J. Maginn, *Anion dependent dynamics and water solubility explained by hydrogen bonding interactions in mixtures of water and aprotic heterocyclic anion ionic liquids*, J. Phys. Chem. B **120**, 12679–12686 (2016).

[134] W. Huang, L. Kong, and X. Wang, *Electrical sliding friction lubricated with ionic liquids*, Tribol. Lett. **65**, 1–6 (2017).

[135] A. Gonda, R. Capan, D. Bechev, and B. Sauer, *The influence of lubricant conductivity on bearing currents in the case of rolling bearing greases*, Lubricants **7**, 108 (2019).

[136] Y. Chen, S. Jha, A. Raut, W. Zhang, and H. Liang, *Performance characteristics of lubricants in electric and hybrid vehicles: a review of current and future needs*, Front. Mech. Eng. **6**, 82 (2020).

[137] M. Harada, A. Yamanaka, M. Tanigaki, and Y. Tada, *Mass and size effects on the transport properties of molten salts*, J. Chem. Phys. **76**, 1550–1556 (1982).

[138] H. Basouli, F. Mozaffari, and H. Eslami, *Atomistic insights into structure, ion-pairing and ionic conductivity of 1-ethyl-3-methylimidazolium methylsulfate [Emim][MeSO4] ionic liquid from molecular dynamics simulation*, J. Mol. Liq. **331**, 115803 (2021).

[139] J.-P. Hansen and I. R. McDonald, *Theory of simple liquids: with applications to soft matter*, Academic press (2013).

[140] Y. Mao and Y. Zhang, *Thermal conductivity, shear viscosity and specific heat of rigid water models*, Chem. Phys. Lett. **542**, 37–41 (2012).

[141] R. L. Gardas, R. Ge, P. Goodrich, C. Hardacre, A. Hussain, and D. W. Rooney, *Thermophysical properties of amino acid-based ionic liquids*, J. Chem. Eng. Data **55**, 1505–1515 (2010).

[142] A. F. Ferreira, P. N. Simões, and A. G. Ferreira, *Quaternary phosphonium-based ionic liquids: Thermal stability and heat capacity of the liquid phase*, J. Chem. Thermodyn. **45**, 16–27 (2012).

[143] K. Oster, J. Jacquemin, C. Hardacre, A. Ribeiro, and A. Elsinawi, *Further development of the predictive models for physical properties of pure ionic liquids: Thermal conductivity and heat capacity*, J. Chem. Thermodyn. **118**, 1–15 (2018).

[144] L. Zhai, Q. Zhong, C. He, and J. Wang, *Hydroxyl ammonium ionic liquids synthesized by water-bath microwave: Synthesis and desulfurization*, J. Hazard. Mater. **177**, 807–813 (2010).

[145] G. Adamová, R. L. Gardas, L. P. N. Rebelo, A. J. Robertson, and K. R. Seddon, *Alkyltrioctylphosphonium chloride ionic liquids: synthesis and physicochemical properties*, Dalton Trans. **40**, 12750–12764 (2011).

[146] M. Montanino, F. Alessandrini, S. Passerini, and G. B. Appetecchi, *Water-based synthesis of hydrophobic ionic liquids for high-energy electrochemical devices*, Electrochim. Acta **96**, 124–133 (2013).

[147] C. Verma, E. E. Ebenso, and M. Quraishi, *Transition metal nanoparticles in ionic liquids: Synthesis and stabilization*, J. Mol. Liq. **276**, 826–849 (2019).

[148] R. Dong, Q. Yu, Y. Bai, Y. Wu, Z. Ma, J. Zhang, C. Zhang, B. Yu, F. Zhou, W. Liu, et al., *Towards superior lubricity and anticorrosion performances of proton-type ionic liquids additives for water-based lubricating fluids*, Chem. Eng. J. **383**, 123201 (2020).

[149] M. C. Kroon, W. Buijs, C. J. Peters, and G.-J. Witkamp, *Quantum chemical aided prediction of the thermal decomposition mechanisms and temperatures of ionic liquids*, Thermochim. Acta **465**, 40–47 (2007).

[150] M. Golets, M. Shimpi, Y.-L. Wang, O. Antzutkin, S. Glavatskih, and A. Laaksonen, *Understanding the thermal decomposition mechanism of a halogen-free chelated orthoborate-based ionic liquid: a combined computational and experimental study*, Phys. Chem. Chem. Phys. **18**, 22458–22466 (2016).

[151] Z. Sun, J. Pan, J. Guo, and F. Yan, *The alkaline stability of anion exchange membrane for fuel cell applications: the effects of alkaline media*, Adv. Sci. **5**, 1800065 (2018).

[152] K. Thasneema, M. S. Thayyil, T. Rosalin, K. Elyas, T. Dipin, P. K. Sahu, N. K. Kumar, V. Saheer, M. Messali, and T. B. Hadda, *Thermal and spectroscopic investigations on three phosphonium based ionic liquids for industrial and biological applications*, J. Mol. Liq. **307**, 112960 (2020).

[153] T. P. Senftle, S. Hong, M. M. Islam, S. B. Kylasa, Y. Zheng, Y. K. Shin, C. Junkermeier, R. Engel-Herbert, M. J. Janik, H. M. Aktulga, T. Verstraelen, A. Grama, and A. C. T. van Duin, *The ReaxFF reactive force-field: development, applications and future directions*, npj Comput. Mater. **2**, 15011 (2016).

[154] A. Martini, S. J. Eder, and N. Dörr, *Tribochemistry: A review of reactive molecular dynamics simulations*, Lubricants **8**, 44 (2020).

[155] S. Han, X. Li, L. Guo, H. Sun, M. Zheng, and W. Ge, *Refining fuel composition of RP-3 chemical surrogate models by reactive molecular dynamics and machine learning*, Energy & Fuels **34**, 11381–11394 (2020).

[156] M. Gao, X. Li, and L. Guo, *Pyrolysis simulations of Fugu coal by large-scale ReaxFF molecular dynamics*, Fuel Process. Technol. **178**, 197–205 (2018).

[157] L. Xin, C. Liu, Y. Liu, E. Huo, Q. Li, X. Wang, and Q. Cheng, *Thermal decomposition mechanism of some hydrocarbons by ReaxFF-based molecular dynamics and density functional theory study*, Fuel **275**, 117885 (2020).

[158] K. Chenoweth, S. Cheung, A. C. Van Duin, W. A. Goddard, and E. M. Kober, *Simulations on the thermal decomposition of a poly (dimethylsiloxane) polymer using the ReaxFF reactive force field*, J. Am. Chem. Soc. **127**, 7192–7202 (2005).

[159] Y. Liu, J. Hu, H. Hou, and B. Wang, *Development and application of a ReaxFF reactive force field for molecular dynamics of perfluorinatedketones thermal decomposition*, Chem. Phys. **538**, 110888 (2020).

[160] E. Huo, C. Liu, X. Xu, and C. Dang, *A ReaxFF-based molecular dynamics study of the pyrolysis mechanism of HFO-1336mzz(Z)*, International Journal of Refrigeration **83**, 118–130 (2017).

[161] Y. Cao, C. Liu, H. Zhang, X. Xu, and Q. Li, *Thermal decomposition of HFO-1234yf through ReaxFF molecular dynamics simulation*, Appl. Therm. Eng. **126**, 330–338 (2017).

[162] R. Lyu, Z. Huang, H. Deng, Y. Wei, C. Mou, and L. Wang, *Anatomies for the thermal decomposition behavior and product rule of 5,5-dinitro-2H,2H-3,3-bi-1,2,4-triazole*, RSC Adv. **11**, 40182–40192 (2021).

[163] G. Lan, J. Li, G. Zhang, J. Ruan, Z. Lu, S. Jin, D. Cao, and J. Wang, *Thermal decomposition mechanism study of 3-nitro-1, 2, 4-triazol-5-one (NTO): Combined TG-FTIR-MS techniques and ReaxFF reactive molecular dynamics simulations*, Fuel **295**, 120655 (2021).

[164] J. P. Ewen, C. A. Latorre, C. Gattinoni, A. Khajeh, J. D. Moore, J. E. Remias, A. Martini, and D. Dini, *Substituent Effects on the Thermal Decomposition of Phosphate Esters on Ferrous Surfaces*, J. Phys. Chem. C **124**, 9852–9865 (2020).

[165] A. C. Mendonca, A. A. Padua, and P. Malfreyt, *Nonequilibrium molecular simulations of new ionic lubricants at metallic surfaces: prediction of the friction*, J. Chem. Theory Comput. **9**, 1600–1610 (2013).

[166] K. Pivnic, F. Bresme, A. A. Kornyshev, and M. Urbakh, *Electrotunable Friction in Diluted Room Temperature Ionic Liquids: Implications for Nanotribology*, ACS Appl. Nano Mater. **3**, 10708–10719 (2020).

[167] N. Voeltzel, N. Fillot, P. Vergne, and L. Joly, *Orders of magnitude changes in the friction of an ionic liquid on carbonaceous surfaces*, J. Phys. Chem. C **122**, 2145–2154 (2018).

[168] N. Voeltzel, A. Giuliani, N. Fillot, P. Vergne, and L. Joly, *Nanolubrication by ionic liquids: molecular dynamics simulations reveal an anomalous effective rheology*, Phys. Chem. Chem. Phys. **17**, 23226–23235 (2015).

[169] O. Y. Fajardo, F. Bresme, A. A. Kornyshev, and M. Urbakh, *Water in ionic liquid lubricants: friend and foe*, ACS nano **11**, 6825–6831 (2017).

[170] M. Bahrami, M. H. Ghatee, and S. F. Ayatollahi, *Simulation of wetting and interfacial behavior of quaternary ammonium and phosphonium ionic liquid nanodroplets over face-centered cubic metal surfaces*, J. Phys. Chem. B **124**, 2835–2847 (2020).

[171] Y.-L. Wang, M. Golets, B. Li, S. Sarman, and A. Laaksonen, *Interfacial structures of trihexyltetradecylphosphonium-bis (mandelato) borate ionic liquid confined between gold electrodes*, ACS Appl. Mater. Interfaces **9**, 4976–4987 (2017).

[172] J. S. Alexander, C. Maxwell, J. Pencer, and M. Saoudi, *Equilibrium Molecular Dynamics Calculations of Thermal Conductivity: A "how-to" for the Beginners*, CNL Nuclear Review **9**, 11–25 (2020).

[173] F. Müller-Plathe, *A simple nonequilibrium molecular dynamics method for calculating the thermal conductivity*, J. Chem. Phys. **106**, 6082–6085 (1997).

[174] M. Salanne, D. Marrocchelli, C. Merlet, N. Ohtori, and P. A. Madden, *Thermal conductivity of ionic systems from equilibrium molecular dynamics*, J. Phys.: Condens. Matter **23**, 102101 (2011).

[175] Y. Ishii, K. Sato, M. Salanne, P. A. Madden, and N. Ohtori, *Thermal conductivity of molten alkali metal fluorides (LiF, NaF, KF) and their mixtures*, J. Phys. Chem. B **118**, 3385–3391 (2014).

[176] N. Rivera, A. García, A. Fernández-González, D. Blanco, R. González, and A. H. Battez, *Tribological behavior of three fatty acid ionic liquids in the lubrication of different material pairs*, J. Mol. Liq. **296**, 111858 (2019).

[177] O. Fajardo, F. Bresme, A. Kornyshev, and M. Urbakh, *Electrotunable lubricity with ionic liquid nanoscale films*, Sci. Rep. **5**, 1–7 (2015).

[178] O. Y. Fajardo, F. Bresme, A. A. Kornyshev, and M. Urbakh, *Electrotunable friction with ionic liquid lubricants: how important is the molecular structure of the ions?*, J. Phys. Chem. Lett. **6**, 3998–4004 (2015).

[179] A. Somers, P. Howlett, J. Sun, D. MacFarlane, and M. Forsyth, *Phosphonium ionic liquids as lubricants for aluminium-steel*, Tribology Des **66**, 273–283 (2010).

[180] A. E. Somers, S. M. Biddulph, P. C. Howlett, J. Sun, D. R. MacFarlane, and M. Forsyth, *A comparison of phosphorus and fluorine containing IL lubricants for steel on aluminium*, Physical Chemistry Chemical Physics **14**, 8224–8231 (2012).

[181] C. J. Reeves, A. Siddaiah, and P. L. Menezes, *Friction and wear behavior of environmentally friendly ionic liquids for sustainability of biolubricants*, Journal of Tribology **141** (2019).

[182] L. S. Dodda, I. Cabeza de Vaca, J. Tirado-Rives, and W. L. Jorgensen, *LigParGen web server: an automatic OPLS-AA parameter generator for organic ligands*, Nucleic Acids Res. **45**, W331–W336 (2017).

[183] S. Plimpton, *Fast parallel algorithms for short-range molecular dynamics*, J. Comput. Phys. **117**, 1–19 (1995).

[184] A. Stukowski, *Visualization and analysis of atomistic simulation data with OVITO–the Open Visualization Tool*, Modelling and simulation in materials science and engineering **18**, 015012 (2009).

[185] D. J. Evans and B. L. Holian, *The nose–hoover thermostat*, J. Comput. Phys. **83**, 4069–4074 (1985).

[186] W. G. Hoover, *Constant-pressure equations of motion*, Physical Review A **34**, 2499 (1986).

[187] Q. Spreiter and M. Walter, *Classical molecular dynamics simulation with the Velocity Verlet algorithm at strong external magnetic fields*, J. Comput. Phys. **152**, 102–119 (1999).

[188] Y. Li and G. J. Wang, *How to produce confidence intervals instead of confidence tricks: Representative sampling for molecular simulations of fluid self-diffusion under nanoscale confinement*, The Journal of Chemical Physics **156**, 114113 (2022).

[189] G. S. Girolami, *A simple" back of the envelope" method for estimating the densities and molecular volumes of liquids and solids*, Journal of Chemical Education **71**, 962 (1994).

[190] E. J. Maginn, R. A. Messerly, D. J. Carlson, D. R. Roe, and J. R. Elliot, *Best practices for computing transport properties 1. Self-diffusivity and viscosity from equilibrium molecular dynamics [article v1. 0]*, Living Journal of Computational Molecular Science **1**, 6324–6324 (2019).

[191] Y. Zhang, A. Otani, and E. J. Maginn, *Reliable viscosity calculation from equilibrium molecular dynamics simulations: A time decomposition method*, Journal of chemical theory and computation **11**, 3537–3546 (2015).

[192] S. Kim, P. A. Thiessen, E. E. Bolton, J. Chen, G. Fu, A. Gindulyte, L. Han, J. He, S. He, B. A. Shoemaker, et al., *PubChem substance and compound databases*, Nucleic acids research **44**, D1202–D1213 (2016).

[193] P. A. Hunt, C. R. Ashworth, and R. P. Matthews, *Hydrogen bonding in ionic liquids*, Chemical Society Reviews **44**, 1257–1288 (2015).

[194] A. Westerholt, M. Weschta, A. Bosmann, S. Tremmel, Y. Korth, M. Wolf, E. Schlucker, N. Wehrum, A. Lennert, M. Uerdingen, et al., *Halide-free synthesis and tribological performance of oil-miscible ammonium and phosphonium-based ionic liquids*, ACS Sustainable Chem. Eng. **3**, 797–808 (2015).

[195] D. Blanco, M. Bartolome, B. Ramajo, J. Viesca, R. Gonzalez, and A. Hernandez Battez, *Wetting properties of seven phosphonium cation-based ionic liquids*, Ind. Eng. Chem. Res. **55**, 9594–9602 (2016).

[196] T. Batchelor, J. Cunder, and A. Y. Fadeev, *Wetting study of imidazolium ionic liquids*, J. Colloid Interface Sci. **330**, 415–420 (2009).

[197] C. H. Pameijer, P.-O. Glantz, and A. von Fraunhofer. *Clinical and Technical Considerations of Luting Agents for Fixed Prosthodontics*, (2012).

[198] M. Kalin and M. Polajnar, *The effect of wetting and surface energy on the friction and slip in oil-lubricated contacts*, Tribol. Lett. **52**, 185–194 (2013).

[199] T. Liu, K. Wang, Y. Chen, S. Zhao, and Y. Han, *Dominant role of wettability in improving the specific capacitance*, Green Energy Environ. **4**, 171–179 (2019).

[200] S. Moldoveanu and V. David, *Selection of the HPLC method in chemical analysis*, Elsevier (2016).

[201] T. Uelzen and J. Müller, *Wettability enhancement by rough surfaces generated by thin film technology*, Thin Solid Films **434**, 311–315 (2003).

[202] L. Matczak, C. Johanning, E. Gil, H. Guo, T. W. Smith, M. Schertzer, and P. Iglesias, *Effect of cation nature on the lubricating and physicochemical properties of three ionic liquids*, Tribol. Int. **124**, 23–33 (2018).

[203] W. Zhang, S. Jiang, J. Sun, Z. Wu, T. Qin, and X. Xi, *Wettability of coal by room temperature ionic liquids*, Int. J. Coal Prep. Util. **41**, 418–427 (2021).

[204] G. Tiago, J. Restolho, A. Forte, R. Colaço, L. Branco, and B. Saramago, *Novel ionic liquids for interfacial and tribological applications*, Colloids Surf., A **472**, 1–8 (2015).

[205] G. V. Carrera, C. A. Afonso, and L. C. Branco, *Interfacial properties, densities, and contact angles of task specific ionic liquids*, J. Chem. Eng. Data **55**, 609–615 (2010).

[206] E. Cigno, C. Magagnoli, M. S. Pierce, and P. Iglesias, *Lubricating ability of two phosphonium-based ionic liquids as additives of a bio-oil for use in wind turbines gearboxes*, Wear **376**, 756–765 (2017).

[207] J. Grace, S. Vysochanska, J. Lodge, and P. Iglesias, *Ionic liquids as additives of coffee bean oil in steel-steel contacts*, Lubricants **3**, 637–649 (2015).

[208] X. Zhao, Y. Zhu, C. Zhang, J. Lei, Y. Ma, and F. Du, *Positive charge pesticide nanoemulsions prepared by the phase inversion composition method with ionic liquids*, RSC advances **7**, 48586–48596 (2017).

[209] S. Malali and M. Foroutan, *Study of wetting behavior of BMIM+/PF6–ionic liquid on TiO2 (110) surface by molecular dynamics simulation*, J. Phys. Chem. C **121**, 11226–11233 (2017).

[210] E. Bordes, L. Douce, E. L. Quitevis, A. A. Pádua, and M. Costa Gomes, *Ionic liquids at the surface of graphite: Wettability and structure*, J. Chem. Phys. **148**, 193840 (2018).

[211] S. Bhattacharjee and S. Khan, *Effect of alkyl chain length on the wetting behavior of imidazolium based ionic liquids: A molecular dynamics study*, Fluid Phase Equilib. **501**, 112253 (2019).

[212] S. Bhattacharjee and S. Khan, *The wetting behavior of aqueous imidazolium based ionic liquids: a molecular dynamics study*, Phys. Chem. Chem. Phys. **22**, 8595–8605 (2020).

[213] H. Atkinson, J. E. Bara, and C. H. Turner, *Molecular-level analysis of the wetting behavior of imidazolium-based ionic liquids on bismuth telluride surfaces*, Chem. Eng. Sci. **211**, 115270 (2020).

[214] H. J. Castejon, T. J. Wynn, and Z. M. Marcin, *Wetting and tribological properties of ionic liquids*, J. Phys. Chem. B **118**, 3661–3668 (2014).

[215] H. Liu and L. Jiang, *Wettability by ionic liquids*, Small **12**, 9–15 (2016).

[216] M. Meunier. *Introduction to materials studio*. In *EPJ Web of Conferences*, volume 30, page 04001. EDP Sciences, (2012).

[217] A. Jain, S. P. Ong, G. Hautier, W. Chen, W. D. Richards, S. Dacek, S. Cholia, D. Gunter, D. Skinner, G. Ceder, et al., *Commentary: The Materials Project: A materials genome approach to accelerating materials innovation*, APL materials **1**, 011002 (2013).

[218] C. Maghfiroh, A. Arkundato, W. Maulina, et al. *Parameters (σ, ε) of Lennard-Jones for Fe, Ni, Pb for Potential and Cr based on Melting Point Values Using the Molecular Dynamics Method of the Lammps Program*. In *J. Phys.: Conf. Ser.*, volume 1491, page 012022. IOP Publishing, (2020).

[219] J. Delhommelle and P. Millié, *Inadequacy of the Lorentz-Berthelot combining rules for accurate predictions of equilibrium properties by molecular simulation*, Molecular Physics **99**, 619–625 (2001).

[220] C. Herrera, G. Garcia, M. Atilhan, and S. Aparicio, *Nanowetting of graphene by ionic liquid droplets*, J. Phys. Chem. C **119**, 24529–24537 (2015).

[221] R. Burt, G. Birkett, M. Salanne, and X. Zhao, *Molecular dynamics simulations of the influence of drop size and surface potential on the contact angle of ionic-liquid droplets*, J. Phys. Chem. C **120**, 15244–15250 (2016).

[222] Y. Guan, Q. Shao, W. Chen, S. Liu, X. Zhang, and Y. Deng, *Dynamic three-dimensional nanowetting behavior of imidazolium-based ionic liquids probed by molecular dynamics simulation*, J. Phys. Chem. C **121**, 23716–23726 (2017).

[223] L. Martínez, R. Andrade, E. G. Birgin, and J. M. Martínez, *PACKMOL: a package for building initial configurations for molecular dynamics simulations*, J. Comput. Chem. **30**, 2157–2164 (2009).

[224] E. E. Santiso, C. Herdes, and E. A. Müller, *On the calculation of solid-fluid contact angles from molecular dynamics*, Entropy **15**, 3734–3745 (2013).

[225] M. Khalkhali, N. Kazemi, H. Zhang, and Q. Liu, *Wetting at the nanoscale: A molecular dynamics study*, J. Chem. Phys. **146**, 114704 (2017).

[226] Y. Yuan and T. R. Lee. *Contact angle and wetting properties*. In *Surf. Sci. techniques*, pages 3–34. Springer, (2013).

[227] F. Liu and W. Shen, *Forced wetting and dewetting of liquids on solid surfaces and their roles in offset printing*, Colloids Surf., A **316**, 62–69 (2008).

[228] C. Aliaga and S. Baldelli, *A sum frequency generation study of the room-temperature ionic liquid- titanium dioxide interface*, J. Phys. Chem. C **112**, 3064–3072 (2008).

[229] S. Xu, S. Xing, S.-S. Pei, and S. Baldelli, *Sum frequency generation spectroscopy study of an ionic liquid at a graphene-BaF2 (111) interface*, J. Phys. Chem. B **118**, 5203–5210 (2014).

[230] Q. Guo, I. Cocks, and E. Williams, *The adsorption of benzoic acid on a TiO2 (110) surface studied using STM, ESDIAD and LEED*, Surf. Sci. **393**, 1–11 (1997).

[231] C. Perry, S. Haq, B. Frederick, and N. Richardson, *Face specificity and the role of metal adatoms in molecular reorientation at surfaces*, Surf. Sci. **409**, 512–520 (1998).

[232] B. Frederick, F. Leibsle, S. Haq, and N. Richardson, *Evolution of lateral order and molecular reorientation in the benzoate/Cu (110) system*, Surf. Rev. Lett. **3**, 1523–1546 (1996).

[233] M. A. Morosanova and E. I. Morosanova, *Silica-titania xerogel for solid phase spectrophotometric determination of salicylate and its derivatives in biological liquids and pharmaceuticals*, Chem. Cent. J. **9**, 1–8 (2015).

[234] Y. Imai and J.-i. Kamada, *Vibrational spectra of saccharin nitranion and its orientation on the surface of silver metal particles*, Spectrochim. Acta, Part A **61**, 711–715 (2005).

[235] Q. J. Wang and Y.-W. Chung, *Encyclopedia of tribology*, Springer (2013).

[236] A. Libardi, S. Schmid, M. Sen, and W. Schneider, *Evaluation of ionic fluids as lubricants in manufacturing*, Journal of Manufacturing Processes **15**, 414–418 (2013).

[237] R. González, J. L. Viesca, A. H. Battez, M. Hadfield, A. Fernández-González, and M. Bartolomé, *Two phosphonium cation-based ionic liquids as lubricant additive to a polyalphaolefin base oil*, J. Mol. Liq. **293**, 111536 (2019).

[238] H. Arora and P. Cann, *Lubricant film formation properties of alkyl imidazolium tetrafluoroborate and hexafluorophosphate ionic liquids*, Tribology International **43**, 1908–1916 (2010).

[239] A. H. Battez, N. Rivera, D. Blanco, P. Oulego, J. Viesca, and R. González, *Physicochemical, traction and tribofilm formation properties of three octanoate-, laurate- and palmitate-anion based ionic liquids*, Journal of molecular liquids **284**, 639–646 (2019).

[240] J. Viesca, J. Faes, N. Rivera, E. Rodríguez, M. Cadenas, and R. González, *Thermal stability, traction and tribofilm formation of three fatty acid-derived ionic liquids*, Tribology International **154**, 106712 (2021).

[241] T. Liu, P. Panwar, A. Khajeh, M. H. Rahman, P. L. Menezes, and A. Martini, *Review of Molecular Dynamics Simulations of Phosphonium Ionic Liquid Lubricants*, Tribol. Lett. **70**, 1–24 (2022).

[242] T. Liu, M. H. Rahman, P. L. Menezes, and A. Martini, *Effect of Ion Pair on Contact Angle for Phosphonium Ionic Liquids*, J. Phys. Chem. B **126**, 4354–4363 (2022).

[243] P. Panwar, E. Schweissinger, S. Maier, S. Hilf, S. Sirak, and A. Martini, *Effect of polymer structure and chemistry on viscosity index, thickening efficiency, and traction coefficient of lubricants*, Journal of Molecular Liquids **359**, 119215 (2022).

[244] D. Tsai, *The virial theorem and stress calculation in molecular dynamics*, The Journal of Chemical Physics **70**, 1375–1382 (1979).

[245] T. A. Harris and M. N. Kotzalas. *Rolling bearing analysis, CRC*, (2007).

[246] S. Maćkowiak, D. Heyes, D. Dini, and A. Brańka, *Non-equilibrium phase behavior and friction of confined molecular films under shear: A non-equilibrium molecular dynamics study*, The Journal of Chemical Physics **145**, 164704 (2016).

[247] P. Panwar, Q. Yang, and A. Martini. *PyL3dMD: Python LAMMPS 3D Molecular Descriptors*. `https://github.com/panwarp/PyL3dMD`. Journal of Cheminformatics (Under review).

[248] C. Gabler, C. Tomastik, J. Brenner, L. Pisarova, N. Doerr, and G. Allmaier, *Corrosion properties of ammonium based ionic liquids evaluated by SEM-EDX, XPS and ICP-OES*, Green Chem. **13**, 2869–2877 (2011).

[249] Y. Ma, F. Han, Z. Li, and C. Xia, *Corrosion behavior of metallic materials in acidic-functionalized ionic liquids*, ACS Sustainable Chem. Eng. **4**, 633–639 (2016).

[250] C. Verma, E. E. Ebenso, and M. Quraishi, *Ionic liquids as green and sustainable corrosion inhibitors for metals and alloys: an overview*, J. Mol. Liq. **233**, 403–414 (2017).

[251] C. Verma, S. H. Alrefaee, M. Quraishi, E. E. Ebenso, and C. M. Hussain, *Recent developments in sustainable corrosion inhibition using ionic liquids: A review*, J. Mol. Liq. **321**, 114484 (2021).

[252] M. Uerdingen, C. Treber, M. Balser, G. Schmitt, and C. Werner, *Corrosion behaviour of ionic liquids*, Green Chem. **7**, 321–325 (2005).

[253] B. Dilasari, Y. Jung, J. Sohn, S. Kim, and K. Kwon, *Review on corrosion behavior of metallic materials in room temperature ionic liquids*, Int. J. Electrochem. Sci. **11**, 1482–1495 (2016).

[254] I. Perissi, U. Bardi, S. Caporali, and A. Lavacchi, *High temperature corrosion properties of ionic liquids*, Corros. Sci. **48**, 2349–2362 (2006).

[255] K. Wu, X. Zhou, X. Wu, B. Lv, G. Jing, and Z. Zhou, *Understanding the corrosion behavior of carbon steel in amino-functionalized ionic liquids for CO_2 capture assisted by weight loss and electrochemical techniques*, Int. J. Greenhouse Gas Control **83**, 216–227 (2019).

[256] L. Pisarova, C. Gabler, N. Dörr, E. Pittenauer, and G. Allmaier, *Thermo-oxidative stability and corrosion properties of ammonium based ionic liquids*, Tribol. Int. **46**, 73–83 (2012).

[257] Y.-C. Wang, T.-C. Lee, J.-Y. Lin, J.-K. Chang, and C.-M. Tseng, *Corrosion properties of metals in dicyanamide-based ionic liquids*, Corros. Sci. **78**, 81–88 (2014).

[258] B. Dilasari, Y. Jung, and K. Kwon, *Comparative study of corrosion behavior of metals in protic and aprotic ionic liquids*, Electrochem. Commun. **73**, 20–23 (2016).

[259] L. T. Popoola, *Progress on pharmaceutical drugs, plant extracts and ionic liquids as corrosion inhibitors*, Heliyon **5**, e01143 (2019).

[260] Q. Zhang and Y. Hua, *Corrosion inhibition of mild steel by alkylimidazolium ionic liquids in hydrochloric acid*, Electrochim. Acta **54**, 1881–1887 (2009).

[261] Y. Qiang, S. Zhang, L. Guo, X. Zheng, B. Xiang, and S. Chen, *Experimental and theoretical studies of four allyl imidazolium-based ionic liquids as green inhibitors for copper corrosion in sulfuric acid*, Corros. Sci. **119**, 68–78 (2017).

[262] Y. L. Kobzar and K. Fatyeyeva, *Ionic liquids as green and sustainable steel corrosion inhibitors: Recent developments*, Chem. Eng. J. **425**, 131480 (2021).

[263] T. Espinosa, J. Sanes, A.-E. Jiménez, and M.-D. Bermúdez, *Surface interactions, corrosion processes and lubricating performance of protic and aprotic ionic liquids with OFHC copper*, Applied Surf. Sci. **273**, 578–597 (2013).

[264] M. del Arco, S. Gutiérrez, C. Martín, V. Rives, and J. Rocha, *Synthesis and characterization of layered double hydroxides (LDH) intercalated with non-steroidal anti-inflammatory drugs (NSAID)*, J. Solid State Chem. **177**, 3954–3962 (2004).

[265] M. Ata, Y. Liu, and I. Zhitomirsky, *A review of new methods of surface chemical modification, dispersion and electrophoretic deposition of metal oxide particles*, RSC Adv. **4**, 22716–22732 (2014).

[266] S. Roy and J. Kästner, *Synergistic substrate and oxygen activation in salicylate dioxygenase revealed by QM/MM simulations*, Angew. Chem., Int. Ed. **55**, 1168–1172 (2016).

[267] J. A. Van der Horn, B. Souvignier, and M. Lutz, *Crystallization, Structure Determination and Reticular Twinning in Iron (III) Salicylate: Fe[(HSal)(Sal)(H_2O)$_2$]*, Crystals **7**, 377 (2017).

[268] R. Bucci, V. Carunchio, and A. Girelli, *Formation of iron (II) complexes with some aromatic anions in DMSO*, Inorg. Chim. Acta **141**, 99–102 (1988).

[269] A. C. Mendonça, P. Malfreyt, and A. A. Padua, *Interactions and ordering of ionic liquids at a metal surface*, J. Chem. Theory Comput. **8**, 3348–3355 (2012).

[270] M. Sobota, I. Nikiforidis, W. Hieringer, N. Paape, M. Happel, H.-P. Steinruck, A. Gorling, P. Wasserscheid, M. Laurin, and J. Libuda, *Toward ionic-liquid-based model catalysis: growth, orientation, conformation, and interaction mechanism of the [Tf_2N]- anion in [BMIM][Tf_2N] thin films on a well-ordered alumina surface*, Langmuir **26**, 7199–7207 (2010).

[271] H. Khanmohammadi, W. Wijanarko, and N. Espallargas, *Ionic liquids as additives in water-based lubricants: from surface adsorption to tribofilm formation*, Tribology Letters **68**, 1–15 (2020).

[272] M. Ji, S. Liu, and H. Xiao, *Effect of Ionic Liquids as Additives in Water-Based Drilling Mud for Steel–Steel Friction Pair*, Tribology Transactions **63**, 453–467 (2020).

[273] A. Khan, O. P. Sharma, and O. P. Khatri, *Ionic liquids-based aqueous lubricants: Emulsion stability to enhancement of surface wettability and tribological properties*, Industrial & Engineering Chemistry Research **60**, 333–342 (2020).